PAUL SCHERRER INSTITUT
PSI

u^b

b
UNIVERSITÄT
BERN

LABOR FÜR RADIO- UND UMWELTCHEMIE
DER UNIVERSITÄT BERN UND
DES PAUL SCHERRER INSTITUTS

Annual Report 2014

Laboratory of Radiochemistry and Environmental Chemistry

PAUL SCHERRER INSTITUT

PSI

u^b

^{b}
UNIVERSITÄT
BERN

LABOR FÜR RADIO- UND UMWELTCHEMIE
DER UNIVERSITÄT BERN UND
DES PAUL SCHERRER INSTITUTS

Annual Report 2014

Laboratory of Radiochemistry and Environmental Chemistry

Editors
A. Türler, M. Schwikowski, A. Blattmann

See also our web-page
http://www.psi.ch/lch/

TABLE OF CONTENTS

Analytical Chemistry

Radwaste Analytics

Radionuclide Development

Environmental Radionuclides Universität Bern

EDITORIAL

In August it has been 5 years since I started as the new head of the Laboratory of Radiochemistry and Environmental Chemistry (LCH) and it is now time to reflect and draw some conclusions. In all, I am extremely satisfied with what LCH has accomplished and how it has developed. The solid foundation left to me by my predecessor Heinz Gäggeler has allowed me to add new topics, such as radionuclide development for medical applications, rather than having to cut programs and to reduce activities. I thank all my group leaders for their continued excellent work and for all the support I received from them. This way, all groups were able to develop and to bring their projects to fruition. Most visible are our three large projects, namely the NAPP-XPS instrument at the SLS at PSI, the MICADAS accelerator mass spectrometer and the radiopharmaceutical laboratory at UNIBE, which now all start to produce exciting scientific results. The fact that all three projects turned out to be extremely successful was by no means self-evident and many technical, financial and other hurdles had to be mastered. As a result, our reputation as a reliable and responsible partner has gained us the trust of the directorate of PSI and University of Bern and our funding organisations. Less satisfying is the integration of LCH into the department biology and chemistry (BIO) at PSI. While we entertain excellent and very fruitful collaborations with the Center for Radiopharmaceutical Sciences our scientific overlap with biology is scarce.

In 2014, LCH surpassed its record set in 2013, with more than 80 original research papers being published, more than double the previous record! Of these papers, two warrant mentioning: Margit Schwikowski, Sönke Szidat and Yanlin Zhang were co-authors of a paper investigating extreme haze events in China published in NATURE, with the leading house being the Laboratory of Atmospheric Chemistry of PSI. The other featured the synthesis of seaborgium carbonyls, published in SCIENCE by an international collaboration with Robert Eichler, Ilya Usoltsev and myself as co-authors.

Our unit was also very successful in acquiring third party funding. Margit Schwikowski is coordinating a new "Sinergia" project funded by the Swiss National Science Foundation with participants from the Oeschger Center for Climate Research of the University of Bern and from the ETHZ. The overall objective is to significantly advance the understanding of complex systemic linkages between climate, land use, fire and vegetation. Another extremely important milestone was the successful application for an interdisciplinary project together with the Laboratory for High Energy Physics of the University of Bern and the Center for Radiopharmaceutical Sciences, PSI, as co-applicants. In this project we will explore possibilities to produce the positron-emitting radionuclide ^{43}Sc at a medical cyclotron and investigate its use and application in nuclear medicine.

A further highlight of 2014 was the adjunct professorship awarded to Markus Ammann by ETHZ. This well-deserved honor, again, enhances the standing and visibility of our unit.

The education of apprentices has gained more visibility with the promotion of Roman Bentz to group leader. LCH now consists of eight groups.

Our PhD students were once again very successful, with Nadine Chiera being the third student in a row to win a prize at the University of Bern graduate student symposium. As a result, group leader Robert Eichler celebrates a hat-trick.

The radiopharmaceutical laboratory at the Insel University Hospital in Bern started to produce a first tracer for positron emission tomography. The compound, ^{68}Ga-DOTA-TATE, allows excellent visualization of neuroendocrine tumors and is far superior to previously-used ^{111}In-octreotide. Nearly 30 patients were able to profit from this new commodity in Bern. I am very happy that former PhD student Maruta Bunka decided to join the production team in Bern after graduating in February 2014. Michael Sigl, a former PhD student of Margit Schwikowski, is also working again at LCH as an advanced PostDoc following his return from the US.

This year's social event had an educational aspect, resulting in a tour of the nuclear power plant in Gösgen, a first for many of us. After a light lunch, sponsored by KKG, we climbed the "Engelberg" from where we enjoyed a great view and other "heavenly" food and drink. The event was organized by Dorothea Schumann and her staff.

We concluded an extremely successful 2014 with a dinner in the old "Tramdepot", a microbrewery at the Bärengraben in Bern, but only after a guided tour on foot through the city of Bern, which, by the way, is a UNESCO world heritage site! This way, everybody was sufficiently hungry to indulge in the spare ribs on offer and wash them down with the local brew. The record number of participants tells me that not only is LCH on a good way scientifically, but also as a group of people that want to work and accomplish things together as a team. I am convinced that LCH is an outstanding unit and well prepared to face the challenges of the future.

Our annual report gives an account of "work in progress" and, as such, provides more of an outlook of things to come, rather than a review of already published work.

Andreas Türler

STABILITY OF THE GROUP VI CARBONYL COMPLEXES: MONTE-CARLO MODELLING OF THE DECOMPOSITION PROCESS

I. Usoltsev, R. Eichler, A. Türler (Univ. Bern & PSI)

In 2014 chemistry, for the first time, acquired a Sg compound in its zero oxidation state – $Sg(CO)_6$ [1]. The enthalpy of adsorption for $Sg(CO)_6$ on a quartz surface was found to be in a good agreement with the corresponding theoretical prediction, supporting the presumed composition of the formed compound. Already in 1999 $Sg(CO)_6$ was predicted to be more stable than the complex of its lighter homologue $W(CO)_6$. The first bond dissociation energy (FBDE) was calculated as 197 ± 8 kJ/mol, which is about 4 kJ/mol higher, if compared to $W(CO)_6$ [2]. Earlier, we suggested an experimental approach for testing the stability of the group VI carbonyl complexes [3]. In this report we suggest a method for the quantitative assessment of the $Sg(CO)_6$ FBDE, which will be derived from the future experimental data on its stability.

Our idealized decomposition model includes only the heterogeneous decomposition, simulated as a two-step process: reversible adsorption is eventually followed by irreversible decomposition (Eqn.1). This is justified by the observation of a strong dependence of the decomposition temperature on the applied stationary surface material [3] and to a lesser extent on the gas flow.

$$Me(CO)_6 \leftrightarrow Me(CO)_{6(ads)} \rightarrow Me + 6\,CO \qquad \text{Eqn. 1}$$

In order to simulate the decomposition behavior in a *laminar flow reactor* [3], the gas-phase chromatography model was complemented by an idealized kinetic model, under the following assumptions:

1. The decomposition reaction happens only on the phase boundary and is irreversible.

2. The activation enthalpy ΔH^+ of the decomposition reaction equals the corresponding FBDE.

The decomposition reaction time t_r was gained through the reaction rate k, expressed by the Eyring equation and implemented in the model as follows:

$$k = k_B \cdot T/h \cdot exp(\Delta S^+/R) \cdot exp(-\Delta H^+/R T) \qquad \text{Eqn. 2}$$

$$t_r = -1/k \cdot ln(1\text{-}random) \qquad \text{Eqn. 3}$$

Where k is a decomposition rate constant [1/s]; k_B is the Boltzmann constant [J/K]; h is the Planck constant [J·s]; ΔS^+ is the activation entropy [J/K/mol]; ΔH^+ is the activation enthalpy of the decomposition [J/mol].

The model describes an adsorption chromatographic transport of volatile molecules along the tubular stationary surface, as given in [4]. Upon each adsorption of a carbonyl complex a decision is being made: if the adsorption time $\leq t_r$, then the hexacarbonyl complex desorbs form the surface without decomposition; if the adsorption $> t_r$, then an irreversible decomposition reaction is assumed. The experimental result on decomposition of Mo and W carbonyls were reproduced by adjusting a single parameter: ΔS^+ (Fig. 1). Its value was determined as 105 ± 3 kJ/mol/K through a least

squares fit procedure with a 95% confidence interval for both complexes independently.
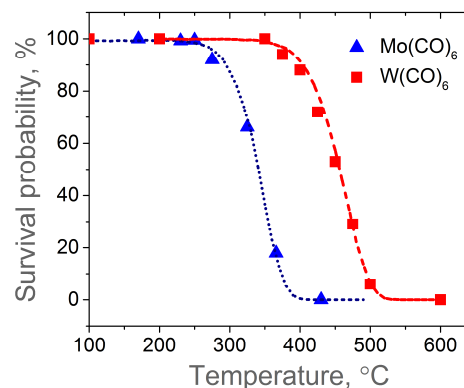
Fig. 1: Experimental decomposition curves of Mo and W carbonyl complexes (symbols) and the corresponding simulations (dotted and dashed lines).

Under the assumption of a similar reaction mechanism for $Sg(CO)_6$, the decomposition behaviour of the complex can be simulated (Fig. 2). About 8 kJ/mol uncertainty difference, given by the prediction [2], corresponds to ~50°C shift (see Fig. 2). The simulation of the $Sg(CO)_6$ decomposition curve would allow for a quantification of the corresponding FBDE and thereby for testing the relativistic theoretical prediction. Therefore, the complete method for experimental verification of $Sg(CO)_6$ stability was elaborated in [5].
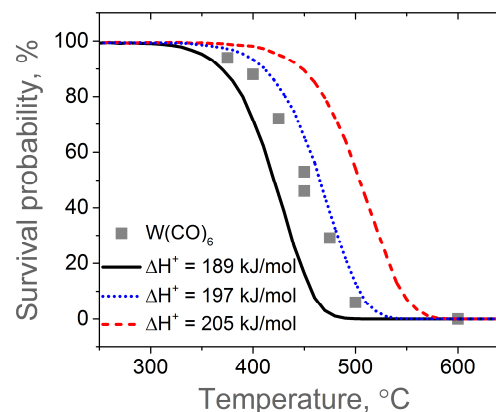
Fig. 2: Simulated decomposition curves of $Sg(CO)_6$ at different FBDE. The experimental decomposition curve for $W(CO)_6$ is given for orientation.

---

[1] J. Even et al., Science, **345**, 6203 (2014).
[2] C. S. Nash, J.Am.Chem.Soc., **121**, 10830 (1999).
[3] I. Usoltsev et al., Ann. Rep. Lab.of Radio- & Environ. Chem., Univ. Bern & PSI, (2013), p. 3.
[4] I. Zvara, The Inorganic Radiochemistry of Heavy Elements, Springer (2008).
[5] I. Usoltsev, PhD Thesis, Univ. of Bern (2014).

CHEMICAL STABILITY OF GROUP VI CARBONYL COMPLEXES: PREPARATION OF THE Sg HEXACARBONYL STABILITY TEST

I. Usoltsev, R. Eichler, A. Türler (Univ. Bern & PSI)

The recently reported chemical identification of $Sg(CO)_6$ [1] confirmed relativistic predictions regarding its thermochemical property – ΔH_{ads} on a quartz surface [2]. Verification of earlier predictions with respect to the thermodynamic stability of the complex [3] is envisaged in the nearest future and can be implemented as suggested in [4]. However, there are a number of experimental difficulties we would like to discuss here, which might jeopardize a milestone experiment. Test experiments with $Mo(CO)_6$ were carried out at the ^{252}Cf spontaneous fission source, at University of Bern. We found that O_2 has a strong impact on the production yield of $^{104}Mo(CO)_6$ (Fig. 1). Already a few vol-% of O_2 in the carrier gas bring the yield down to less than 20%. The effect stems from the high stability of MoO_2 and MoO_3 oxides, with formation enthalpies of -589 kJ/mol and -745 kJ/mol, respectively. The influence of oxygen content on the production yields of $W(CO)_6$ was not studied systematically. Nevertheless, it was qualitatively observed, that the formation of $W(CO)_6$ is much more sensitive to O_2, than the formation of $Mo(CO)_6$, by comparing transport yields of the carbonyls with and without Oxysorb® cartridges installed in the gas-loop, described in [1]. This can be attributed to an even higher stability of WO_2 and WO_3, which have formation enthalpies of -590 kJ/mol and -843 kJ/mol. SgO_3 was predicted to have a heat of formation lower than -850 kJ/mol, which makes this system the most sensitive to O_2 among all group VI elements. Therefore, the O_2 content in the carrier gas must be kept very low and must be constantly monitored, as it can introduce ambiguity to the stability experiments.
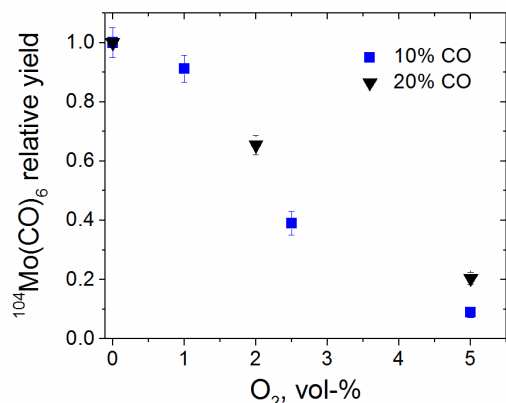
Fig. 1: Influence of the O_2 content in the carrier gas on the $^{104}Mo(CO)_6$ production yield.

Due to the relatively high sublimation point (-78°C) carbon dioxide tends to freeze-block cryo-thermochromatography detectors as used in [1]. CO_2 comes as an admixture to carbon monoxide and can be also permanently produced by oxidation of the latter in the gas-jet system by trace contaminations of oxygen. Thus special cleaning units such as molecular sieves, liquid nitrogen traps or chemical absorbents have to be employed in the system for effective elimination of the produced CO_2. Implementation of a decomposition column facilitates the reaction between CO and O_2 and therefore promotes the formation of CO_2 in the system. The operation of a silver column at 500°C brings about a twofold increase in the CO_2 content, as determined with the MKS Cirrus 2® atmospheric pressure mass spectrometer (see Fig. 2). This particular source of CO_2 cannot be easily eliminated, since cleaning units between the decomposition column and the detection system are excluded.

Therefore, we suggest implementing a Pt/CeO_2 catalyst [5] for efficient burning of CO into CO_2, as a pre-cleaning step for removing O_2 from the carrier gas. The formed CO_2 must be removed from the gas efficiently before reaching the RTC e.g. with a CaO cartridge or similar reactive agents.
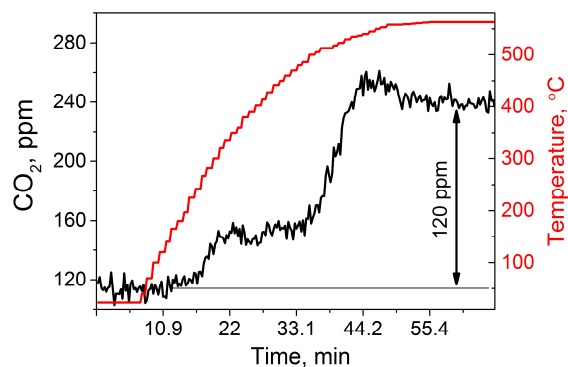
Fig. 2: Influence of the silver decomposition column temperature on the CO_2 content in the carrier gas at 1 l/min gas flow rate and 100 vol-% CO content.

Furthermore, we estimated the average adsorption time for $^{265}Sg(CO)_6$ in the 10 m Teflon® capillary under the experimental conditions applied in [1]. The retention time is strongly dependent on the gas flow rate, on the pressure, on the temperature, and on the adsorption enthalpy of the investigated species. In the worst case scenario the adsorption time can exceed one minute. The transport efficiency could be largely improved in upcoming experiments by heating the capillary up to about 100°C. The decomposition of the complex at this temperature is expected to be negligible [4,6].

[1] J. Even et al., Science, **345**, 6203 (2014).

[2] V. Pershina et al., J.Chem.Phys. **138**, 174301 (2013).

[3] C. S. Nash, J.Am.Chem.Soc., **121**, 10830 (1999).

[4] I. Usoltsev, PhD Thesis, Univ. Bern (2014).

[5] B. Parthasarathi et. Al, J.Phys. Chem. B **107**, 6122 (2003).

[6] I. Usoltsev et al., Ann. Rep. Lab. of Radio- & Environ. Chem., Univ. Bern & PSI (2014).

TOWARDS SELENIDES OF THE SUPERHEAVY ELEMENTS Cn AND Fl

N. M. Chiera, R. Eichler, A. Türler (Univ. Bern & PSI)

The aim of this work is to study the chemical interaction of the superheavy elements copernicium (Z = 112) and flerovium (Z = 114) with selenium deposited on a surface. The mutual correlation of thermochemical state functions revealed stability trends among chalcogenides in group 12 and 14 of the periodic table. They predict the formation of FlSe to be stronger compared to its lighter homologues, while the interaction between Cn and selenium is expected to be weaker compared to its homologues [1]. Among all selenium allotropes, recent studies reported red amorphous nano-selenium as an efficient mercury sorbent, due to the high affinity of this modification of Se towards Hg and the high surface-to-mass ratios of the nanoparticles [2]. In preparation of experimental investigations with superheavy elements, isothermal reaction chromatography experiments with Hg and red amorphous selenium (a-Se) surfaces were performed. Homogeneous stationary surfaces of a-Se with 95% surface coverage were obtained through deposition of super-cooled vapour of elemental selenium on quartz substrates. Monte-Carlo simulations of the reaction chromatography are in good agreement with the measured experimental data, assuming an upper interaction limit -ΔH_{ads}^{Hg}(a-Se) > 85 kJ/mol [1]. However, red amorphous Se, being a metastable phase, undergoes a transformation to the most stable trigonal crystal structure (t-Se). The control of this phase transition process is crucial, since the trigonal structure is less reactive than the amorphous one (Fig. 1).
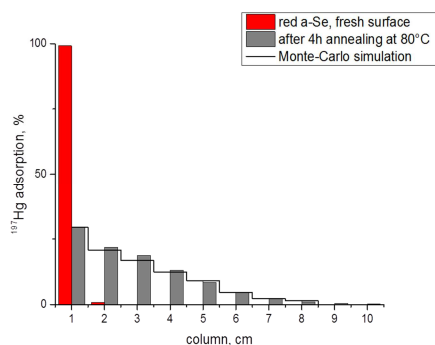
Fig. 1: The deposition of ^{197}Hg on a 10 cm selenium column annealed for 4 hours at 80°C (grey bars), is shown. The Monte-Carlo simulation (solid black line) with a -ΔH_{ads}^{Hg}(t-Se) > 67.5 kJ/mol for a 50% t-Se and a 13% a-Se surface coverage is indicated. The ^{197}Hg deposition on a 10 cm a-Se fresh deposited surface is shown for comparison. Experimental ^{197}Hg deposition conditions: T= 25°C, 25 ml/min He gas flow.

The physico-chemical properties, e.g. the crystallization rate of this amorphous material vary with the preparation procedure and the storage method [3].

The vapour transport deposition (VTD) technique was optimized to obtain a relatively stable amorphous selenium surface. This method, unlike chemical bath deposition or electroplating, can be easily kept free from impurities like water, organic substances and oxygen. The VTD is based on a fast quenching of selenium vapour held at a maximum temperature of 653 K. At this temperature the major component of selenium vapour is Se$_6$, a ring-like molecule which high symmetry and electronic stability leads to an amorphous selenium structure. This structure slowly undergoes crystallization by ageing, if it's kept in a dark, inert environment, at a storage temperature below the glass transition point (T$_g$ ~ 25 °C) [4-6]. The elaborated VTD method allows for the coverage of silicon PIN diode detectors with a homogeneous a-Se layer with thicknesses of a few hundred nanometers to permit alpha-particle spectroscopy (Fig. 2).
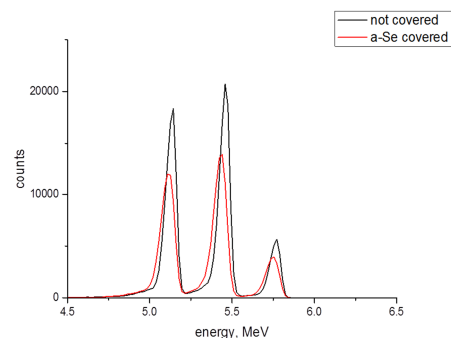
Fig. 2: Alpha spectrum for a standard α-emitting mixed nuclides (^{239}Pu; ^{241}Am, ^{244}Cm) source with an uncovered PIN diode (black line) and the same diode covered with a 0.2µm thickness a-Se layer, composed of 0.3µm diameter Se particles (red line). The thickness of the layer and the particles dimension were deduced performing alpha spectroscopy simulation with the AASIFIT software [7].

[1] N. Chiera, Ann Rep. Lab. of Radio- & Environ. Chem., Univ. Bern & PSI (2013), p. 7.
[2] N. Ralston, Nature Nanotech. **9**, 527 (2008).
[3] R. Clement et al., J. Non-Cryst. Solids, **15**, 3 (1974).
[4] J. Berkowitz et. al, J. Chem. Phys., **45**, 4289, (1966).
[5] Z. Q. Li et al., Phys. Rev. B., **52**, 3 (1995).
[6] J.P. Audiere et al., J. Non-Cryst. Solids, **34**, 1 (1979).
[7] T. Siiskonen, R. Pöllänen, T. Karhunen AASI 2.0 http://www.stuk.fi/yhteistyo/programs/aasi/en_G B/aasi/

4-FOLD DIAMOND DETECTOR FOR ISOTHERMAL VACUUM CHROMATOGRAPHY EXPERIMENTS

P. Steinegger, R. Eichler, A. Türler (Univ. Bern & PSI), R. Dressler, D. Piguet (PSI)

In order to chemically characterize less volatile ($-\Delta H_{ads} > 47$ kJ·mol^{-1}) superheavy elements (SHE) in the gas phase, higher stationary surface temperatures are essential [1]. Hence, a special α-spectroscopy detector material is needed, being able to withstand these high temperatures – either as high temperature stationary surface itself or as an external detector close to a high temperature chromatography column exit. In case of the commonly used Si-based α-detectors, a critical threshold is encountered at roughly 40ºC, above which any spectroscopic measurement is prevented due to considerable thermal excitation (Si band gap of 1.12 eV). Diamond, on the other hand, outperforms its heavier homolog by far. Due to its relatively large band gap of 5.5 eV, α-spectroscopic measurements in the range of the Debye temperature of diamond (2340 K) are theoretically feasible [2], thereby making it a superior candidate for future SHE chemistry studies of less volatile species. Herein we present a 4-fold diamond detector, successfully used in a first E113 model experiment, using an isotope of the lighter homolog thallium, ^{184}Tl [3].

Four single crystal, electronic grade chemical vapour deposition (CVD) diamond plates (4.5 x 4.5 x 0.5 mm) [4] were cleaned and surficial oxidized according to a procedure adopted from [2].
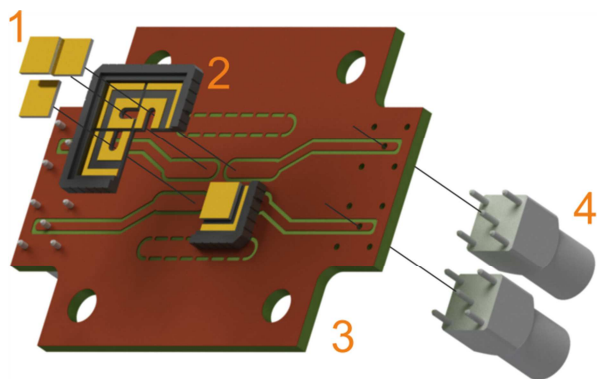
Fig. 1: Exploded view of the 4-fold diamond detector assembly with **1** the single diamond detectors, **2** the modified CLCC, **3** the custom-made PCB and **4** the LEMO® 00 connectors.

The samples were metallized on both sides differently – once to the very edges (front side, Fig. 1) and once only partially, leaving a bare frame around the back electrode with a width of 0.5 mm. Prior to each of the two thermal metallization steps, a 15 minutes UV/ozone treatment finalized the diamond surface oxidation and ensured the removal of remaining organic impurities. Both electrodes consisted of a first 10 – 20 nm Cr layer, followed by a 100 – 110 nm Au layer. Four modified ceramic leadless chip carriers (CLCC)

were assembled on a custom-made printed circuit board (PCB) together with the four, prepared diamond detectors (Fig. 1). All parts were finally fixed with the electrically conductive adhesive EPO-TEK® H20S, whereas the front electrode was grounded and interconnected using Al wire-bonding. This design [5], with the high-voltage (HV = 0.6 V/μm) individually applied from the read-out side (back), enables measurements at low HF noise levels.

The read-out electronics consists of four CIVIDEC Cx spectroscopic shaping amplifiers [6] with a Gaussian pulse shaping time of 250 ns. The satisfying energy resolution $\Delta E/E \approx 1.2\%$ at 5.257 MeV (^{239}Pu) together with the inexistent high energetic background (Fig. 2) are utterly important characteristics for a detector being used for the identification of SHEs.
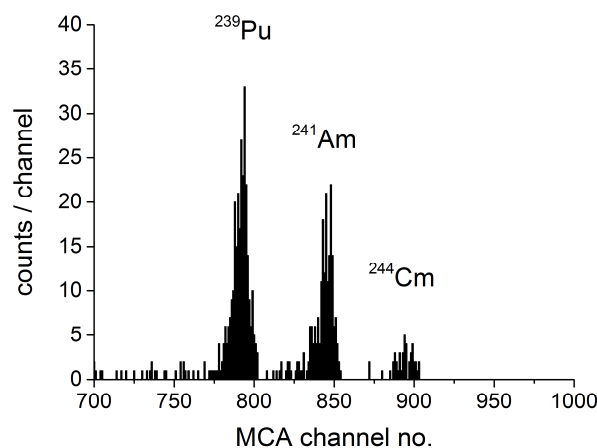
Fig. 2: Sample spectrum of channel EG2 (LT = 500 s, HV = 0.6 V/μm).

ACKNOWLEDGEMENT

---

[1]   M. Schädel, Angew. Chem. **118**, 3 (2006).
[2]   M. Pomorski, PhD thesis, Goethe Universität, Frankfurt am Main (2008).
[3]   P. Steinegger et al., see this report, pp. 7 & 8.
[4]   *Element Six Ltd.*, Ascot, United Kingdom.
[5]   C. Weiss et al., Nucl. Instr. Meth. A **732** (2013).
[6]   *CIVIDEC Instrumentation GmbH*, Wien, Austria.

THE ISOL – IVAC EXPERIMENT:
EXPERIMENTAL SETUP

P. Steinegger, R. Eichler, A. Türler (Uni. Bern & PSI), M. Asai, Y. Kaneya, A. Mitsukai, Y. Nagame, T. K. Sato,
M. Schädel, S. Takeda, A. Toyoshima, K. Tsukada, A. Vascon (ASRC, JAEA, Japan), R. Dressler, D. Piguet (PSI)

Gas-phase chromatography experiments have proven to be a fast and reliable technique for chemically characterizing volatile superheavy elements (SHE) in their elemental state using isotopes with half-lives above one second [1]. However, for investigating less volatile ($-\Delta H_{ads} > 47$ kJ·mol^{-1}) and more short-lived (i.e. $t_{1/2} < 1$ s) species, a different experimental approach has to be chosen. The stronger interaction with the stationary surface demands for higher stationary surface temperatures and thus, for the development of novel, fairly temperature resistant detectors based on CVD diamond [2]. A considerable decrease in transport time on the other hand, can be achieved by switching from a standard gas-phase experiment (laminar flow regime) to a vacuum experiment (molecular flow range). The principle of the vacuum chromatography technique, as a method for investigating SHEs, has been suggested already in [3]. Beside accessing isotopes with shorter half-lives the transition into vacuum brings along further advantages, such as no aerosol-bound transport of non-volatile by-products (i.e. lower background) and clean chromatographic surfaces. However, the necessity of stopping the nuclear reaction products in an evacuated environment remains a major challenge. The implantation and subsequent thermal release (hereinafter referred to as *hot catcher*) of those products appears to be the most promising – and presumably the only realistic – solution [4]. In the following, we report on an isothermal vacuum chromatography (IVAC) setup, combining for the first time a thin foil hot catcher unit with an isothermal chromatography experiment including the novel diamond detectors [2]. The experiment was tested using the model system ^{184}Tl ($t_{1/2} = 10.3$ s, Iα = 2.1%) on quartz [2], with Tl as the lighter homolog of E113 in group 13 of the periodic table. ^{184}Tl was produced at the JAEA tandem accelerator in the reaction ^{152}Gd(^{35}Cl, 3n)^{184}Tl, using a ^{35}Cl^{10+} beam of $E_{lab} \approx 186$ MeV with an average intensity of $\approx$150 pnA. The nuclear reaction products were first stopped in the adjacent recoil chamber and then transported by means of a He/CdI$_2$ gas-jet ($Q_{He} = 1.4$ l/min) to the JAEA-ISOL setup [5]. After ionization, the reaction products were accelerated, mass-separated and finally delivered to the IVAC system (Fig. 1, $p_{IVAC} \approx 10^{-5}$ mbar) at moderate translational energies of 30 keV. Thus, the present study rather serves as a model for an experiment, using a gas catcher setup yielding products featuring similar kinetic energies [6]. However, these low energies required an entrance hole of $\varnothing_{entr} = 3$ mm diameter that had to be included in the hot catcher containment. The containment itself consisted of a cylindrical Ta heat shield, with the possibility of an inner coverage by a quartz insert. Together with ceramic end caps it confines the space around the hot catcher, thereby providing a rapid guidance of the released products into the directly connected isothermal chromatography column ($\varnothing_{col\_in} > \varnothing_{entr}$) or through the entrance hole (significant losses). In accordance with [4], Zr and Hf foils (both 25 µm thick) served as hot catcher, being resistively heated up to approximately 1600ºC.
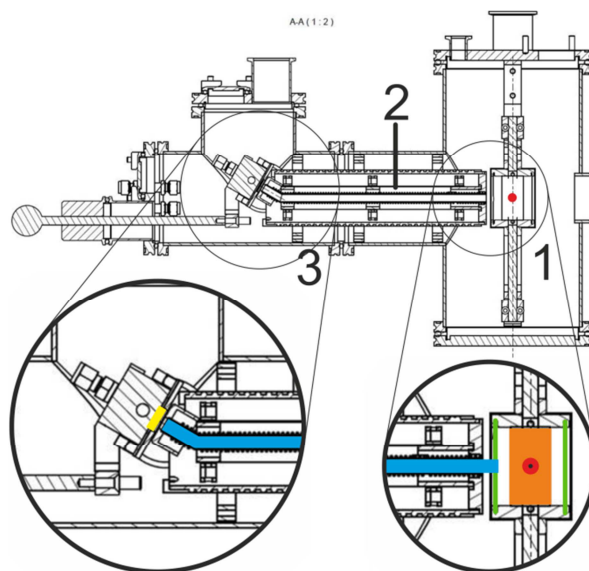
Fig. 1: The ISOL-IVAC exp. in the direction of the beam (●) with 1 the hot catcher foil in *orange* and Ta heat shield in *green*, 2 the isothermal chromatography part (quartz insert in *blue*) and 3 the 4-fold diamond detector (*yellow*). The size of the entrance hole is indicated as black dot (●) on the "beam spot".

A special thermocoax$^{®}$ oven with quartz inserts ($\varnothing_{in} = 6$ mm) was used as chromatography unit, providing isothermal temperatures between 300ºC to 920ºC. The diamond detector, with the active detection area facing the chromatography column exit in close proximity (≤ 5 mm), was mounted on a water cooled copper block and operated as described in [2].

The presented isothermal vacuum chromatography setup was successfully tested, among others [2] in an on-line chromatography experiment at the JAEA tandem accelerator facility (data analysis is ongoing).

_____

[1] A. Türler et al., Chem. Rev. **113**, 2 (2013).
[2] P. Steinegger et al., see this report, p. 6.
[3] H. Gäggeler et al., Radiochim. Acta **40**, 3 (1986).
[4] D. Wittwer et al., Nucl. Instrum. Methods Phys. Res. B **297** (2013).
[5] T. K. Sato et al., Rev. Sci. Instrum. **84**, 2 (2013).
[6] C. Droese et al., Nucl. Instrum. Methods Phys. Res. B **338** (2014).

THE ISOL – IVAC EXPERIMENT:
OPTIMIZATION STUDY

P. Steinegger, R. Eichler, A. Türler (Uni. Bern & PSI), M. Asai, Y. Kaneya, A. Mitsukai, Y. Nagame, T. K. Sato,
M. Schädel, S. Takeda, A. Toyoshima, K. Tsukada, A. Vascon (ASRC, JAEA, Japan), R. Dressler, D. Piguet (PSI)

The isothermal vacuum chromatography setup [1] was tested on-line for the first time using the model system of ^{184}Tl ($t_{1/2}$ = 10.3 s, Iα = 2.1%) on quartz. Several consecutive test experiments were performed to optimize the IVAC experiment. These efforts altogether serve as pilot studies for future vacuum chromatography experiments with short-lived ($t_{1/2}$ < 1 s), less volatile (-ΔH_{ads} > 47 kJ·mol^{-1}) superheavy elements (SHE), having a special focus on E113. Herein, we present one of the preparatory experiments, where Hf was utilized as hot catcher material, following suggestions by [2]. ^{184}Tl was produced and provided to the IVAC setup following the description in [1, 3]. Quartz inserts were used for both the hot catcher containment and the thermocoax® oven [4]. The latter was operated in a constant high temperature mode with T > 750ºC, whereas the release temperature (i.e. the hot catcher) was stepwise increased until a maximum at roughly around 1500ºC.
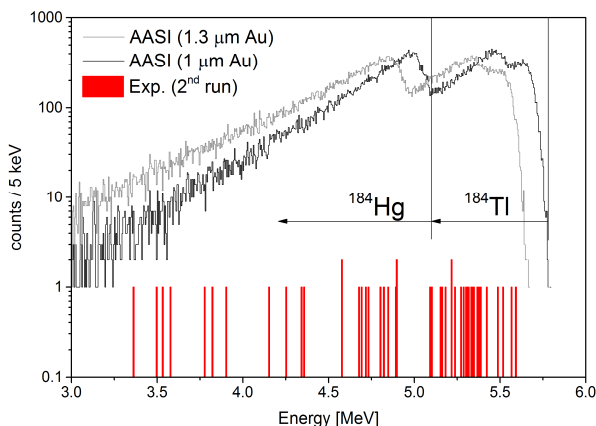
Fig. 1: Sum spectrum of the 2nd run (Hf hot catcher) with the experimentally obtained spectrum (red) and the simulations [5] for ^{184}Tl and ^{184}Hg on a 1 µm Au foil (black) and on a 1.3 µm Au foil (grey). The ROIs for ^{184}Tl and its β^+-decay daughter ^{184}Hg are indicated.

At the applied chromatography column temperatures, thallium is supposed to pass through without considerable retention. The α-decay of depositing ^{184}Tl was measured using the 4-fold diamond detector in combination with four CIVIDEC Cx spectroscopic shaping amplifiers (250 ns shaping time) [6] and a NIKI GLASS ADC/MCA readout system. A more detailed description of the detector and its operation condition is given in [1].A gold foil was covering the detectors preventing possible surface deposits during the benchmark runs (i.e. Au foil with a nominal thickness of 1 µm). In a 6.6 hours background measurement, no events were registered in the region of interest. The resulting sum spectrum of ^{184}Tl is shown together with simulations performed using the AASI code [5], taking into account the detector coverage (Fig. 1). Thus, it has been shown that ^{184}Tl reached in fact the detector. This involved the implantation and subsequent thermal release as well as the chromatographic process through the column. The gold foil was not perfectly flat thereby exceeding its ideal thickness, which explains the slight low energy shift of the measured alpha energies (see simulations in Fig. 1). The achieved transport efficiencies reached ≈10%. Partly, this can be explained by suboptimal collection efficiency on the detector (misalignment, too large distance to the column exit, etc.). Another more severe effect concerned the release out of the hot catcher foil. As revealed by post-experimental γ-spectroscopy of the longer-lived daughter ^{184}Ir ($t_{1/2}$ = 3.0 h), a considerable amount of implanted material was found to be retained within the hot catcher matrix. Several points of improvement were addressed during the update of the setup: 1) the verification and control of the hot catcher temperature in order to maintain stable release conditions; 2) introduction of various ISOL beam current monitoring possibilities (^{184}Tl input verification); 3) the optimization of the catcher-IVAC connection; 4) the improvement of the detector position adjustment.

The follow-up experiments performed in Fall 2014 revealed higher efficiencies for the release and chromatographic transmission of ^{184}Tl. First full on-line IVAC experiments have been performed. The data analysis is ongoing.

ACKNOWLEDGEMENT

[1] P. Steinegger et al., see this report, p. 7.
[2] D. Wittwer et al., Nucl. Instrum. Methods Phys. Res. B **297** (2013).
[3] T. K. Sato et al., Rev. Sci. Instrum. **84**, 2 (2013).
[4] A. Serov et al., Radiochim. Acta **101**, 7 (2013).
[5] T. Siiskonen et al., Nucl. Instrum. Methods Phys. Res. A **550**, 1-2 (2005).
[6] *CIVIDEC Instrumentation GmbH*, Wien, Austria.

CAN NITROGEN MONOXIDE REPLACE CARBON MONOXIDE FOR FORMATION OF VOLATILE COMPOUNDS WITH d-ELEMENTS?

H.W. Gäggeler, I. Usoltsev, R. Eichler (Univ. Bern & PSI)

Volatile carbonyls can be formed *in-situ* and under ambient condition with products from nuclear reactions in gas jet experiments if CO is added to an inert carrier gas (e.g. He) [1]. So far, group 6 to 9 elements have proven to react with CO: Mo, Tc, Ru and Rh but also their homologs in the next period: W, Re, Os, and Ir [2,3]. This reaction type was recently successfully applied to form Sg hexacarbonyls [4]. The question arose whether NO gas could also be applied for formation of volatile nitrosyl complexes with the same elements. NO has a similar electronic structure as CO, though it is well known that its oxidative capacity is higher compared to that of CO.

At the Miss Piggy ^{252}Cf spontaneous-fission source of Bern University gas-jet experiments were conducted with NO/He as well as with NO/CO/He gas mixtures. These measurements were complemented by studies with CO/He gas and pure He.

The data are summarized in Tab. 1. Figure 1 shows gamma spectra of volatile products transported out of the recoil chamber of Miss Piggy and deposited on the charcole trap. The spectra obtained with gas mixtures of 5vol-% CO in He and with 50vol-% NO in He are shown for comparison. As a primary result, no formation of volatile compounds with d-elements such as e.g. Mo with NO was observed. However, to our surprise, volatile compounds with iodine were detected - most likely nitrosyl iodide. As ^{252}Cf fission does not form with significant yield bromine, it could not be verified whether bromide compounds would also be formed with NO. Indeed, reaction of I with NO to form INO (in the inert gas Ar) has a rather high formation enthalpy (IUPAC recommended value, is $\Delta H° = -75.7$ kJ·mol^{-1}).

In a second series of experiments mixtures of NO and CO were used to study possible mixed nitrosyl-carbonyl compounds, as recently described for Tc and Re [5]. It turned out that no volatile compounds with d-elements (e.g. Mo, Tc) were observed.

In a final experiment with pure CO in He gas – to verify formation of volatile carbonyl compounds – it was found that also iodine was transported at 5%-vol % CO –He mixture, though at a lower yield compared to that with NO in He gas. At 50 vol-% CO iodine was not transported anymore.

To conclude, NO/He gas is well suited to separate iodine and probably also other halogens. Whether this gas mixture might also be applied for future separation of element 117 remains open. Element 117 should exhibit rather strong metallic properties similar to At, the first metallic halogen [6].

Otherwise the NO admixture to CO containing carrier gas significantly suppressed formation of volatile transition metal carbonyl compounds.

Tab. 1: Average yield for ^{136}I, ^{137}I, and ^{138}I observed in gas jet experiments with Miss Piggy during 1800 s accumulation.

Gas condition	Average yield $^{136-138}$I, %
50%NO/50%He	100*
10%NO/90%He	62±17
47.5%NO/5%CO/47.5%He	105±23
5%NO/5%CO/90%He	71±5
5%CO/95%He	32±6
50%CO/50%He	---
100%He	---

* All yields are normalized to the first experiment.
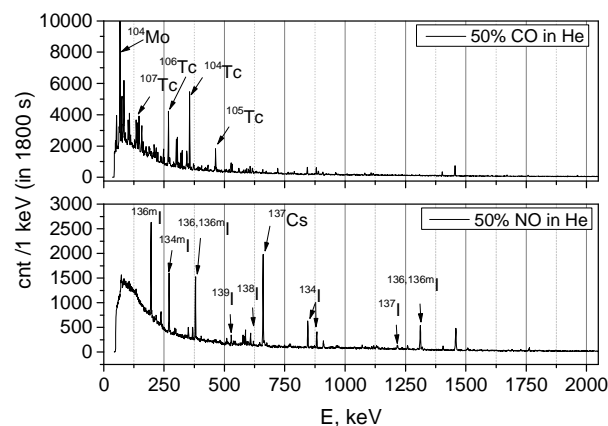
Fig. 1: γ–spectra accumulated from the charcoal trap applying 1:1 CO/He and NO/He transport gas mixtures. A selection of mainly transported nuclides is indicated, ^{137}Cs is accumulated as decay product of ^{137}I and ^{137}Xe on the trap used in the experiment with NO containing carrier gas.

[1] J. Even et al. Inorg. Chem. **51,** 6431, (2012).
[2] Y. Wang et al., Radiochim. Acta, **102** (1,2) (2014).
[3] J. Even et al., Radiochim. Acta **102**(12) 1093 (2014).
[4] J. Even et al., Science, **345,** 6203 (2014).
[5] D. Rattat et al., J. Organomet. Chem., **689**, 4833 (2004).
[6] A. Hermann et al., Phys. Rev. Lett., **111,** 116404 (2013).

TEFLON COVERAGE OF SILICON ALPHA DETECTORS

R. Eichler, I. Usoltsev, A. Türler (Univ. Bern & PSI)

The recently reported successful production of group 6 carbonyl complexes [1] and the chemical identification of $Sg(CO)_6$ [2] was possible because these complexes have a considerable thermodynamic stability [3] and a low reactivity towards inert and oxide covered surfaces [1]. The transition metals of groups 7-9 were reported to form volatile carbonyl molecules too [1]. Since some of these complexes are not obeying the 18-electron rule, will have a non-CO-ligand, or represent complex molecules with free electrons, their reactivity will be enhanced or their thermodynamic stability will be low. This fact is corroborated by investigations using fission product transition metals produced at the ^{252}Cf source at the University of Bern [4]. Figure 1 shows the probability to survive a transport through columns of different materials at room temperature for various carbonyl compounds. There was no decomposition observed in contact with Teflon® or polyethylene (PE).
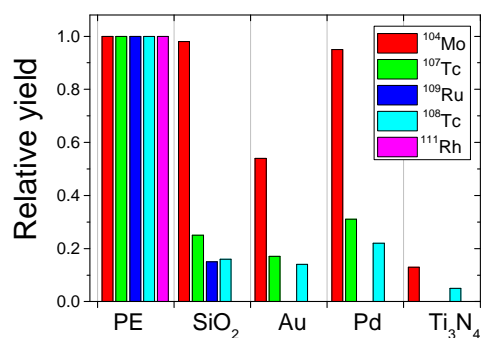
Fig. 1: Survival probability of carbonyl compounds in contact with various surfaces at room temperature.

The efficient non-destructive transport is of outmost importance in chemistry experiments with less stable transactinide complexes. We suggest here a method for covering surfaces with thin layers of Teflon. Fiber-coating with Teflon®-AF was already performed in [5]. DuPont^{TM} Teflon®-AF is an amorphous fluoroplastic that dissolves in the Fluorinert® solvent FC-40 [6]. A transparent 2% Teflon-AF 1600 solution in FC40 was prepared in a PE-Eppendorf® vial applying ultra-sonication for three hours. A 5 µl drop of the solution was placed on a microscopy glass and left for drying in air. A transparent thin layer of Teflon was obtained. Placing a water drop onto the covered surface (as shown in Fig.1 (A)) the surface revealed completely hydrophobic character. The following experiment was dedicated to reveal the chemical resistivity of the layer, proving also the homogeneity of the coverage. Therefore, a copper foil was covered with a thin layer of about 0.3 µm Teflon®-AF. A drop of concentrated HNO_3 was placed on the covered copper surface. As can be seen from Figure 2 (B, left) the chemical inertness and homogeneity of the surface coverage was fully proven, if compared to the behavior of the uncovered copper foil (Fig.1B right).

Fig. 2: (A) A drop of water placed on a Teflon-AF covered glass plate; (B) A drop of HNO_3 conc. placed on Teflon-AF covered (left) and uncovered (right) copper foils

These promising results encouraged us to try the same coverage with a silicon PIPS detector (Fig. 3A). The homogeneity of the layer thickness and alpha resolution was tested using the detector in a standard α-spectroscopy setup with a mixed nuclide standard source (see Fig. 3B). The number of layers indicates the number of wetting-drying cycles. The 1 µm layer was produced using a 5% solution of Teflon-AF 1600.
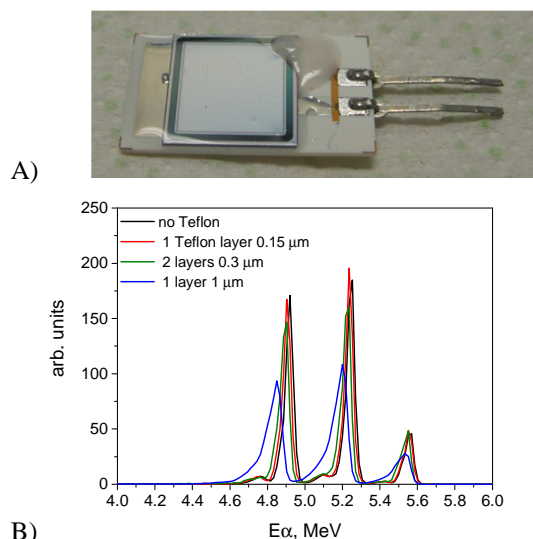
Fig. 3: (A) Silicon PIPS detector covered with a 1 µm thick layer of Teflon-AF. (B) Merged α-spectra of a ^{239}Pu, ^{241}Am, ^{244}Cm - mixed nuclide standard source recorded using Teflon-AF 1600 covered detectors.

The Teflon-AF thickness of the coverage can be controlled by using low concentration Teflon-AF solutions in FC40 applying a certain number of wetting and drying cycles. The obtained Teflon-AF 1600 coated silicon detector is suitable for high resolution alpha spectroscopy at chemically resistive homogeneous layer thicknesses.

[1]   J. Even et al. Inorg. Chem. **51,** 6431 (2012).
[2]   J. Even et al., Science, **345**, 6203 (2014).
[3]   C. S. Nash, J.Am.Chem.Soc., **121**, 10830 (1999).
[4]   I. Usoltsev, PhD Thesis, Univ. Bern (2014).
[5]   D. Han, A.J. Steckl, Langmuir 25, 9454 (2009).
[6]   http://www2.dupont.com/Teflon_Industrial/
      en_US/products/product_by_name/teflon_af/

UPTAKE OF ^{13}N-LABELLED N_2O_5 TO NITRATE CONTAINING AEROSOL

G. Gržinić (Univ. Bern & PSI), T. Bartels-Rausch (PSI), A. Türler (Univ. Bern & PSI), M. Ammann (PSI)

N_2O_5, a reactive intermediate of the night-time chemistry of nitrogen oxides, has been identified as one of the major reservoir species and potential sinks of NO_x [1]. Removal of N_2O_5 leads to a reduction of atmospheric NO_x and consequent reduction of tropospheric ozone and thus the oxidative capacity of the atmosphere. In presence of nitrate in the aerosol, the net uptake of N_2O_5 becomes suppressed because of reformation of aqueous N_2O_5 and its re-evaporation into the gas phase. This effect is referred to as the 'nitrate effect'. We have used the short-lived radioactive isotope ^{13}N to trace the exchange of ^{13}N-labelled N_2O_5 with the non-labelled nitrate pool in the aerosol phase, in order to estimate the bulk accommodation coefficient α_b.

In our experiments we used the short-lived radioactive tracer ^{13}N produced at PSI's PROTRAC facility [2]. ^{13}NO is mixed with non-labelled NO and O_3 in a gas flow reactor where N_2O_5 is synthesized under dry conditions. The N_2O_5 flow is fed into an aerosol fast-flow tube and mixed with a humidified aerosol prepared by ultrasonic nebulisation of a $NaNO_3$, Na_2SO_4 and a 1:1 $NaNO_3/Na_2SO_4$ solution. A movable injector is used to vary the reaction time in the aerosol fast-flow tube. A Scanning Mobility Particle Sizer (SMPS) system is placed behind the aerosol flow tube to characterize the aerosol. The remaining gas flow is then directed into a parallel plate diffusion denuder system, where the gaseous species can be selectively separated. The aerosol particles are trapped at the end of the denuder system on a particle filter. Gamma detectors placed on the denuder plates and the particle filter are used to monitor the activity of the trapped ^{13}N-labelled species.
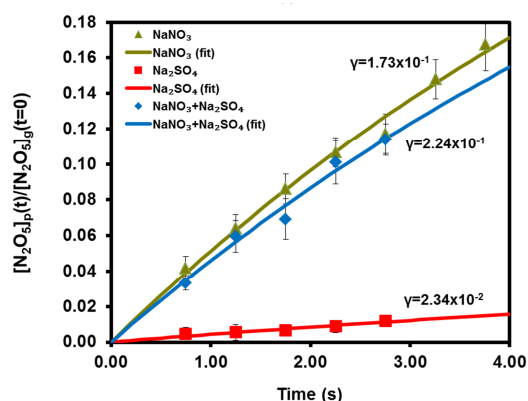
Fig. 1: Normalized particle-phase N_2O_5 concentration vs. time for an experiment performed at 70% RH.

Fig. 1 shows the measurements of the uptake coefficient (γ) of ^{13}N labelled N_2O_5 conducted at 70% RH. The resulting uptake values for the nitrate and mixed aerosols are significantly above those reported in previous studies [3], while the uptake to $NaSO_4$ aerosol is

consistent with uptake to aqueous particles without nitrate as reported earlier for non-labelled N_2O_5.

The different behaviour of labelled and non-labelled species can be assessed by explicitly tracking the ^{13}N tracer in the reaction mechanism as shown in Fig. 2. The left branch of the mechanism results in complete sequestration of the ^{13}N tracer into the nitrate pool present in the aerosol, because the back reaction of nitronium ion occurs with non-labelled nitrate, which is in large excess over the labelled nitrate. The right branch of the mechanism, where the ^{13}N tracer ends up on the nitronium ion, results in reformation and eventual evaporation of ^{13}N$_2O_5$ back into the gas phase. If the label is symmetrically distributed in the N_2O_5 molecule and if its dissociation is symmetric and not affected by an isotope effect, the true probability for uptake of N_2O_5 into the aqueous phase is about two times the one observed for the labelled N_2O_5 (about 0.2). This has allowed us to estimate the bulk accommodation coefficient (α_b) to be ≥ 0.4, which is at least an order of magnitude above previous estimates.
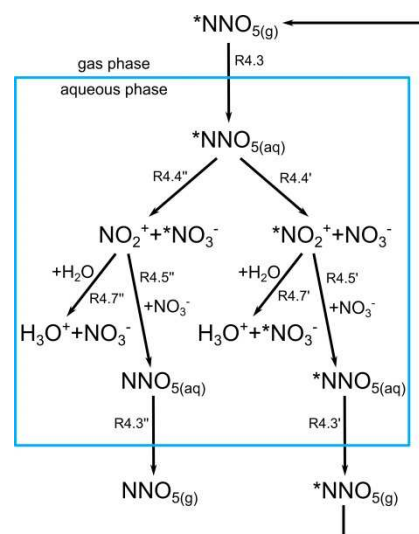
Fig. 2: The chemical mechanism of ^{13}N-labelled N_2O_5 hydrolysis

[1] Abbatt, J. P. D., et al., Chem. Soc. Rev., **41**, 6555-6581 (2012).

[2] Ammann, M., Radiochim. Acta, **89**, 831 (2001).

[3] Hallquist, M., et al., Phys. Chem. Chem. Phys., **5**, 3453-3463 (2003).

ORGANIC NITRATE FORMATION DURING GROWTH OF α-PINENE SECONDARY ORGANIC AEROSOL

T. Berkemeier, U. Pöschl, M. Shiraiwa (MPIC), G. Gržinić (Univ. Bern & PSI), M. Ammann (PSI)

Secondary organic aerosol (SOA) particles are formed by oxidation of volatile organic precursors by atmospheric oxidants such as ozone, NO_3 and OH radicals. Nitrogen oxides (NO, $NO_2 \equiv NO_x$) have been shown to affect the underlying chemistry by formation of organic nitrates [1,2] (cf. Fig. 1) and thus alter the total mass yield. However, the formation and partitioning of nitrogen containing compounds into SOA particles is still poorly understood since organic nitrate contents are difficult to quantify with standard analytical tools. Our collaboration unites a suitable experimental method available at PSI and new advances in the numerical description of growing particulates to unravel the kinetics of the process.
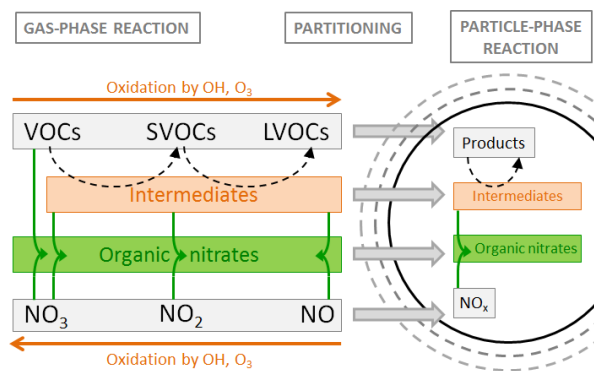
Fig. 1: Schematic representation of SOA formation, involving oxidation of volatile organic compounds (VOCs) to semi and low volatility organic compounds (SVOCs and LVOCs), which partition into the particle phase (grey arrows). Intermediates may react with nitrogen oxides to form organic nitrates in both, gas and particle phase (green arrows).

We use the short-lived radioactive tracer ^{13}N produced by PSI's PROTRAC facility [4] to quantify the amount of organic nitrates produced and retained in SOA particles. SOA particles nucleate homogeneously during either dark ozonolysis or OH photooxidation of α-pinene precursor gas (~ 500 ppb) by feeding varying mixtures of these trace gases into an aerosol flow tube system. The ^{13}N labelled molecules are introduced as ^{13}NO in the ozonolysis or HO^{13}NO in the photooxidation experiments, respectively. OH radicals form during the photodissocation of HONO under irradiation with UV lamps centred at 350 nm, also releasing the labelled nitrous oxide ^{13}NO. HONO is prepared by reduction of NO_2 gas over a surface of ABTS (diammonium salt of azino-bis(ethylbenzothiazoline-sulfonic acid)). The length of the aerosol flow tube can be adjusted via movable inlets. A Scanning Mobility Particle Sizer (SMPS) system is placed behind the aerosol flow tube to determine the size distribution. The remaining gas flow is then directed into a detection system that separates gas and particle phase species and detects the trapped labelled nitrogen compounds via scintillation counters.

A comparison of the time dependence of particle mass, particle number and organic nitrate content reveals that organic nitrate contents are substantial throughout, but seem to play a major role in the initial formation phase (Fig. 2).
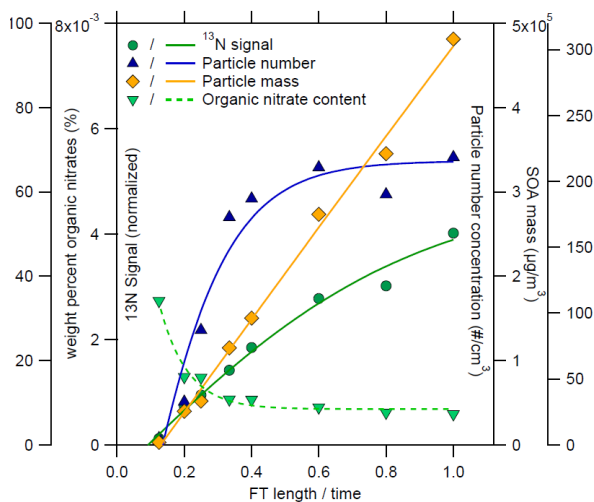
Fig. 2: SOA mass (orange diamonds), normalized ^{13}N signal (green circles), particle number concentration (blue upward triangles) and organic nitrate content (green downward triangles) in the particle phase as function of residence time in the flow tube reactor during an OH photooxidation experiment. The solid lines are to guide the eye.

Our measurements show that while new particle formation ceases quickly in the flow tube reactor, particle mass continues to increase over the full experimental time scale. Analogously, nitrogen oxides are taken up effectively into the particle phase and persist in the form of organic nitrates. As organic precursor, nitrogen oxides and oxidants (O_3 / OH) get depleted in the flow reactor, the rate of formation of organic nitrates decreases. The quantitative results suggest that a large fraction (> 10 %) of organic molecules in SOA may exist in a nitrated form.

[1] Ziemann, P.J., and Atkinson, R., Chem. Soc. Rev., **41**, 6582–6605 (2012).

[2] Renbaum, L. H., and Smith, G. D., Phys. Chem. Chem. Phys., **11**, 8040–8047 (2009).

[3] Shiraiwa *et al.*, Atmos. Chem. Phys., **12**, 2777–2794 (2012).

[4] Ammann, M., Radiochim. Acta, **89**, 831 (2001).

RADICAL PRODUCTION FROM THE PHOTOSENSITIZATION OF IMIDAZOLES

P. Corral Arroyo (Univ. Bern & PSI), L. González , R. Volkamer (CU), S. Steimer, T. Bartels-Rausch,
M. Ammann (PSI)

HO_x radicals largely control the oxidative capacity of the troposphere. This project studies the HO_x radical production from the photochemistry of imidazole-2-carboxaldehyde (IC). Imidazoles are light absorbing products of glyoxal multiphase chemistry and can behave as photosensitizers [1,2]. First experiments have shown that significant HO_2 production may occur in presence of citric acid (CA) as an electron or H atom donor.

Experiments were performed in a photochemical flow tube reactor, where IC/CA films were exposed to a flow (1.5 l min^{-1}) of NO (up to 1 ppmv) in N_2/O_2 (up to 2:1) at atmospheric pressure and relative humidity (RH) between 0 and 60 %. The NO_2 and HONO produced was measured by the difference between NO signals of a chemiluminescence detector (CLD), w/o a molybdenum converter (for conversion of NO_2 to NO) and w/o a HONO trap in line.
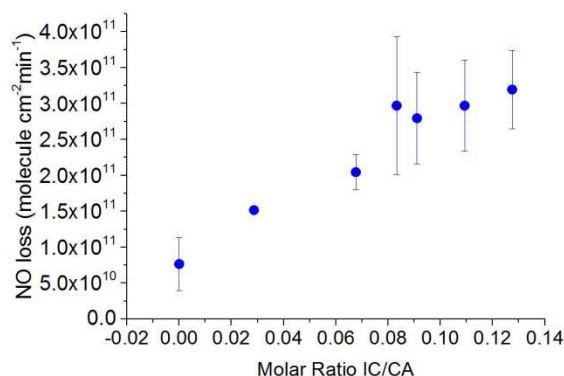
Fig. 1: Correlation between the molar ratio of IC and CA in the film and NO loss (molecule $cm^{-2}min^{-1}$).

The amount of NO molecules reacted per unit film area and time presented in Fig.1 is related to the amount of NO_2 and HONO produced in the reactor, and are thus also related to the amount of HO_2 produced in the film. The ratio NO_2/HONO was observed to be ~1.2 in an experiment at 360 ppb NO, 17.7°C and 55% RH.

The likely fate of the excited IC (see suggested mechanism in Fig. 2) is to transfer an H atom from a donor (e.g., CA) to O_2 yielding HO_2 and recycling the IC. HO_2 thus produced reacts with the excess NO to form NO_2 that is measured. HONO may form in the reaction of NO with OH produced in the reaction of NO + HO_2, with OH directly produced in the film (not shown), or if H atom transfer occurs to NO_2 (not shown). According to the preliminary HONO measurements, the amount of NO_2 and HONO produced are the same, indicating that in presence of O_2, the production of HO_2 dominates over the direct conversion of NO_2 to HONO.
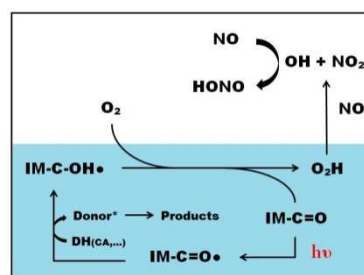
Fig. 2: Proposed mechanism of the reaction based on refs [3,4]. The donor (DH) could be citric acid but IC or contaminations as well.
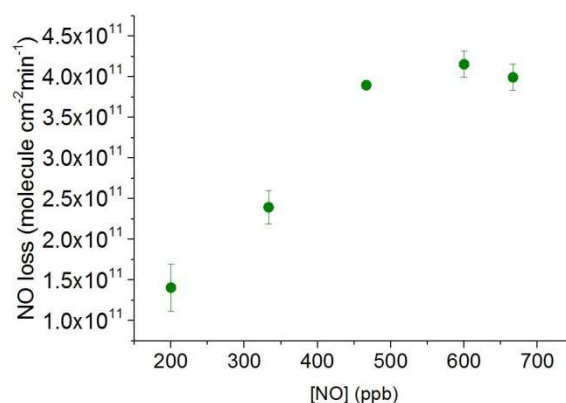
Fig. 3: The variation of the number of NO molecules reacted with the concentration of NO in the reactor for a film with a molar ratio of 0.09.

In order to check the scavenging efficiency of HO_2 by NO, we measured the NO loss as a function of NO concentration, which levels off above about 500ppb. At this concentration, the life time of HO_2 with respect to its reaction with NO becomes short enough (8.5 ms) to ensure complete conversion.

Further preliminary experiments on the humidity dependence are available; the dependence of the reactivity with the actinic flux has been demonstrated in last years' experiments. In conclusion, HO_2 is produced from the photochemistry of IC in the CA+H_2O matrix. A more detailed analysis will have to disentangle the other contributions to radical production and analysis of the products of reaction by HPLC as well.

[1] Kampf et al., Atmos. Chem. Phys., **12**, 6323-6333 (2012).
[2] Aregahegn et al., Faraday Discussions, DOI: 10.1039/C3FD00044C (2013).
[3] Canonica et al., Environ. Sci. Technol., **29**, 1822-1831 (1995).
[4] George et al., Faraday Discussions., **130**, 195-210 (2005).

DIFFUSION OF WATER IN SHIKIMIC ACID

S. Steimer (ETHZ & PSI), A. Huisman, U. Krieger, D. Lienhard, C. Marcolli, T. Peter (ETHZ), M. Ammann (PSI)

Atmospheric organic matter can adopt an amorphous solid state [1]. Diffusivity gradually decreases from liquid to amorphous solid states, so that transport within the bulk is delayed in solid and semi-solid material. For water soluble material, the change in physical state is affected by both temperature and relative humidity (RH), due to water acting as a plasticizer. Shikimic acid is a plant metabolite, which can be found in biomass burning aerosol [2]. We used an electrodynamic balance (EDB) to determine the physical state of aqueous shikimic acid particles as well as the associated changes in water diffusivity as a function of temperature and humidity.

Single shikimic acid particles were generated from a 2.5 wt-% solution of shikimic acid in Milli-Q water using an ink jet cartridge. The charged particle is then levitated in the electric field of the EDB. Four independent methods were used to characterize the aerosol particle: (i) the DC voltage applied to compensate the gravitational force is proportional to and a measure for the mass change of the particle; (ii) the two-dimensional angular scattering pattern was measured over a scattering angle and used to estimate the radius of the particle and to detect phase changes; (iii) low resolution Mie resonance spectroscopy with a LED-white-light source for illumination was used to follow the radius change of spherical particles (e.g. liquid droplets) (iv) high resolution Mie resonance spectroscopy with a tunable diode laser was used to measure size and refractive index simultaneously with high precision.

Figure 1 shows the humidogram of shikimic acid at 20°C. The particle stayed spherical through the whole measurement, indicating that no crystallization occurred at any humidity. At low humidities (<40% RH), the particle is not in thermodynamic equilibrium, as hysteresis loops are apparent when cycling RH. This suggests strong impedance to water uptake and release and can be used to retrieve water diffusion coefficients by modelling the growth behaviour with a numerical diffusion model [3]. The parameterizations of the diffusion coefficient of water, D_w, which yield the best fit to experimental data at the different temperatures are then used to obtain a global fit (Fig. 2), which is described by a modified Vignes-type equation:

$$D_w = (D_w^0)^{x_w \alpha} (D_s^0)^{1-x_w \alpha}, \qquad (1)$$

where D_w^0 is the diffusion coefficient of pure water, D_s^0 the diffusion coefficient of pure shikimic acid, x_w the mole fraction of water and α an empirical correction parameter. At the lowest temperature (-23°C) the difference in D_w is more than 13 orders of magnitude between the lowest and highest RH.
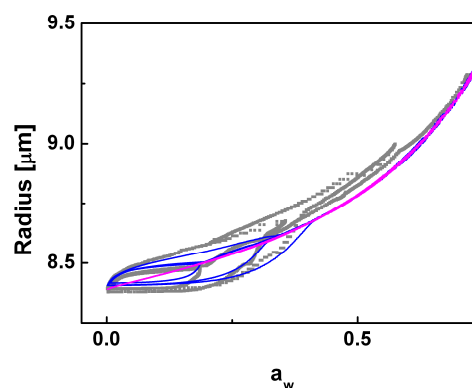
Fig. 1: Particle size as a function of water activity in the gas phase: experimental data (grey squares) as well as diffusion model results without transport limitation ($D_w = 10^{-11}$ m²/s, pink line) and with optimized parameterization of the diffusion coefficient (blue line).
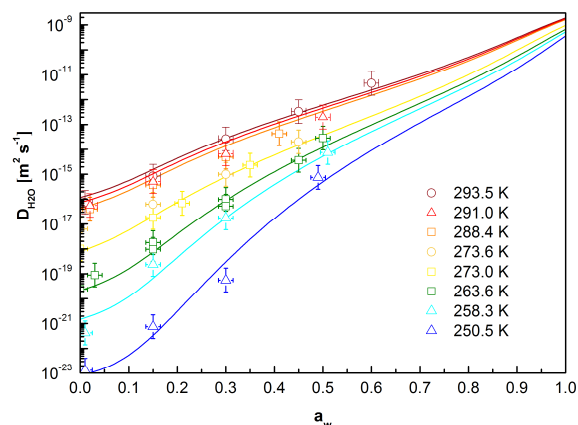
Fig. 2: Water diffusion coefficient as a function of water activity for the investigated temperatures indicated by different colours. Different symbols represent different particles. The lines represent fits to eq. (1).

_____

[1]   A. Virtanen et al., Nature, **467**, 824 (2010).
[2]   P. M. Medeiros et al., Environ. Sci. Technol., **42**, 8310 (2008).
[3]   B. Zobrist et al., Phys. Chem. Chem. Phys., **13**, 3514 (2011).

O₃ UPTAKE TO MIXTURES OF SODIUM BROMIDE AND CITRIC ACID SOLUTIONS

M.T. Lee, A. Türler (Univ. Bern & PSI), M. Ammann (PSI)

The ocean surface water and sea spray aerosol derived therefrom contain a complex mixture of not only inorganic salts but also organic compounds deriving from marine biota [1]. In the context of the present study, an important aspect of organics is that they may have a significant effect on the way halide ions are distributed at the interface and may thus affect their reactivity [2]. Therefore, the goal of the present study was to understand the effect of an organic compound on the reaction of gaseous O₃ with a NaBr solution using a flow reactor approach.

Experiments were done with an atmospheric pressure flow reactor setup in which the solution of interest is contained in a shallow trough, over which a gas containing O₃ is passing. The reactor has planar geometry (Fig. 1) and it has cooling coils to allow circulating a thermo-stated fluid to control the temperature. The latter was set to 15.7 °C to allow operation at saturated conditions with respect to water vapor inside the flow reactor, and to avoid high humidity in gas lines upstream, downstream and within the O₃ analyzer. The liquid surface is 27.5 mm wide and 398 mm long. The thickness of the liquid can be varied from 0.8 to 1.5 mm which is significantly larger than the reacto-diffusive length (max few µm) of O₃ under all conditions.
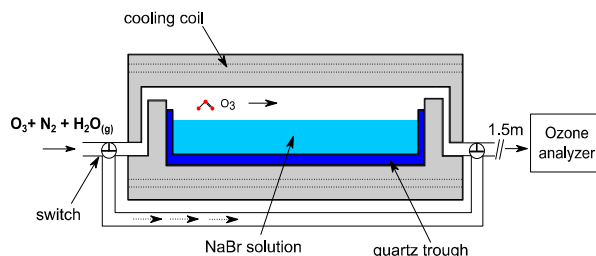
Fig. 1: A Schematic diagram of flat-bed reactor used in O₃ uptake measurements to the NaBr solution filled on a quartz trough.

Figure 2 presents the O₃ uptake coefficient as a function of the square root of the bromide concentration in presence of 2.5 M CA and at two O₃ concentrations in the gas phase. The solid lines lines represent the expected behavior for γ based on the measurements on neat NaBr solution (blue), the acid catalyzed mechanism (green) [3] and an additional increase in solubility of O₃ (red) [4]. The dashed curve represents the sum of the acid catalyzed bulk reaction and a surface reaction component. We did not see a significant dependence on the O₃ concentration.

To discuss the enhanced reactivity of the solutions in presence of citric acid, we consider two scenarios: i) if we accept the linear dependence of γ of the square root of the bromide concentration as an indication of reactio-diffusive uptake into the bulk, the slope of the increase of γ with bromide concentration is determined

by the product: $H \times [k_b^{II}]^{1/2}$. Therefore, within this scenario, we need to discuss changes in the solubility (H, Henry's law constant) or the second order rate constant. ii) In the second scenario we consider the option that the difference between the observed reactivity and that explained by the bulk reaction is partly or completely driven by a surface reaction as suggested by Oldridge and Abbatt [5].
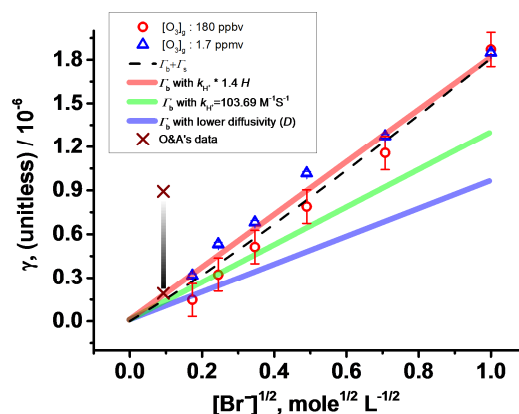
Fig. 2: Measured γ vs $[Br^-]^{1/2}$ for mixed NaBr–citric acid aqueous solutions at 15.7 °C. The dataset by Oldridge and Abbatt is represented by the two crosses and the vertical bar with the grey scale applied to symbols represents the O₃ concentrations (the darker the higher).

We concluded that the uptake kinetics of O₃ to neat NaBr solutions is consistent with bulk reaction limited uptake. In presence of citric acid, bulk reaction limited uptake is still a likely scenario, where the enhanced reactivity may be explained by an acid catalyzed mechanism and possibly an increase in solubility of O₃. The uncertainty in the underlying kinetic parameters leaves room for a surface reaction.

_____

[1]   O'Dowd et al., Nature, **431**, 676-680 (2004).
[2]   Krisch et al., J. Phys. Chem. C., **111**, 13497-13509 (2007).
[3]   Liu et al., Inorg. Chem., **40**, 4436-4442 (2001).
[4]   Bin et al., Ozone-Sci. Eng., **28**, 67-75 (2006).
[5]   Oldridge and Abbatt, J. Phys. Chem. A., **115**, 2590-2598 (2011).
[6]   Lee et al., J. Phys. Chem. A., DOI: 10.1021 /jp510707s (2014).

THE AQUEOUS SOLUTION–AIR INTERFACE AS SEEN FROM X-RAY PHOTOELECTRON SPECTROSCOPY

M. T. Lee (Univ. Bern & PSI), F. Orlando (PSI), M. A. Brown (ETHZ), S. Kato (PSI), A. Kleibert (PSI/SLS), A. Türler (Univ. Bern & PSI), M. Ammann (PSI)

The aim of the experiments was to obtain surface chemical composition information of mixed halide/ organic acid solutions of relevance to atmospheric chemistry in marine environments with X-ray photoelectron spectroscopy (XPS) on a liquid micro-jet (LJ). The surface composition of sea spray particles is crucial in the chemistry with gas phase oxidants [1,2]. Organics present at these interfaces derive from surface active degradation products of marine biota accumulating at the ocean surface. Here we use citric acid (CA) as a proxy for these.

We made use of the near ambient pressure photoemission endstation (NAPP) with the liquid microjet setup [3]. Measurements were made at the SIM beamline at SLS. A complete description of the equilibrated nature of a liquid microjet under the conditions of photoemission experiments has been described in the literature previously [4].
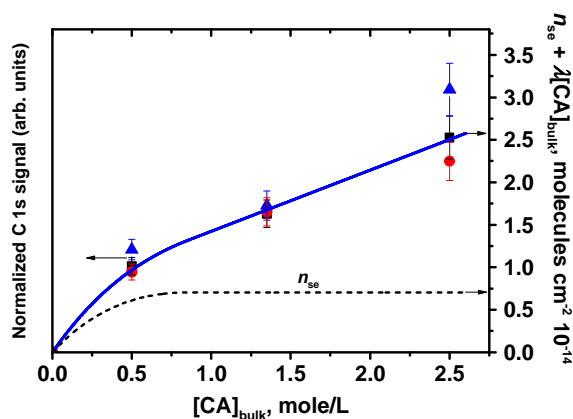
Fig. 1: Normalized C 1s photoemission signals as a function of citric acid concentration for three different NaBr concentrations.

Figure 1 shows the normalized C 1s PE signal as a function of the citric acid bulk concentration and for the three different NaBr concentrations. The blue solid line represents the simulated photoemission signal [5]. The dashed line represents the surface excess n_{se}, derived from surface tension measurements. The photoemission signal was calculated from the bulk phase CA (represented by the CA bulk concentration, $[CA]_b$, times the electron inelastic mean free path, λ) and its surface excess. It demonstrates that citric acid exhibits weak surfactant behavior. Figure 2 summarizes the contrasting behavior of bromide and sodium cation according to the measured PE signals, which are plotted as relative departure of the normalized Br 3d and Na 2s PE signals from that of the neat NaBr solution with the same bromide and sodium concentration, respectively, as a function of the citric acid concentration in the bulk. Therefore, citric acid leads to a relative depletion of bromide at the interface. In turn, Na

cations seem to be attracted more towards the interface.
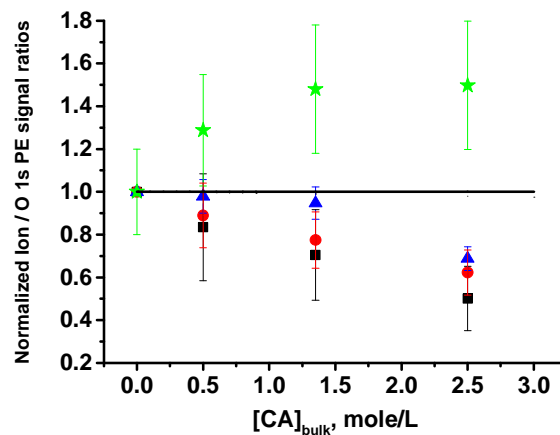
Fig. 2: Relative change of Br 3d and Na 2s photoemission signals as a function of citric acid concentration for 0.03 M (squares), 0.06 M (circles), 0.12 M (triangles) NaBr concentrations. For Na 2s, only data for 0.12 M NaBr are shown (stars). The horizontal solid line illustrates the behavior expected for the bulk solution for reference.

The photoelectron spectroscopic investigation of the solutions by LJ-XPS demonstrates that citric acid exhibits weak surfactant behavior in line with known surface tension data and suppresses bromide at the interface. Interestingly, the abundance of the sodium cations increased in presence of citric acid possibly through specific interactions of sodium with the alcohol or carboxylic acid groups of citric acid suggested before. These subtle effects of an organic surfactant on the changing structure at the interface do not allow to conclusively clarify the role of organics on interfacial reactivity in general [6].

[1] Donaldson and George, Environ. Sci. Technol., **46**, 10385-10389 (2012).
[2] Oldridge and Abbatt, J. Phys. Chem. A., **115**, 2590-2598 (2011).
[3] Brown et al., Rev. Sci. Instrum., **84**, art. no. 073904 (2013).
[4] Winter et al. Chem. Rev., **106**, 1176-1211 (2006).
[5] Pruyne et al. J. Chem. Phys. C., DOI: 10.1021/jp5056039 (2014).
[6] Lee et al., J. Phys. Chem. A., DOI: 10.1021/jp510707s (2014).

A NOVEL ANALYSIS CHAMBER FOR NEAR AMBIENT PRESSURE XPS OF SOLID SURFACES FOR ENVIRONMENTAL AND CATALYSIS RESEARCH

F. Orlando (PSI), A. Waldner (PSI & ETHZ), M. T. Lee (PSI & Univ. Bern), M. Birrer,
T. Bartels-Rausch (PSI), C. Proff (PSI/LBK), J. van Bokhoven (PSI/LSK & ETHZ), M. Ammann (PSI)

Ambient pressure X-ray photoelectron spectroscopy (APXPS) is a powerful tool to investigate elemental composition and chemical specificity of solid and liquid surfaces, which offers tremendous opportunities in environmental science and heterogeneous catalysis research [1]. In the following we provide an outlook of the new analysis chamber for the near ambient pressure photoemission (NAPP) endstation that has been recently build up by our group and collaborators at PSI and ETH Zurich for in situ spectroscopy at SLS [2].
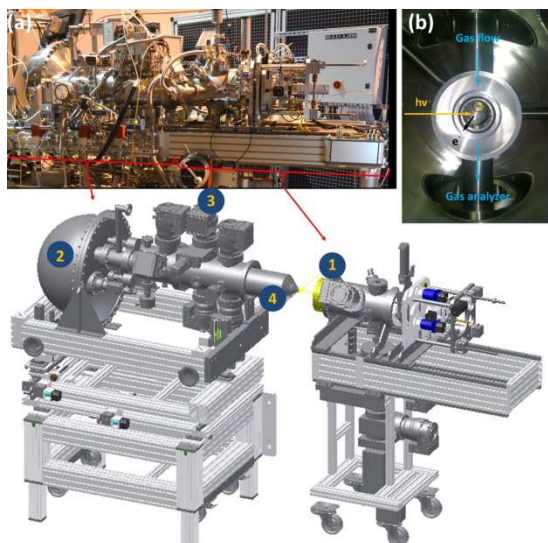
Fig. 1: (a) Schematic of the NAPP endstation with the solid chamber set-up and (b) view of the reaction cell surrounded by the UHV chamber. See text for details.

A schematic of the endstation is depicted in Fig. 1a, showing: the new chamber for solid samples (1), the Scienta R4000 HiPP-2 electron energy analyzer with CCD detector (2), the differential pumping on the electron lens and pre-lens (3) that allows XPS and NEXAFS measurements up to 20 mbar over a wide kinetic energy range (5-7000 eV), and the exchangeable entrance front cones (4). The whole endstation is mounted on a frame allowing easy movement and fine alignment. The new analysis chamber for solid samples is a vertically aligned flow tube with minimized internal surface area that enables dosing chemically reactive sticky gases with reduced wall effects (Fig. 1b). A high sensitivity mass spectrometer is mounted directly at the lower exit of the flow tube. The flow tube with the analysis cell is surrounded by an external UHV chamber connected through a bypass. This design allows to quickly vary the pressure at the sample so that both UHV and high pressure measurements can be performed one after the other in the same analysis chamber.

The wide sample temperature range (150-1300 K) enables in situ experiments for a number of applica-

tions in environmental research: with temperatures below ambient, high relative humidity (RH) conditions can be reached at still reasonably low water partial pressure, allowing to address surface chemical composition also under atmospherically relevant conditions.
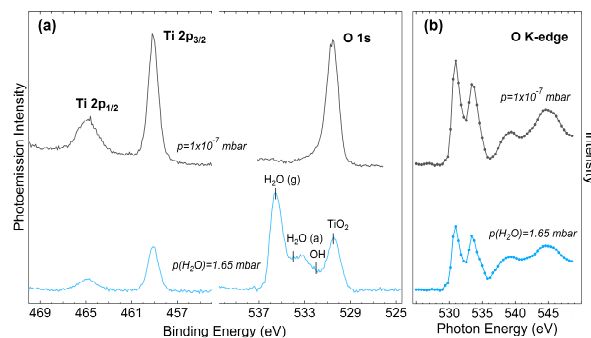
Fig. 2: TiO_2 powder (Degussa P25) on Au foil. (a) Photoemission spectra of Ti 2p and O 1s core levels measured at 650 and 730 eV photon energy, respectively, and (b) NEXAFS O K-edge spectra for the as-prepared sample (grey) and in 1.65 mbar H_2O (blue).

We have tested the solid chamber set-up in a water adsorption experiment on a TiO_2 powder sample. Fig. 2a shows the Ti 2p and O 1s spectra measured for the as-prepared sample and in 1.65 mbar H_2O at 270 K, corresponding to about 30% RH. With reference to the main peak at 530.5 eV binding energy (BE) indicative of O in a TiO_2 environment, several oxygen components appear upon water vapor exposure corresponding to OH and molecular water at about 532 and 534 eV, respectively [3], besides an additional peak at higher BE associated with gas-phase water. Fig. 2b shows the O K-edge NEXAFS: the resonances located at 531.3 and 534.0 eV are characteristic of TiO_2 and correspond to excitations to mixed states derived from O 2p and Ti 3d states, while the features between 537 and 550 eV are due to the covalent mixing of O 2p and Ti 4sp states [4].

[1] D. E. Starr et al., Chem. Soc. Rev., **42**, 5833 (2013).
[2] M. A. Brown et al., Rev. Sci. Instr., **84**, 073904 (2013).
[3] G. Ketteler et al., J. Phys. Chem. C, **111**, 8278 (2007).
[4] V. S. Lusvardi et al., Surf. Sci., **397**, 237 (2008).

FIRST XPS ANALYSIS OF
THE INTERACTION OF ACIDIC TRACE GASES WITH ICE AT SLS

A. Waldner (ETHZ & PSI), F. Orlando (PSI), T. Huthwelker (PSI/SLS), M. Birrer, M. Ammann,
T. Bartels-Rausch (PSI)

Uptake of atmospheric trace gases to the surfaces of cirrus clouds or to snow can modify the composition of the atmosphere and can play an integral role in transferring gases to and from the atmosphere [1,2]. Better knowledge of this process will help with the interpretation of concentration profiles in ice cores and with improving atmospheric chemistry models. The aim of this project is to examine the adsorption of acidic trace gases to ice surfaces on a molecular level with the near ambient pressure photoelectron endstation (NAPP). Earlier photoelectron studies have detected adsorbed acetic acid at the ice surface and indicated that the acid is confined to the uppermost ice layers [3].
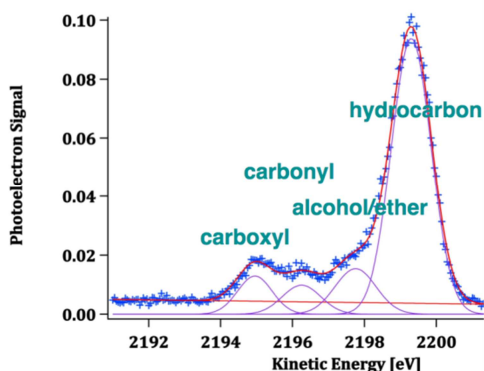
Fig. 1: Photoelectron spectrum (crosses) of the surface of an ice sample in presence of formic acid at T=243. Also shown is a reconstruction of the spectrum (red line) based on fitting 4 distinct features (purple lines).

Figure 1 shows a typical spectrum at 2500 eV nominal photon energy taken at the Phoenix beam line of the Swiss Light Source (SLS). The kinetic energy range of the detected photoelectrons reveals a binding energy of roughly 290 eV corresponding to the C1s level. The ice sample was formed in-situ by depositing water from the gas phase on a sample holder at ~190 K. After 1 hour, when the film reached a thickness of ~0.5 mm, the sample is warmed to 243 K and exposed to formic acid. During the measurements the ice sample is kept stable by maintaining a total water vapour pressure of 0.2 mbar.

The C1s spectrum (Fig. 1) reveals 4 distinct features at kinetic energies of 2199, 2198, 2196, and 2195 eV. Such shifts in kinetic energies are caused by chemical bonds that modify the energy levels of the core electrons. Based on typical chemical shifts in the C1s spectra of organic samples, we assign the following functional groups: Aliphatic carbons at 2199 eV kinetic energy, while alcohol or ether groups, carbonyl, and carboxyl appear in this order towards lower kinetic energy (higher binding energy). The carboxyl feature

at 2195 eV showed a strong response to changes in the dosing rate of formic acid, confirming the first observation of formic acid adsorbed to ice samples by photoelectron spectroscopy. The other features are either caused by adventitious carbon that might be produced in-situ by radiation chemistry or by other contaminations of volatile organics.

The Phoenix beam line allows acquiring C1s spectra with photon energies of up to 6800 eV. This results in increasing kinetic energies of the detected photoelectrons of up to 6500 eV. This allows taking measurements at varying probing depths, as the inelastic mean free path (IMFP) of electrons in ice increases with increasing kinetic energy (green line, Fig. 2).
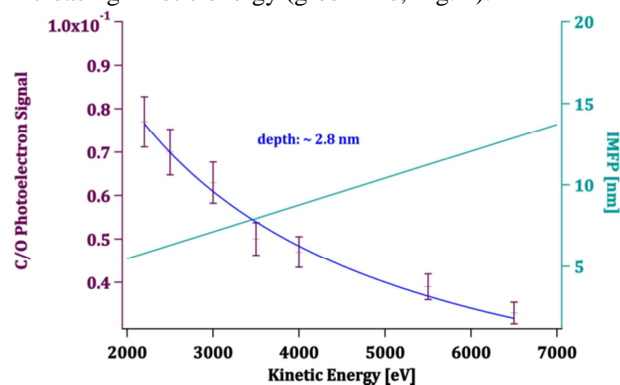
Fig. 2: Depth profile of formic acid dosed on ice (purple plus). Error bars represent random errors.

Figure 2 shows the ratios of C1s (carboxyl component only) to total O1s photoelectron signals as a function of electron kinetic energy (plus symbols). The blue line represents a fit from a simple two-layer model from which the thickness of the layer into which formic acid enters the ice (depth) can be derived [3]. The thickness of 2.8 nm indicates that formic acid stays at the surface.

We are in the process of evaluating the spectra in detail and our aim is to do further measurements with an improved setup.

---

[1] T. Huthwelker et al., Chem. Rev., **106**, 1375-1444 (2006).
[2] F. Dominé et al., Science, **297**, 1506-1510 (2002).
[3] A. Křepelová et al., J. Phys. Chem. A, **117**, 401-409 (2013).

PROVENANCE OF LEAD POLLUTION FROM Pb ISOTOPES IN AN ILLIMANI CORE

A. Eichler, L. Tobler, G. Gramlich (PSI), T. Kellerhals (KUP), M. Schwikowski (PSI & Univ.Bern)

Temporal changes in Pb isotopes have been successfully used to trace the provenance of Pb pollution and to differentiate between natural and anthropogenic Pb sources (e.g. [1]).

A 2000 year record of Pb enrichment factors (EFs) from Illimani glacier in Bolivia documents the history of anthropogenic Pb pollution in South America from pre-colonial mining/smelting during periods of Tiwanaku/Wari cultures and Inca empires, post-colonial metallurgical activities at the Altiplano, and leaded gasoline [2] (Fig. 1). To distinguish between the different Pb sources, isotopic ratios $^{206}Pb/^{207}Pb$ and $^{208}Pb/^{207}Pb$ were determined. The ice core $^{206}Pb/^{207}Pb$ ratio did not change significantly during AD 0-2000. This is due to a similar $^{206}Pb/^{207}Pb$ ratio of Bolivian background dust and local ores [3] (Fig. 1). Likewise, the $^{208}Pb/^{207}Pb$ ratio does not show temporal variations in the period AD 0-1960. Thus, the Pb isotopic fingerprint during AD 0-1960 is not suited to distinguish between different sources of pollution at the study site.
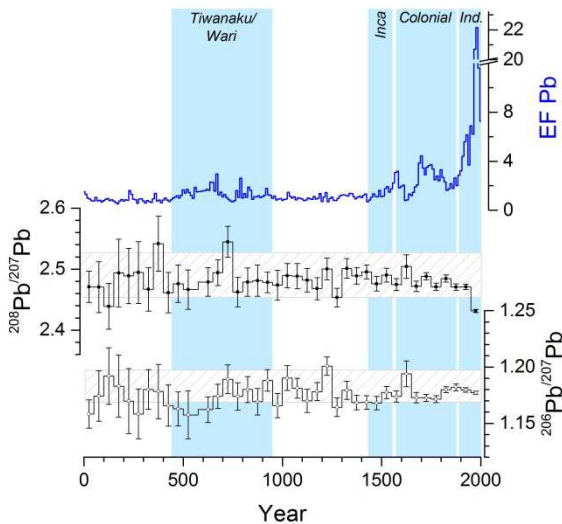
Fig. 1: Ice core records of Pb EFs (10 year medians) and Pb isotope ratios (50-year means ± 1 std err). The hatched areas mark the background range for Bolivia (local dust and soils, Porco and Cerro de Potosí mine tailings) [3].

Only from the 1960s onward the $^{208}Pb/^{207}Pb$ ratio is lower than the Bolivian dust and ore background (Figs. 2, 3), due to an input of non-local anthropogenic Pb primarily from leaded gasoline. Simultaneously, during the second half of the twentieth century, Pb EFs reveal the highest values of the past 2000 years. Historical emission estimates suggest that emissions from leaded gasoline dominate Pb pollution in South America during AD 1962-99, accounting for about two thirds of total Pb emissions [4]. The range of the Illimani Pb isotopic composition in the period AD 1965-2000 is similar to that of aerosols in Northern Chile, Argentina, and Brazil in the period AD 1994-99 [5] (Fig. 3). After 1994 leaded gasoline was still used

in Chile and Argentina, whereas it was already phased-out in Brazil. The similar isotopic range of aerosols from Northern Chile and Brazil in the 1990s indicates that Pb emissions from leaded gasoline and industrial processes (mainly metallurgy) in Middle South America can isotopically not be distinguished, but have a different composition than the background dust and the ores in Bolivia (Fig. 3).
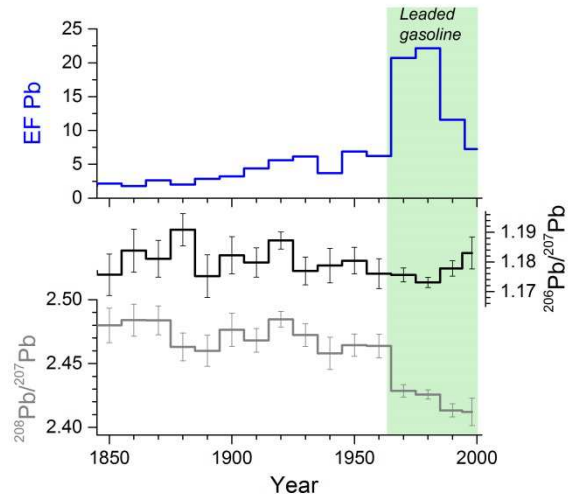
Fig. 2: Records of Pb EFs (10 year medians) and the Pb isotopic ratios (10 year averages ± 1 std err).
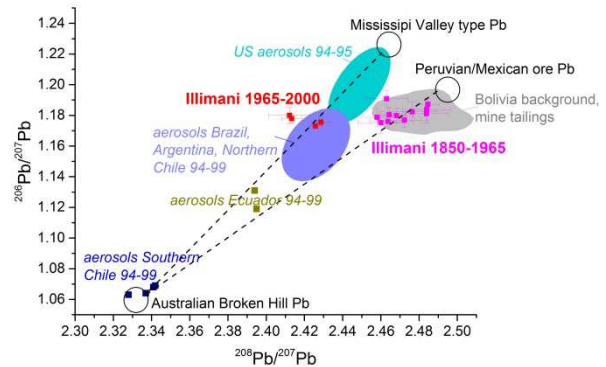
Fig. 3: Three-isotope plot of the Illimani Pb record for the period AD 1850-2000, aerosols from South America and the USA in the period AD 1994-99 [5], background soils and dust in Bolivia and Porco and Potosí mine tailings [3], Australian Broken Hill Pb used in European gasoline, Mississippi Valley type Pb used in USA gasoline, Peruvian/Mexican ore Pb [5].

_____

[1] A. Eichler et al., ES&T, **46**, 4323 (2012).
[2] G. Gramlich et al., Ann. Rep. Lab. of Radio- & Environ. Chem., Uni Bern & PSI (2013), p. 27.
[3] J.R. Miller et al., Sci. Tot. Environ., **384**, 355 (2007).
[4] C. Barbante et al., Int. J. Environ. Anal. **68**, 457 (1997).
[5] A. Bollhöfer et al., Geochim. Cosmochim. Acta **64**, 3251 (2000).

EFFECT OF MELTING ON THE DISTRIBUTION OF iPCBs IN GLACIERS

P.A. Pavlova (Univ. Bern & PSI), P. Schmid (Empa), M. Schwikowski (PSI & Univ. Bern)

PCBs are hydrophobic anthropogenic chemicals, which were introduced in the 20th century, and because of their volatility and persistence are still circulating in the environment. In glacial systems the inventory and localization of contaminants depends on the atmospheric input, the accumulation and ablation of the ice (mass balance), but also on transport processes within the glacier ice. Partitioning of the substances between the different phases ice, pore space and deposited aerosol particles occurs according to their physicochemical properties.

We analysed concentrations of six indicator PCBs (iPCBs) in three Alpine ice cores, which are affected to different extend by melting (Fig. 1). First, an ice core, from 3900 m.a.s.l. at the cold Fiescherhorn glacier, where even in summer almost no melting occurs, is used as an inventory of the atmospheric input into Alpine glaciers. Being particularly interested in the effect of surface meltwater percolating through the pore space and the related leaching of chemicals, we determined iPCBs in two additional ice cores from glaciers subject to surface melting. Grenzgletscher is a cold glacier, located in the Monte Rosa Massif, where an ice core was collected at 4200 a.s.l. The signal of the water soluble species in this ice core is well preserved apart from a 10 mweq segment covering 1985-89, affected by a horizontal meltwater flow from a closely located crevasse [1]. The third ice core was obtained from Silvretta glacier, a temperate glacier with surface melting occurring regularly every year.

The concentration profiles of the three ice cores follow the emission time trends of iPCBs, peaking in 1970s [2] and decreasing towards the surface. Whereas the low contaminant loads in 1960s are explained with low atmospheric input [3], the decreased levels of PCBs in the 1980s in the Grenzgletscher and Silvretta ice cores result of redistribution of substances due to melting. In all three ice cores the dissolved fraction dominates. However, in both Grenzgletscher and Silvretta we observed relatively high particulate loads.

Total loads per cm^2 for Silvretta, Fiescherhorn and Grenzgletscher were calculated by summing-up the deposition fluxes with depth. Since the three glaciers are located in the Alps, where the sources are similar [4], we assume a comparable input of pollutants to the three glaciers. We therefore attribute significant differences in the calculated load to post-depositional melting and release of contaminants.

Ice core	average dissolved	average particulate	total burden
	(ng/L)	(ng/L)	µg/cm^2
Silvretta	0.8	0.2	5
Grenzgletscher	1.1	0.3	19
Fiescherhorn	1.9	0.2	26

Tab. 1: Total load of iPCBs in the three ice cores. Time period covered: Silvretta 1940-2010, Grenzgletscher 1942-1993, Fiescherhorn 1940-2002.

In all three studied glaciers the total loads of iPCBs are in the range of µg/cm^2 (Table 1). Fiescherhorn, considered to preserve the entire inventory, has a load of 26 µg/cm^2. Grenzgletscher, although located closer to additional sources in the Po plain, is characterized with a load of 19 µg/cm^2, which corresponds to the load in Fiescherhorn for the same period (1941-1993 - 20 µg/cm^2). Remarkably, the contaminant load of Silvretta glacier is a factor of 5 lower than the other two (5 µg/cm^2), supporting that melting results in partial loss of organic pollutants from temperate glaciers in the Alps. The extent of these processes depends on the chemical properties and needs to be studied further in detail.

[1] A. Eichler et al., 2001, J. Glaciol., **46** (2000).
[2] K. Breivik et al., Sci. Tot. Env., **377** (2007).
[3] P.A. Pavlova et al., ES&T., **48** (2014).
[4] I. Offenthaler et al., Env. Pol., **157** (2009).
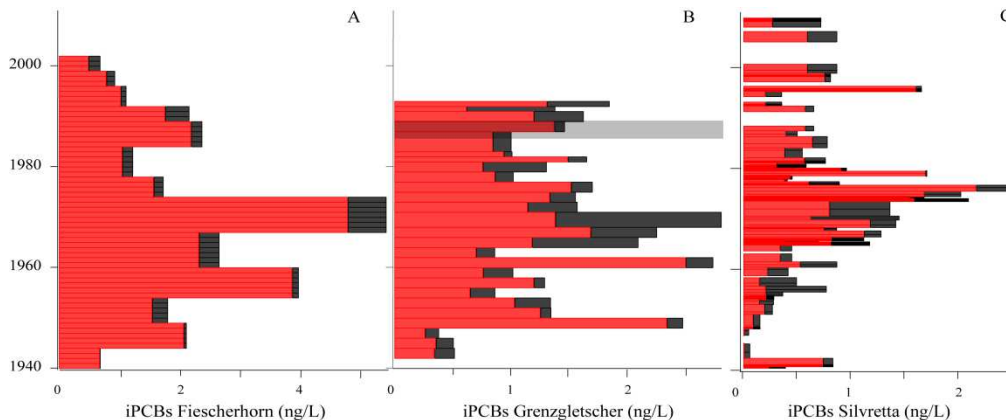
Fig. 1: iPCB records of three Alpine ice cores (red bars– dissolved fraction; black bars – particulate fraction).

MODELLING PCB INCORPORATION INTO A TEMPERATE ALPINE GLACIER

C. Steinlin, C. Bogdal (ETHZ), P.A. Pavlova (PSI, Empa & Univ. Bern), M. Schwikowski (PSI & Univ. Bern),
M. Lüthi (Univ. Zürich), M. Scheringer (ETHZ), P. Schmid (Empa), K. Hungerbühler (ETHZ)

Polychlorinated Biphenyls (PCBs) are industrial chemicals widely used during the 20th century, phased out in the 1970s-80s, and banned worldwide by the Stockholm Convention on persistent organic pollutants (POPs) in 2004 [1]. Decades after their ban, PCBs are still cycling in the environment and can be transported to remote regions. Due to high precipitation rates and cold temperatures, PCBs are deposited to Alpine glaciers, from where these substances are released to sensitive Alpine ecosystems.

We study deposition and incorporation of PCBs into the temperate Alpine Silvretta glacier using a multi-compartment chemical fate model (Fig. 1). The model describes the vertical transport of PCBs in snow and ice of Silvretta glacier. The model includes an air compartment and a set of glacier compartments, consisting of ice, pore air, particles and liquid water. The setup of the glacier compartments is a function of the glacier mass balance, determined by a reanalysis of mass balance measurements between 1900 and 2000 [2]. In the model, we include partitioning of PCBs in the atmosphere and in the glacier, wet and dry gaseous and particle deposition, revolatilization, molecular diffusion, wind pumping, degradation, as well as meltwater and particle percolation and runoff.
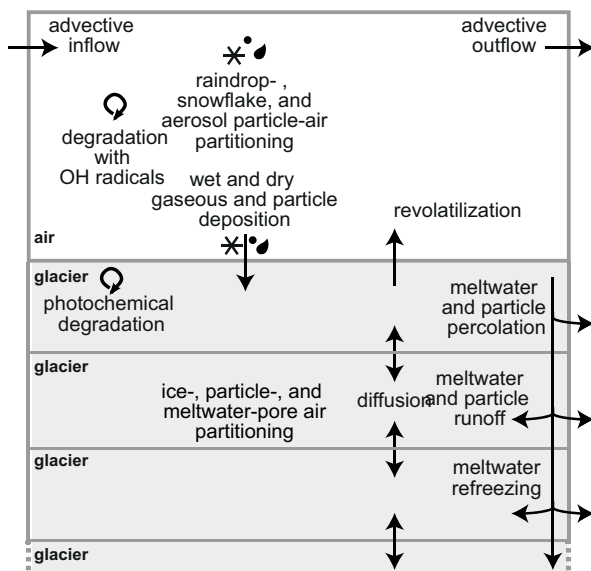
Fig. 1: Model setup including the air compartment, the glacier compartments, and the processes included in the model.

The modelled and measured [3] concentration of PCBs peaks in 30 m depth, corresponding to the 1970s, when PCB emissions were highest (Fig. 2) [4]. This is consistent with our previous results of concentration profiles measured and modelled in a cold glac-

ier [5, 6]. Besides this peak, the PCB concentration profile also contains peaks in periods when PCB emissions were low (e.g. 10 m and 60 m). Due to our model, these peaks can be explained by periods of low ice accumulation and strong melt, leading to an enrichment of particles, and water-insoluble substances, such as PCBs. This is the first study modelling PCB incorporation into a temperate Alpine glacier, which is only possible thanks to the combination of chemical fate modelling, glaciology, and ice core analytics.
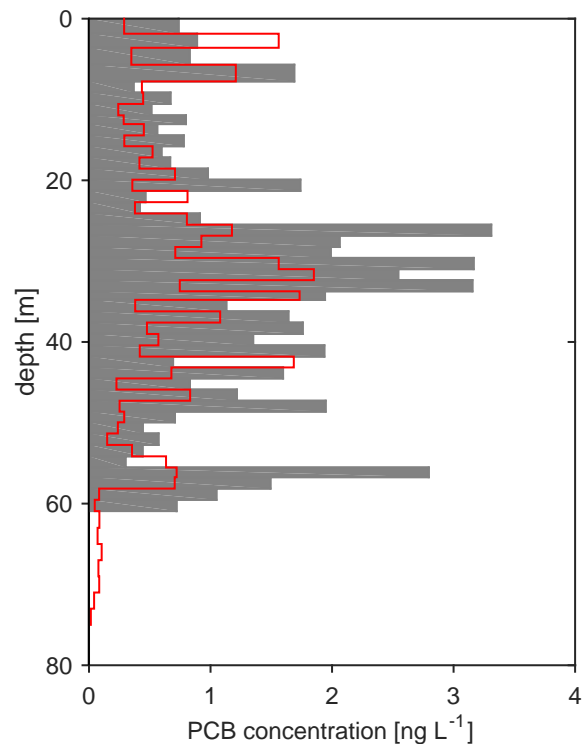
Fig. 2: Modelled (red line) and measured (grey bars, [3]) PCB concentrations in the ice core. Sum of PCB congeners 28, 52, 101, 138, 153, and 180.

---

[1] http://chm.pops.int (2004).
[2] M. Huss and A. Bauder, Ann. Glaciol., **50** (2009).
[3] P.A. Pavlova, PhD Thesis, Univ. Bern (2014).
[4] K. Breivik et al., Sci. Total Environ., **377** (2007).
[5] P.A. Pavlova et al., Environ. Sci. Technol., **48** (2014).
[6] C. Steinlin et al., Environ. Sci. Technol., **48** (2014).

SHALLOW FIRN CORE DRILLING AT THE QUELCCAYA ICE CAP

T.M. Jenk (PSI), J. Schindler (PSI & Univ. Bern), R. Schild (PSI), D. Hardy (Univ. Massachusetts),
M. Vuille (Univ. Albany), F. Vicencio (Vicencio Expeditions), M. Schwikowski (PSI & Univ. Bern)

The Quelccaya Ice Cap is the largest tropical ice cap on Earth. Although reduced by 30% over the last 35 years, the glacier covered area is still around 39 km^2 today [1, 2]. Located in the Cordillera Vilcanota between the high Andean Altiplano extending to the west and the Amazon Basin to the east it is situated in a climatically sensitive region (Fig. 1). The glacier has been studied for more than 40 years and ice cores were drilled to bedrock in 1983 and 2003 [3, 4]. Since 2003, an automated weather station (AWS) is operated on the summit by D. Hardy, running in parallel with a snow sampling program to investigate depositional and post-depositional effects on the stable isotope composition of snow accumulation (e.g. mass redistribution).

Snowfall at this site is highly associated with the South American summer monsoon (SASM) [5] which is of great socioeconomic relevance to sub-tropical South America. Increased understanding of past SASM variations and the response to natural and anthropogenic disturbances is the focus of an ongoing NSF project (PI M. Vuille). Based on highly resolved ice-core proxy data combined with long-term climatologic and glaciological onsite monitoring/calibration programs, it aims at a comprehensive climatological history of the SASM for the last 1000 years. In this context our goal was to extend the 2003 ice core record to the present to obtain overlapping time periods with the dataset from the AWS and related instrumental/remote sensing data. This would allow a detailed investigation on how climatic signals are archived in the Quelccaya ice leading to most reliable paleo reconstructions and interpretation. Furthermore the ice core should allow to accurately determining the currently not well defined accumulation rates for this period.

From 7 to 24 October 2014 this drilling was part of D. Hardy's annual field campaign conducted for AWS maintenance and the snow sampling program. Unexpectedly, the major challenge of the entire expedition turned out to be the import of our equipment. Evolving and highly unpredictable delays related to bureaucracy required permanent reconsideration of the campaign time schedule. With our equipment still waiting in Lima for its release from customs, the expedition team went ahead to reach final camp at the margin of the ice cap (5200 m a.s.l) for acclimatization and the other duties. Thanks to this and the great effort of everyone involved, we were eventually able to transport the equipment from Lima to the Quelccaya summit within

24 hours. The next day, although weather was sunny and surface temperatures close to 0°C, drilling went smooth even under these usually difficult circumstances (Fig. 2). We were able to establish a new depth record for our lightweight drill ("backpack drill" [6]) recovering 21 m of good quality core at 13.93°S, 70.82°W, 5660 m a.s.l.. Obviously, snow and firn conditions on Quelccaya were favourable for our set-up. Firn temperatures were close to the melting point, which significantly reduced the danger that the drill got stuck by freezing to the borehole walls. Yet the temperatures seemed to be never high enough to create percolating meltwater with the potential of water table formation within the firn generally making further penetration impossible. Drilling was stopped soon after solid ice was reached (around 20 m) and core breaking by manual pull started to become almost impossible with a high risk of losing the drill. Snowpit samples with 7 cm resolution were collected for the upper 1.5 m where core quality was lowest.

Fig. 2: Drilling at Quelccaya ice cap.

Transported frozen to our lab, the firn core and snow pit samples will now be analysed for stratigraphic features such as ice and dust layers, density, the stable isotopes of water (δ^{18}O, δD, d-excesss) and concentrations of chemical impurities such as major ions and black carbon. Results will soon show if we succeeded to reach back to the 2003 layer.

[1] M.N. Hanshaw and B. Bookhagen, The Cryosphere, **8**, (2014).
[2] T. Albert et al., GLIMPS, Chapter 26, (2014).
[3] L.G. Thompson et al., Science, **229**, (1985).
[4] L.G. Thompson et al., Science, **340**, (2013).
[5] M. Vuille et al., Clim. Past, **8**, (2012).
[6] P. Ginot et al., Mem. Natl. Inst. Polar Res., Special Issue 56, (2002).

Fig. 1: Panoramic view of the Quelccaya ice cap from the west (Photo by J. Schindler).

THE MERCEDARIO ICE CORE – FINAL DATING POINTS TO THE PRESENCE OF A DOMINANT ENSO SIGNAL

T.M. Jenk, A. Ciric, L. Tobler, H.W. Gäggeler (PSI), U. Morgenstern (GNS), M.P. Lüthi (Univ. Zürich),
G. Casassa (Geoestudios & Univ. Magallanes), J. Schmitt (KUP), M. Schwikowski (PSI & Univ. Bern)

In 2005 a 104 m long ice core was drilled at La Ollada glacier on Cerro Mercedario (31°58'S, 70°07'W, 6100 m asl.) [1]. The drill site in the Central Argentinean Andes was chosen in view of its high potential to obtain a good El Niño-Southern Oscillation (ENSO) proxy record, given the regionally observed strong influence of this climatic phenomena. For any paleoclimate reconstruction a reliable dating of the archive is fundamental. For the Mercedario ice core this turned out to be a major challenge. In a first study, annual layer counting (ALC) based on $\delta^{18}O$ and NH_4^+ signals resulted in significantly different accumulation rates and ages than independent nuclear dating with ^{210}Pb [1]. Yet some analytical artefacts in the ^{210}Pb data could not be excluded. Because of high detection limits in the applied method, first results of tritium measurements to identify the horizon from nuclear weapon tests reflected in a Southern Hemisphere (SH) maximum for the year 1965 were also not conclusive.

In a first step we investigated the potential analytical artefact in the ^{210}Pb results. The depth interval for which samples with suspicious high activities were measured was resampled. Our new results show the expected low background levels. We therefore assume the earlier measurements to be biased, probably due to procedural flaws related to a simultaneous change in the used standard. The new results allow now to convincingly apply an age model to the ^{210}Pb data, resulting in an accumulation rate of 27 ± 5 cm w.eq. yr^{-1}. This value is consistent with newly available tritium data from measurements by electrolytic enrichment and liquid scintillation counting, where the dominant 1965 bomb peaks appears at a depth of 10.54 m w.eq.. Clearly, these results are incompatible with the earlier reported ALC-based value of 91 cm w.eq. yr^{-1}. Thus, the counting based on $\delta^{18}O$ and NH_4^+ had to be questioned. We now assumed the signal in $\delta^{18}O$ to be unrelated to seasonality and ignored it for ALC. Instead, we solely relied on the signals of chemical impurities (i.e. Na^+, NH_4^+, K^+, Mg^{2+}, Ca^{2+}, F^-, MSA, Cl^-, SO_4^{2-}, NO_3^-). Most of them show small, high frequency wiggles superimposed by peaks with a lower frequency similar to the one in $\delta^{18}O$. We interpreted the high frequencies as an annual signal superimposed by a regular, strong and less frequent climatic signal such as the ENSO (Fig. 1). Accordingly the new ALC-based dating results in a much lower accumulation of 27 ± 3 cm w.eq. yr^{-1}. As a supplementary dating tool, four samples were analysed for trace gases enclosed in air bubbles in the ice (CH_4, N_2O and CFCs). From a Freon-13 signal detected in the top most sample, not expected for a sample of atmospheric origin, the bubble close-off depth was assigned to a density of 0.83 ± 0.01 g cm^{-3} in agreement with the value of 0.82 g cm^{-3} calculated following [2]. By comparing the measured mixing ratios with past atmospheric SH values the age of gas was determined. Results were identical for the

different gases which excludes a potentially occurring bias from analytical procedures or in-situ production. The results are consistent with the new but not with the old ALC ages. For a site characterised by high wind speeds and thus highly ventilated firn a relatively young gas age at close-off depth is expected and was estimated with 10 ± 5 years. With a finally derived gas-ice age difference of 99 ± 15 years, an excellent agreement is obtained with the other dating methods. As layers get thinner with depth, ALC uncertainty increases. However, a detectable seasonal signal is retained throughout the core and a counted age of 350 ± 40 years was obtained for the drilled depth of 104 m. This agrees with recalibrated ^{14}C-cal ages previously reported by [3] (here using the appropriate SH calibration curve instead) but is slightly younger than ice flow model based estimates using the defined accumulation rate of 27 ± 3 cm w.eq. yr^{-1} and a radar derived glacier thickness of 145 ± 15 m at the drill site. In conclusion, a reliable chronology with good agreement between different dating methods was achieved after considering a dominant signal with a frequency similar to the ENSO of 3-5 years (Fig. 2).
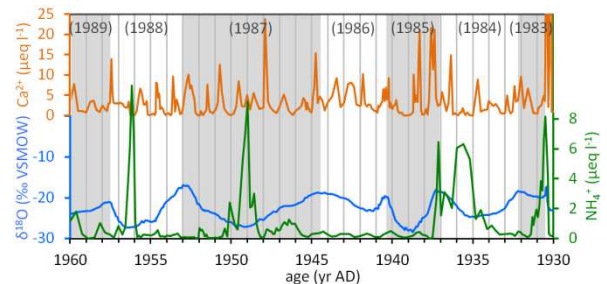
Fig. 1: $\delta^{18}O$, Ca^{2+} and NH_4^+ signals for the 1930-1960 time interval defined by the new ALC approach together with ages (in brackets) and annual layers (grey and white bands) defined by the previous dating.
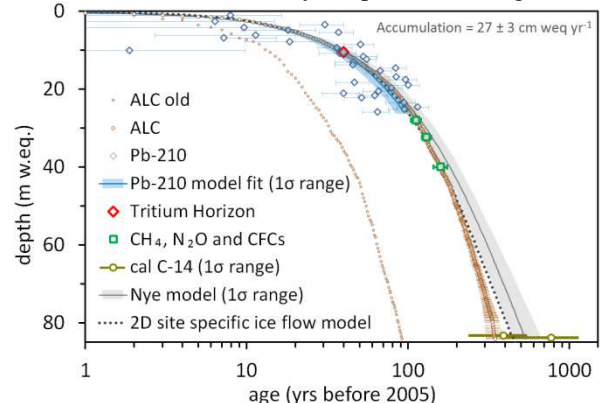
Fig. 2: Depth-age relationship. Values with 1σ errors and sum of uncertain layers divided by two for ALC.

[1] A. Ciric, PhD Thesis, Univ. Bern (2009).
[2] P. Martinerie et al., JGR-Atmos, **99**(D5), (1994).
[3] M. Sigl et al., J. Glaciol., **55**, 194, (2009).

^{14}C AND CONCENTRATION ANALYSES OF DISSOLVED ORGANIC CARBON IN GLACIER ICE - SETTING UP THE EXTRACTION SYSTEM

J. Schindler (PSI & Univ. Bern), D. Piguet, M. Birrer, T.M. Jenk (PSI),
S. Szidat (Univ. Bern), M. Schwikowski (PSI & Univ. Bern)

Glaciers in mid- and low latitudes are valuable archives for paleoclimatology, offering a continuous record of recent local climatic conditions in regions where the majority of mankind lived and lives. For meaningful interpretation of such archives, their accurate dating is essential. Among different complementing approaches, radiocarbon dating is a powerful method due to the continuous record and suitable age range of ^{14}C. Our group developed and ever since successfully applies radiocarbon dating of the particulate fraction of organic carbon (POC) found in glacier ice [1]. The dissolved organic carbon fraction (DOC) promises even better suitability for dating due to factor 5 to 10 higher concentrations compared to POC [2] and a reduced reservoir effect. However, a straightforward analysis is hampered by the need of contamination-free sample processing with isotopic fidelity in the ppb concentration range.

To meet these requirements, we develop an extraction system for ultraclean analyses of DOC in glacier ice. For concentration and ^{14}C measurements, DOC contained in the frozen ice samples needs to be extracted as CO_2. In brief, after cutting and cleaning an ice sample in the cold room, it is melted and further cleaned under helium inert gas conditions in a melting vessel. To separate POC and inorganic carbon, the liquid sample is filtered, acidified and degassed with helium. The remaining DOC in the solution is oxidised by UV radiation in a quartz glass photo-reactor. Evolving CO_2 is degassed and transported through cryogenic traps for cleaning and separation from the carrier gas. In a vacuum system, the CO_2 is further cleaned, quantified and sampled to glass vials for ^{14}C analyses via the gas inlet system of the MICADAS AMS [3].

We constructed and set up the complete extraction system by now. After first optimisation and adjustment, we began to characterise the individual components. Apart from the radiocarbon age, the DOC concentration itself is a valuable proxy, which can be obtained by determination of the ice mass and the amount of extracted CO_2. The latter is measured by a cell with known volume equipped with a manometer ('manometry cell'). To accurately determine the cell volume, we constructed a calibration tube connected to the vacuum line and transferred the calibration by pressure reading of the same amount of CO_2 in different volumes. The cell volume is 3.57 ± 0.08 ml, which in the current setup allows the measurement of less than 1 μg to up to 700 μg with an uncertainty better than 3 %, fitting the expected range of sample concentrations. While the cleaning and transport procedures of the CO_2 in the vacuum line show very good recoveries and high reproducibility, it is subject of current work to optimise the separation of the CO_2 from the helium gas stream in the cryogenic trap and develop a reliable operation protocol.

The glass part of the setup is designed for handling of the frozen and liquid sample. To ensure a very low carbon background, no carbon containing materials are used for the sealing of the individual glass components. However, this sets high demands on the quality of the glass fittings, which were revised multiple times to ensure leak tight and user-friendly operation.

For the UV photo-oxidation step, we use two 250 W medium-pressure Hg-lamps with a broad spectrum down to the UVC range. Despite the need to cool the lamps, they also pose hazards to the operator - directly by radiation emission and indirectly by ozone production. For radiation shielding, ozone venting and air cooling, we constructed a movable housing with folded path air inlets, electrical connections, sample stirrer and a strong ventilator to a fume hood. A cloth around the glass reactor head provides further radiation shielding. As validated by radiation and temperature measurements, this setup provides good radiation protection for the operator as well as sufficient cooling of the lamps and the reactor.
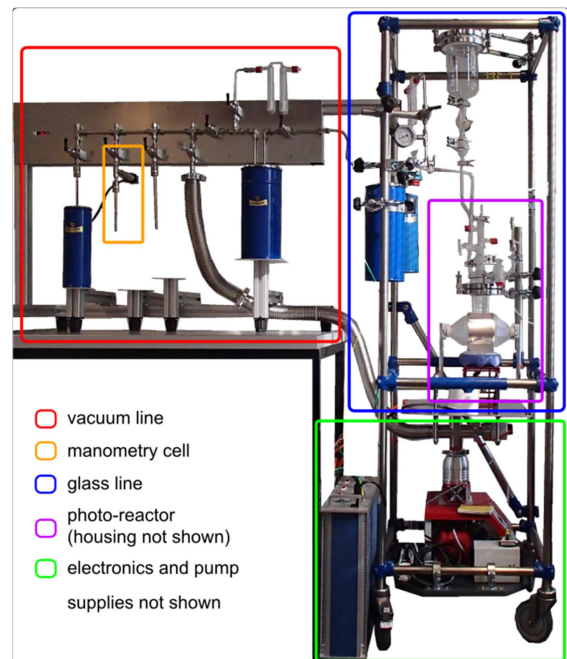
Fig. 1: The extraction system.

Next steps include characterisation of the filtration, acidification and degassing procedures before first oxidation experiments will be started using organic standard substances.

[1]   A. Zapf et al., Radiocarbon, **55** (2013).
[2]   M. Legrand et al., Climate of the Past, **9** (2013).
[3]   S. Szidat et al., Radiocarbon, **56** (2014).

HISTORIC RECORDS OF ORGANIC AEROSOLS FROM A HIGH-ALPINE GLACIER: IMPLICATIONS OF BIOMASS BURNING AND ANTHROPOGENIC EMISSIONS

C. Müller-Tautges (Univ. Mainz), A. Eichler (PSI), M. Schwikowski (PSI & Univ. Bern), G.B. Pezzatti, M. Conedera (WSL), T. Hoffmann (Univ. Mainz)

In contrast to the well-established analysis of inorganic species in ice cores, organic compounds have been analysed to a much smaller extent [1]. These compounds, however, play an important role as constituents of secondary organic aerosol (SOA), which is a major part of atmospheric aerosol.

Ice core records of alpha-dicarbonyls, carboxylic acids, and major ions (sulphate, oxalate, formate, calcium) were determined with annual resolution in an ice core from Grenzgletscher in the southern Swiss Alps, covering the time period 1942-1993. Alpha-dicarbonyl measurements were carried out using a method by Müller-Tautges et al. [2]. Carboxylic acids were analyzed using a new protocol employing solid phase extraction with strong anion exchange followed by ultra-high performance liquid chromatography coupled to high resolution mass spectrometry [3] and major ions were measured using ion chromatography.

To investigate the main sources of the organic trace species, a principal component analysis (PCA) with Varimax rotation was performed using the obtained records (based on 3-year averages, Tab. 1).

Tab. 1: Rotated PCA matrix. PC1: Biomass burning, PC2: Anthropogenic emissions, PC3 Transport with mineral dust, PC4: mixed influence

Variable	PC1	PC2	PC3	PC4
P-Hydoxyb. acid (PHB)	**0.92**			
Pinic acid (PIN)	**0.85**			
Pimelic acid (C7)	**0.81**	0.55		
Suberic acid (C8)	**0.80**			
Glyoxal (G)	**0.73**	0.44		
4-Methylpht.(MPH)	**0.70**	0.43		
Fires South. Switz.	**0.86**			
Methylglyoxal(MG)		**0.84**		
Phtalic acid (P)		**0.77**		
Adipic acid (C6)		**0.68**		
Sebacic acid (C10)		**0.80**		
Dodecan. Ac. (C12)		**0.63**	-0.41	
Oxalate (Ox)			**0.92**	
Formate (Fo)			**0.90**	
Calcium (CAL)			**0.56**	
Azelaic acid (C9)				**0.87**
Vanillic acid (VA)	0.44		-0.56	**0.63**
Variance expl. (%)	35.7	22.1	14.4	10.1

The PC1 record is in good agreement with the burned area from forest fires in southern Switzerland (Fig. 1, upper graph). The main part of the burned species is hardwood forest, followed by grassland [4]. PHB shows the highest correlation of all species with the FSS (r^2=0.75), thus being the best organic fire marker in the study area, which is in agreement with other studies [5]. VA, previously used as typical fire marker [5] does not have a high loading in the PC1 and is only weakly correlated with the FSS (r^2=0.27). Major sources of VA include fires of conifers, which are

minor in Southern Switzerland [4].

Concentration trends of organic compounds having a high loading in PC2 represent changes in anthropogenic emissions of non-methane volatile organic compound (NM-VOC) in Switzerland, France, and Italy (Fig. 1, middle graph).

High loadings of Ox, Fo, and CAL within PC3 and similar records indicate a strong uptake of the small acids by alkaline, calcareous aerosol and a common transport to the glacier (Tab. 1, Fig. 1 lower graph).
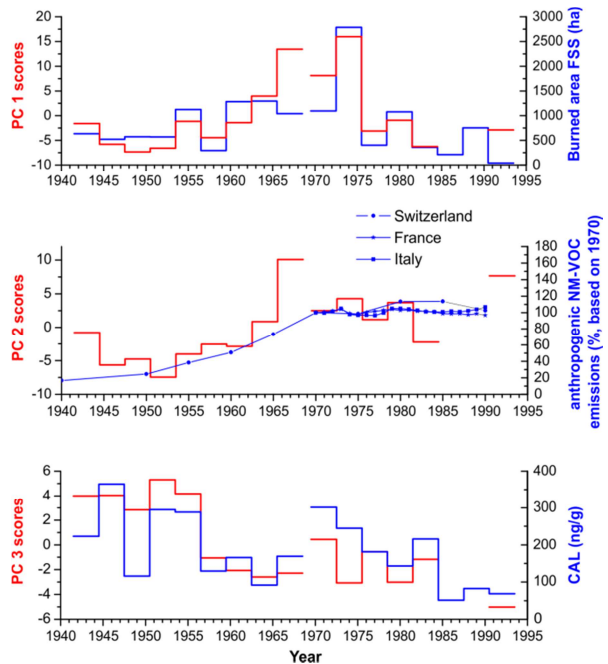
Fig. 1: Scores of PC1-3, burned area in southern Switzerland (FSS) [4], anthropogenic emissions of NM-VOC in Switzerland, France, and Italy [6,7], as well as the ice core record of calcium (CAL).

Thus, biomass burning was found to be the main source influencing the composition of organic matter in the ice core, followed by anthropogenic emissions of NM-VOC, and transport of mineral dust.

[1] M. Legrand et al., Clim. Past, **9**, 2195 (2013).

[2] C. Müller-Tautges et al., Anal. Bioanal. Chem., **406**, 2525 (2014).

[3] C. Müller-Tautges, PhD Thesis, Univ. Mainz (2014).

[4] M. Conedera, G. B. Pezzatti, pers. communication.

[5] K. Kawamura et al., Geochimica et Cosmochimica Acta, **99**, 317 (2012).

[6] Schriftenreihe Umwelt Nr. 256, Bundesamt für Umwelt, Wald und Landschaft (BUWAL), Bern 1995.

[7] EDGAR database (http://edgar.jrc.ec.europa.eu, accessed 04-28-2014).

DETERMINATION OF ACCUMULATION RATES FROM A SHALLOW FIRN CORE OF THE WEST ANTARCTIC ICE SHEET

J. Fenwick (Univ. Bern), A. Eichler, S. Brütsch (PSI), A. Rivera (CECS), M. Schwikowski (Univ. Bern & PSI)

The West Antarctic Ice Sheet (WAIS) is theoretically unstable and many of its glaciers have retreated in the past two decades [1]. Although significant advances have been made in understanding and modelling climate and glacial processes in the region, much remains unknown. The triple ice divide between Pine Island Glacier, Institute Ice Stream and Rutford Ice Stream (PIR Divide) on the West Antarctic Ice Sheet, shown in Figure 1, is of particular interest to glaciologists because a substantial volume of west Antarctic ice drains via these three glaciers [2, 3, 4]. At present, little is known of the accumulation rate in the region, and a better understanding of this may improve knowledge of ice flow and of WAIS stability, more broadly.
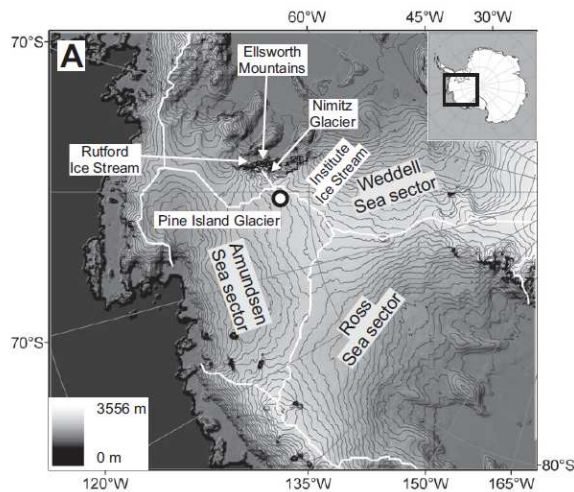
Fig. 1: Ice surface elevation map of the WAIS with sectors and glaciers of interest labelled, including the Pine Island Glacier, Institute Ice Stream and Rutford Ice Stream. The black circle indicates the approximate location of the PIR divide, the site for this study. Based on map from [5].

In January 2014, a 7 metre firn core was drilled at the PIR Divide by a team from the Centro de Estudios Cientificos, Chile, and sent to the Paul Scherrer Institute for analysis. The core, which suffered some degree of melt during transportation, was analysed to calculate the average annual snow accumulation rate. This required annual layer counting using multiple seasonally-varying glaciochemical parameters. $\delta^{18}O$ and δD were measured using Cavity Ringdown Spectroscopy and appeared to exhibit seasonal variability. Ion concentrations were measured with Ion Chromatography and likewise showed seasonality. Based on comparison with the summer-peaking $\delta^{18}O$ record, the major ions could be grouped into winter-peaking species (sodium (Na^+), chloride (Cl^-) and potassium (K^+)

and summer-peaking species (methanesulfonate ($CH_3SO_3^-$), sulphate (SO_4^{2-}) and nitrate (NO_3^-)). The opposing seasonality can primarily be attributed to sea salt aerosols peaking in winter due to sea ice expansion and bioactivity peaking in summer due to sea ice melt. The summer NO_3^- maximum results from polar stratospheric cloud sedimentation and summer post-depositional processes.

Despite the melt damage to the core, it was possible to determine 18 annual layers, shown on the $\delta^{18}O$ data in Figure 2, by counting the aligning peaks in the isotope and ion records. Based on this allocation of years, an average accumulation rate of around 25 cm water equivalent per year (minimum 10.1 cm, maximum 46.7 cm) was calculated.
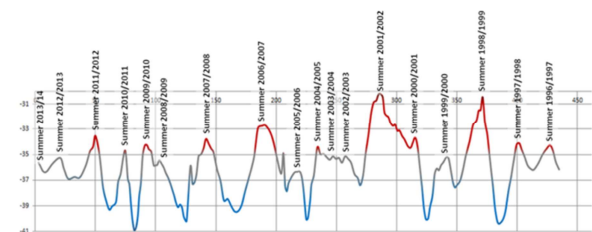
Fig. 2: $\delta^{18}O$ record for the PIR divide with colours accentuating high and low values. Labels show austral summers based on annual layer counting. X-axis is depth in cm water equivalent, Y-axis shows $\delta^{18}O$ in per mil.

Analysis of a radargram from the site, with knowledge of this accumulation rate, indicated that annual reflectance horizons could not be identified without radar data of higher resolution. As a result, the available radargram for the PIR Divide was not deemed suitable for further analysis of accumulation rates.

These results suggest that the PIR Divide is suitable for glaciochemical analysis, with a reasonably high accumulation rate and seasonally varying ions and stable isotopes useful for annual layer counting. The retrieval of additional firn or ice cores, without melt influence, could contribute valuable data regarding the West Antarctic.

[1] E. Rignot et al. Geophys. Res. Letters. **41**, 3502 (2014).
[2] P. Dutrieux et al. Science. **343**, 174 (2014).
[3] R. Goldstein et al. Science. **262, 1525** (1993).
[4] T. Scambos at al. Antarctic Science. **16** (2004).
[5] N. Ross et al. Geology. **39** (2011).

COASTAL ANTARCTIC ICE CORES RECORD REGIONAL CLIMATE CHANGES: EXAMPLES FROM DRONNING MAUD LAND

E. Isaksson (NPI), C.P. Vega (Uppsala Univ.), J. Brown, D. Divine, J. Kohler, K. Matsuoka (NPI),
E. Schlosser (Univ. Innsbruck), T. Martma (Tallin Univ. Technology), R. Mulvaney (BAS),
A. Eichler (PSI), M. Schwikowski (PSI & Univ. Bern)

Antarctic ice cores are important to study past climate and environmental changes in order to predict future changes in the Earth´s climate system and biogeochemical cycles. During the past decades, Norwegian scientists, in collaboration with international initiatives, have retrieved and analysed shallow firn/ice cores and snow pits from coastal Dronning Maud Land (DML) as part of projects focusing on the spatial variability of surface mass balance (SMB [1]). In this study, we use ionic results from a 100 m long ice core (S100 [2]) drilled during the austral summer 2000/2001 at the Fimbulisen ice shelf, western DML, and one of three recently drilled shallow ice cores retrieved at three ice rises at Fimbulisen (IRB, IRC and IRD). The aim of this study is to use these unique glacio-chemical records as proxies of regional changes in key climate variables such as temperature and sea ice extent (SIE), as well as changes in climate forcing and biogeochemical cycles.

Methanesulfonic acid (MSA) can be used as proxy for marine biogenic productivity [3], and potentially as proxy for Antarctic SIE [4]. When comparing annual standardized MSA (combined S100 and IRD ice cores) and SIE at different sectors of Antarctica during 1979-2012 (Fig. 1), the correlation between MSA and SIE is only significant at the 95% confidence level at the Weddell Sea (R = 0.29), the Bellingshausen/Amundsen Seas (R = -0.34) and when considering the total SIE anomalies in Antarctica (R = 0.42).
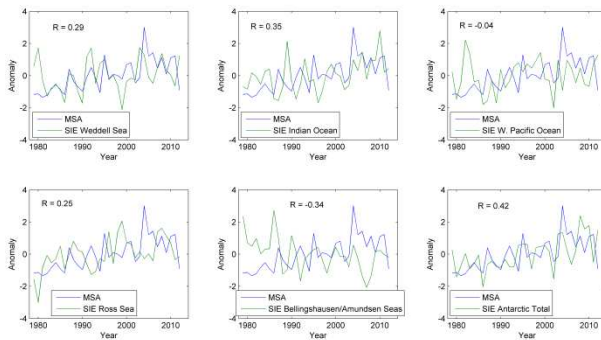
Fig. 1: Annual standardized MSA (combined S100 and IRD) (blue line) and SIE (green line) for the period 1979-2012.

The wavelet coherence method was used to compare the MSA record and El Niño 3.4 SON index and examine the relationship between the series during the period 1950-2012 (Fig. 2). The WTC analysis demonstrates that the records exhibit coherent variations on the scales of approximately 4-6 years during the period 1970-1990. During this period, the warmer SST in the Pacific are anti-correlated with the MSA combined record on the 4-6 year time scales (as indicated by arrows pointed to the left). There is another statistical-ly significant variation between the records at 2 years and less during a short period between 1990 and 2000.
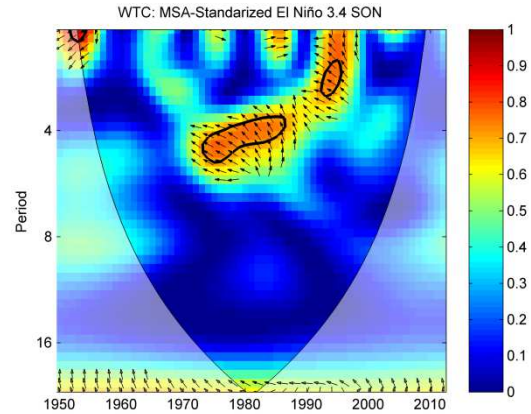
Fig. 2: Wavelet coherence (WTC) between the standardized annual mean of the combined MSA record and the standardized El Niño 3.4 SON index during the period 1950-2012. Thick contours show the areas with correlation statistically significant at the 95% confidence level again red noise. Semi-transparent areas indicate the cone of influence where the time series edge effects become important. The relative phase relationship is shown in arrows, with in-phase pointing right and anti-phase pointing left.

The combined ion record (S100 and IRD ice cores) presented in this study was employed to investigate possible links between the MSA, and SIE at different sectors of Antarctica. The MSA record is representative of changes on the SIE in the Weddell Sea during the period 1979-2012. By using WTC, interesting correlations were observed between MSA and El Niño 3.4 index, however, further and more refined calculations need to be done before drawing robust conclusions on the relationship between such climate index and the ion data from Fimbulisen ice core records.

ACKNOWLEDGEMENT

[1] E. Schlosser et al., J. Geophys. Res. Atmospheres, **119**, 6549 (2014).
[2] M. Kaczmarska et al., Antarctic Science, **18**(2), 271 (2006).
[3] C. Saigne and M. Legrand, Nature, **330**, 240 (1987).
[4] K. A. Welch et al., Geophys. Res. Lett., **20**(6), 443 (1993).

COMPARISON OF TWO ICE CORE RECORDS
FROM LOMONOSOVFONNA, SVALBARD

I.A. Wendl (PSI & Univ. Bern), S. Brütsch, A. Eichler (PSI), E. Isaksson (NPI), T. Martma (Tallin Univ. Technology), M. Schwikowski (PSI & Univ. Bern)

Here, we present a first comprehensive comparison of two ice cores, retrieved from Lomonosovfonna, Svalbard, just 4.6 km apart, to assess to what extent the parameters analysed in the cores agree. This comparison is thought to reveal whether the climate and environmental reconstruction from one ice core is representative of an entire region such as the archipelago of Svalbard. The two cores were collected in 1997 [1] and 2009 [2] (Lomo97 and Lomo09), respectively.

Both cores were dated using a multiple parameter approach. Several major volcanic eruptions were identified in both cores, with the 1783 Laki eruption having the most prominent impact on the SO_4^{2-} records. The 1963 tritium peak was clearly imprinted in both cores, with total activity and depth of the peak in the same range. The largest discrepancy is the age of the deepest core sections, which resulted from the attribution of the SO_4^{2-} peak detected in the deepest core section to two different major volcanic eruptions, the Hekla 1104 or 1158 for the Lomo97 and the Samalas 1257/58 for the Lomo09.

The ion chemistry as well as the concentration trends in the ion records are overall similar (Tab. 1). The two cores are dominated by the sea salt species of Na^+, Cl^-, K^+, and Mg^{2+} that contribute >70% to the ion budget. The anthropogenic influence is observed in both cores, especially in the NO_3^- and SO_4^{2-} records. The correlation between MSA and NO_3^- detected in the Lomo09 core [3] is not seen in the Lomo97.

Tab. 1: Median values [µeq/L] for the ionic species and the annual accumulation rate [m weq/year] in the Lomo97 and Lomo09 ice cores as well as Lomo09 to Lomo97 ratios.

1222-1997	Lomo97	Lomo09	Ratio 09/97
MSA	0.07	0.07	1.0
Cl⁻	6.87	10.18	1.5
NO₃⁻	0.63	0.58	0.9
SO₄²⁻	2.25	2.35	1.0
Na⁺	6.18	8.50	1.4
NH₄⁺	0.90	0.57	0.6
K⁺	0.14	0.23	1.6
Mg²⁺	1.26	1.87	1.5
Ca²⁺	0.94	1.29	1.4
Accummul.	0.36 [4]	0.58	1.6

The NH_4^+ records show large differences especially before 1950. The preindustrial (before 1859) concentrations of NH_4^+ at both sites are close to the detection limits of the analytical methods. In addition, NH_4^+ is prone to contamination during samples preparation and analysis. During our sample preparation steps we minimize NH_4^+ contamination from lab air by melting ice samples in a N_2 atmosphere. We therefore think that the Lomo09 NH_4^+ concentrations are robust.

The concentrations of all sea salt components (Na^+, Cl^-, K^+, Mg^{2+}) are higher by a factor of 1.5 in Lomo09 than in Lomo97, whereas NO_3^-, SO_4^{2-}, and MSA show similar levels (period 1222-1997). Since also the annual accumulation rate is a factor of 1.6 higher at Lomo09 this suggests slightly different humidity source regions or air mass trajectories. The $\delta^{18}O$ records of the two ice cores are similar (Fig. 1), thus the Lomo09 $\delta^{18}O$ record is thought to correlate best with air temperature near Longyearbyen like the Lomo97 $\delta^{18}O$ record. The records of the stratigraphic melt index show great similarities in the common period from 1700 to 1997. The records of the melt index $\ln(Na^+/Mg^{2+})$ are comparable prior to around 1800. Afterwards, the Lomo09 record resembles more that of the Holtedahlfonna ice core drilled in 2005 [3].

This comparison of two ice cores from Lomonosovfonna shows that the climate and environmental reconstruction from one Lomonosovfonna ice core is representative of the glacier, but not necessarily of the entire region of Svalbard.
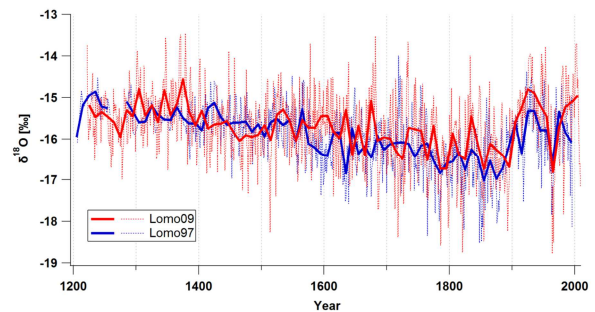
Fig. 1: Records of $\delta^{18}O$ of the Lomo97 (blue; [4]) and the Lomo09 ice core (red). Dashed lines are annual averages; bold lines are 10-year-averages.

[1] E. Isaksson et al., J. Glac. **47** (157) 335 (2001).
[2] I. Wendl, PhD Thesis, University of Bern (2014).
[3] I. Wendl et al., Atmos. Chem. Phys. Discuss. **14**, 24667 (2014).
[4] D. Divine et al., Polar Research **30**, 7379 (2011).

INTEGRATION OF AN AUTOSAMPLER WITH A SINGLE-PARTICLE SOOT PHOTOMETER AND A JET NEBULIZER TO MEASURE BLACK CARBON IN ICE CORES

L. Schmidely (Univ. Bern & PSI), A. Dal Farra (PSI & Univ. Bern), T.M. Jenk, P.A. Pavlova (PSI), M. Schwikowski (PSI & Univ. Bern)

The single-particle soot photometer (SP2) is considered as a state-of the art instrument to analyze black carbon (BC). It uses a laser-induced incandescence principle to determine mass concentration and size distribution of BC independent of the amount of coating of the particles and the mixing state of BC. Particles suspended in air are pumped into the SP2 and are heated by a Nd :YAG-laser to their boiling point (4200 K). The intensity of the thermal radiation they emit is detected by two photomultiplier tubes and the magnitude of this signal is then proportional to the mass of the BC particle [1].

Previous work by I. Wendl and others at PSI focused on implementing a procedure to analyze BC in ice samples combining an SP2 with a nebulizer to convert liquid samples into an aerosol. The APEX-Q jet nebulizer was found to be highly suitable as it requires small sample volumes and has the least size-dependent nebulizing efficiency. The following sample treatment procedure was developed: samples should be quickly melted, sonicated for 25 minutes to break down eventual agglomerates, and stirred during measurements to keep BC concentration homogeneous in the solution. Samples should be measured immediately after melting as BC concentrations tend to decrease over time because of particle settling and adhering to the container's wall. To avoid further losses, refreezing and remelting should be avoided [2].

We aim at improving this setup by adding a CETAC ASX-520 autosampler (AS). Using an AS allows us to automate BC measurements making the procedure better reproducible and less time-consuming. Concretely, we run the AS with a new routine that increments samples based on the count of BC particles instead of the count of the total number of particles. For statistical precision, the threshold to increment sample is set to 10'000 particles [1]. This can take more than one hour in case of very low concentrated samples. Therefore, the routine allows us to define the maximum measurement time corresponding to the time necessary to consume the smallest volume in a series of samples with mean sample consumption around 0.0064 g/s. This is crucial to avoid that the AS aspirates air as this is likely to disturb the following measurement. In case sample volume is very small it is still possible to combine it with the next sample at the expense of time resolution [1].

Furthermore, we set a delay of 2.5 minutes before starting BC particles counting and a five minutes rinsing time between each measurements. These values allow the counting to start with the sample signal and that the baseline concentration is met again between samples.

We monitored the stability of the setup by conducting regular calibrations with standards. The results show a stable SP2 response over time with larger deviations for high concentrations.
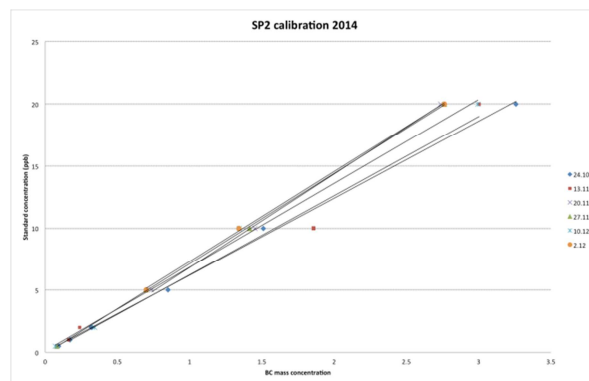
Fig. 1: Calibration curves of the SP2.

In the future, two experiments remain to be done to operate the SP2 with the AS at full capacity.

First, we will address the stability of BC concentration in samples over time. As mentioned before, this has been reported to decrease, [1] and quantifying this effect over the course of a week will allow us to know how many samples can be inserted at the same time in the AS. The experiment will consist in measuring in loop a series of standards, samples and blanks during three days to calculate losses as a function of time. This experiment needs to be repeated three times to ensure the stability of the results.

Secondly, as stirring is not convenient to perform with an AS, an experiment will be conducted to discriminate its contribution to the BC concentration recorded. This will be done by measuring the same set of samples once with stirring and once without.

To conclude, the addition of the AS to the SP2 APEX-Q nebulizer will largely increase the efficiency of BC measurements. We will be able to process more samples by operating the instrument continuously with a routine based specifically on the BC particles counting. Finally, the precision of measurements will also be improved as the same routine will be applied to every sample.

_____

[1] I. Wendl et al., Atmos. Meas. Tech., **7**, 2667 (2014).
[2] I. Wendl, PhD Thesis, University of Bern (2014).

INFLUENCES OF IMPURITIES ON GLACIER ALBEDO

A. Dal Farra, L. Schmidely (Univ. Bern & PSI), T.M. Jenk (PSI), M. Schwikowski (PSI & Univ. Bern)

Glaciers in Switzerland are receding, in agreement with the worldwide trend of glacier retreat. Evidence of this is numerous and has been provided by both modelling studies [1] and remote sensing-based studies [2]. One of the causes of this alarming trend is assumed to be the albedo effect. For snow covered glaciers the albedo is very high and the solar radiation is thus mostly reflected. For glaciers that are snow free during the summer the albedo is considerably lower (see example of Plaine Morte glacier in Fig. 1).

Fig. 1: Comparison of complete snow cover (left) and snow free conditions (right) on Plaine Morte glacier.

The lowering of the albedo is largely attributable to the accumulation on the glacier's surface of cryoconite. Cryoconites are supra-glacial particulate deposits, consisting of granules which contain living microorganisms, decomposing organic matter, mineral dust, and black carbon. The aim of this study is to characterize the cryoconite and define the contribution of each of its components to the absorption of the solar radiation.

Two field campaigns have been successfully carried out on Rhone glacier and on Plaine Morte Glacier in 2014 (Fig. 2). The objective for the work on Rhone glacier (a very accessible glacier) was to test the instrumentation and the methods for sample collection [3]. The glacier considered for this study is Plaine Morte glacier, located between the cantons of Valais and Bern. This glacier had been the subject of both remote sensing studies and hydrological studies [4]. On this glacier fourteen samples were collected and their reflectance was measured in-situ with a Fieldspec 3 (Fig. 3).
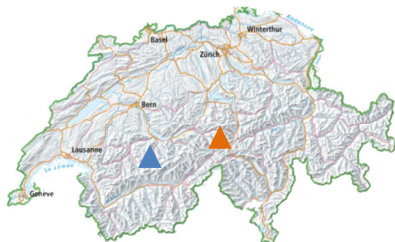
Fig. 2: Location in Switzerland of the two glaciers Plaine Morte (blue), Rhone Glacier (orange).

The analysis of these samples aims at the characterization of the components of the cryoconite and at the determination of their individual contribution to the absorption of the solar radiation.
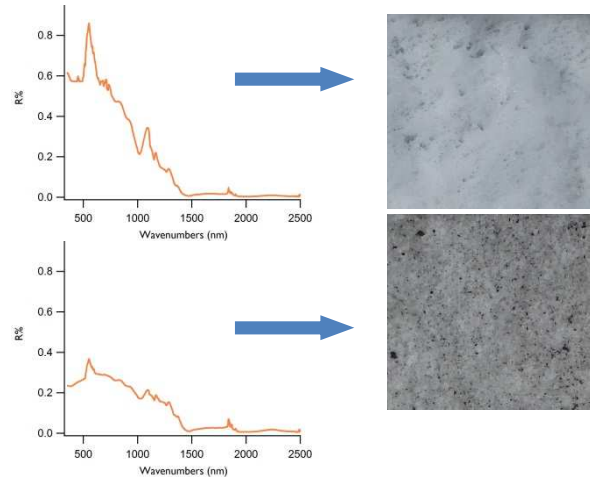
Fig. 3: Fieldspec3 spectra and the corrispective picture of the measured area. The darker more loaded surface shows lower reflectance.

We will employ different methods to identify these components. X-Ray Diffractometry for mineral dust, Single Particle Soot Photometry for black carbon and UV-Vis Spectrometry for organic matter. Their light absorption properties will be studied using reflectance spectra obtained on the glacier and of individual components measured with Scanning Multi-Channel Reflectance Spectroscopy in the visible and near IR range.

This latter instrument takes Hyper Spectral Images, in which a picture is obtained where each pixel corresponds to a reflectance spectrum. The complex data can be made more legible through principal component analysis and be used to identify the different contribution to the total absorption. The cryoconite is deposited on a quartz filter and on this filter the first hyperspectral data is taken. By removing each component and repeating the measurement the contribution of each to the absorption will be defined. This will lead to a decisive step forward in understanding the effect of albedo lowering substances in glaciers.

_____

[1] M. Huss et al., Hydrol. Process., **22**, 19 (2008).

[2] F. Paul and W. Haeberli, Geophys. Res. Lett. **35**, (2008).

[3] http://www.kika.de/checker-tobi/sendungen/sendung78982.html.

[4] D. Finger et al, Hydrol.Earth Syst. Sc., **17**, 8 (2003).

[5] K. Naegli et al., Geophys. Res. Abstr., **16**, (2014).

ICE CORE-DERIVED ANTHROPOGENIC AND BIOGENIC CONTRIBUTIONS TO CARBONACEOUS AEROSOLS IN THE PAST (1650-2002)

F. Cao (PSI & GIG CAS), Y.L. Zhang, S. Szidat (Univ. Bern & PSI),
T.M Jenk (PSI), M. Schwikowski (PSI & Univ. Bern)

Radiocarbon (^{14}C) determination of particulate OC and EC extracted from ice cores provides a powerful tool to reconstruct the historical anthropogenic and biogenic emissions of carbonaceous aerosols. A first long-term record of OC and EC concentrations along with the corresponding fraction of modern (f_M) carbon derived from ^{14}C analysis in an Alpine ice core (Fiescherhorn glacier, 46°33'3.2''N, 08°04'0.4''E; 3900 masl.) was published by Jenk et al. (2006) [1]. However, this ^{14}C-based source apportionment method was not applied to the firn section (upper ~100 m, time period 1940-2002) due to difficulties in decontamination. We developed a decontamination method for ^{14}C analysis in firn [2] and measured mass and ^{14}C content of OC and EC extracted from the firn part of the Fiescherhorn ice core. Together with the previous data [1] this forms a complete record of anthropogenic and biogenic emissions in the past (1650-2002).

Detailed procedures on sample preparation, separation of the two fractions and applied analytical methods (AMS) can be found in [2]. OC and EC were determined and separated by a recently developed thermal-optical method [3]. ^{14}C measurements were carried out with the MIni CArbon DAting System (MICADAS) with a gas ion source [4].

Concentrations of OC, EC are presented in Fig. 1. We combined the results in this study with the previous study [1] to achieve a long historic record. The concentration of OC increased slightly from 1940 to 2002, while the concentration of EC showed a decreasing trend.
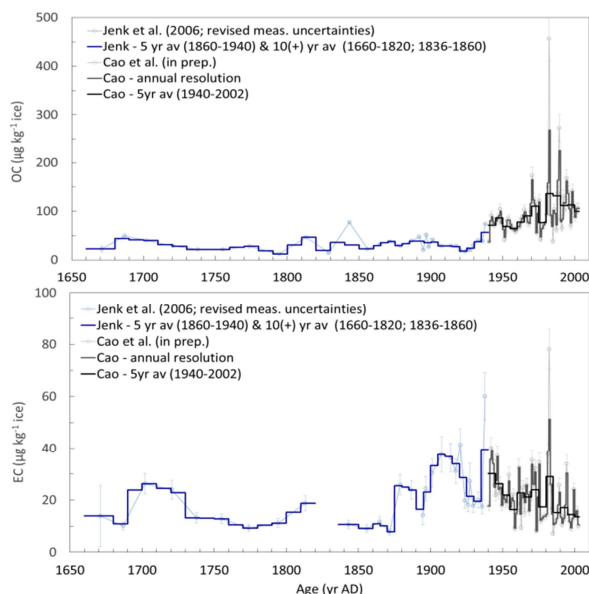
Fig. 1: Temporal changes of concentrations (µg/kg) of OC and EC extracted from firn and ice cores from Fiescherhorn glacier, covering 1650-2002.

The record of OC and EC apportioned to fossil and non-fossil contributions using the ^{14}C content is shown in Fig. 2. In general, fossil contribution to EC was much larger than to OC, indicating significant anthropogenic EC emissions due to the use of fossil fuels (such as coal, later oil and diesel). Non-fossil EC emissions were relatively stable during the last 300 years. The fossil EC emissions increased rapidly since the beginning of the industrial revolution (i.e. 1860s), but started decreasing in the 1940s due to many factors (e.g. mainly environmental regulation). Total OC emissions were quite stable from 1650 to 1940, and then increased until 2002, which is likely due to enhanced photochemical aerosol production and increased petroleum combustion. The variations of fossil OC concentrations were associated with anthropogenic emissions related to different energy consumption and environmental control implementation.
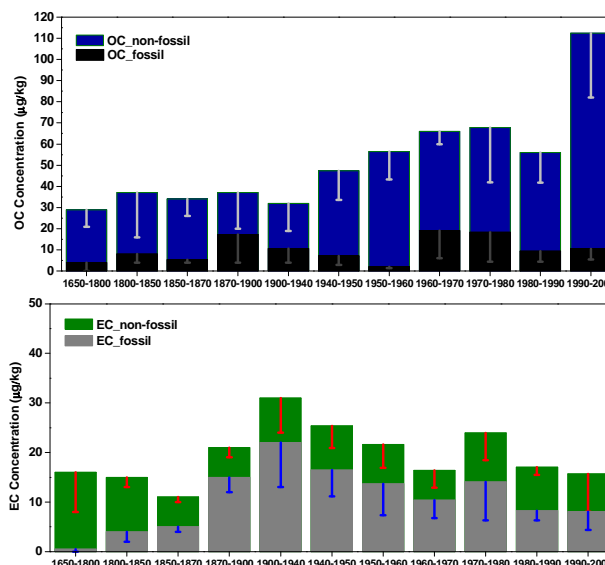
Fig. 2: Fossil and non-fossil contributions to OC and EC extracted from firn and ice cores at Fiescherhorn glacier, covering 1650-2002.

_____

[1] T. M. Jenk et al., Atmos. Chem. Phys., **6**, 5381 (2006).
[2] F. Cao et al., Radiocarbon, **55**, 383 (2014).
[3] Y.L. Zhang et al., Atmos. Chem. Phys., **12**, 10841-10856 (2012).
[4] L. Wacker et al., Nucl. Instrum. Methods B., **294**, 315 (2013).

THE IMPACT OF SAHARAN DUST AND BLACK CARBON ON THE LONG-TERM GLACIER MASS BALANCE

J. Gabbi (ETHZ), M. Huss (ETHZ, Univ. Fribourg), A. Bauder (ETHZ),
M. Schwikowski (PSI & Univ. Bern), F. Cao (PSI & GIG CAS)

Light-absorbing impurities at the glacier surface have a strong impact on the energy balance of snow and glacier covered areas. They augment the absorption of sun light and enhance snow and glacier melt [1]. Light-absorbing particles on alpine glaciers consist primarily of black carbon (BC) and mineral dust, the latter made to a large proportion of Saharan dust [2].

The study aims to determine the long-term effect of anthropogenic and natural impurities in snow and firn on the glacier mass balance. We have chosen Claridenfirn (Glarus Alps) as study site where an extraordinary data set of seasonal mass balance measurements over a 100-year period (1914-2014) is available. These measurements allow an accurate determination of ablation and accumulation rates in the investigation period. The analysis was performed at two locations: one measuring site which is situated in the accumulation area and a second site which migrates from accumulation to predominately ablation conditions in recent years (Fig. 1). In order to simulate the feedback between melt, accumulation and impurities, a glacier mass balance model was coupled to a snow layer model which tracks the position and the thickness of the deposited snow layers and impurities. Atmospheric deposition rates of mineral dust and BC were derived based on two ice/firn cores from Colle Gnifetti (Valais Alps) and Fiescherhorn (Bernese Alps).

According to our model results, high Saharan dust concentrations at the glacier surface occur in years with high atmospheric deposits of Saharan dust and in years with intense melting (e.g. in the 1940s and 2000s). Under conditions of melt, Saharan dust particles are retained at the surface due to inefficient removal by melt water which leads to a rise in surface concentration. In comparison to Saharan dust, BC is less influenced by episodic deposition and shows only in melt-intense periods high concentrations at the surface.

Our study demonstrates that the presences of light-absorbing snow impurities have a strong impact on the glacier mass balance. At the lower site, Saharan dust and BC together lead to a change in cumulative mass balance of 49 m over the period 1914-2014 compared to pure snow (Fig. 1a). BC more strongly

affects glacier melt than Saharan dust and yields a seven times larger change in cumulative mass balance. The effect of light-absorbing impurities depends strongly on the location on the glacier. At the upper site the effect of Saharan dust and BC is less pronounced and is around half of that at the lower site (Fig. 1b). The mainly positive mass balances at the upper site lead to a continuous burial of deposited impurities by winter snow whereas the negative mass balances at the lower site lead to a re-exposure of dust-loaded layers and thus to accelerated melting.

Particularly with regard to the climate change, a potential darkening of the glacier surface due to enhanced melting may play an important role in accelerating the retreat of mountain glaciers.
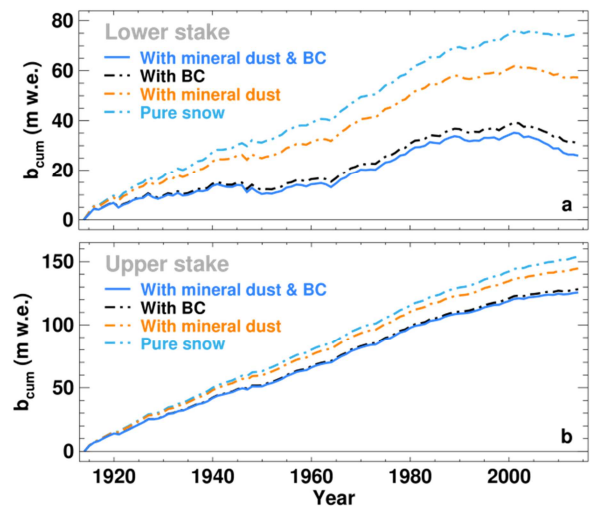
Fig. 1: The cumulative mass balance over 1914-2014 at (a) the upper and (b) the lower measurement sites. The solid blue lines correspond to the cumulative mass balance under real conditions (including Saharan dust and BC) and are consistent with the direct observations on Claridenfirn. The dashed-dotted lines refer to simulations (1) only with BC, (2) only with Saharan dust and (3) with pure snow conditions.

---

[1]   T. Painter et al., Geophys. Res. Lett. **34** (2007).

[2]   D. Wagenbach and K. Geis in "Paleoclimatology and Paleometeorology", Springer, **282** (1989).

THE CONTROVERSIAL AGE OF KILIMANJARO ICE CAP

C. Uglietti, A. Zapf‡ (PSI & Univ. Bern), T.M. Jenk (PSI), S. Szidat, G. Salazar (Univ. Bern),
D. Hardy (Univ. Massachusetts), M. Schwikowski (PSI & Univ. Bern)

The age of the Kilimanjaro's plateau glaciers is still debated. Paleoclimate reconstructions based on six ice cores, extracted from the Kilimanjaro plateau ice fields in 2000, assigned a basal age of 11'700 years [1]. A more recent study claims recurring cycles of waxing and waning with estimated decay time periods of a few hundred years, controlled primarily by atmospheric moisture [2]. An absence of the ice bodies was reconstructed for the period around 850 years ago.

The aim of this project was therefore dating of the Kilimanjaro plateau glacier applying our ^{14}C method [3, 4] in order to resolve the age controversy. This might have wide implications for understanding of the full range of natural climate variability in the tropics.

In 2011 a stratigraphic sequence with a total of 45 horizontal short cores (50 cm length) was extracted from 22 horizons characterized by varying microparticle concentrations from the exposed vertical ice cliffs at the margins of the Kilimanjaro Northern Ice Field (NIF). Additionally, 3 surface samples were taken to investigate a potential age offset (Fig. 1). All samples were shipped frozen to Paul Scherrer Institute, decontaminated in a cold room by removing the outer layer (0.3 mm) and by rinsing the samples with ultra-pure water in a class 100 clean room. The insoluble carbonaceous particles were filtrated onto preheated quartz fibre filters which were combusted by means of a thermo-optical OC/EC analyser (Model4L, Sunset Laboratory Inc, USA), using a well-established protocol (Swiss 4S) for OC/EC separation [5]. Procedural blanks were estimated using artificial ice blocks of frozen ultra-pure water treated as real ice samples and were consistent with previously reported blanks [3, 4]. ^{14}C analyses were conducted using the compact radiocarbon AMS system 'MICADAS' equipped with a gas ion source, directly coupled to the Sunset instrument. Conventional ^{14}C ages were calibrated using OxCal v4.2.4 software with the SHCal13 calibration curve.

The results of ^{14}C calibrated ages for the South and North cliffs of the NIF are shown in Fig. 2 against the depth of the ice cliffs with 0 m corresponding to the surface.

The dates span between modern ages at the surface to 1200 AD at the bottom of the cliff. A linear fit model was run through the data points with confidence interval of 68.2 and 95.4%.
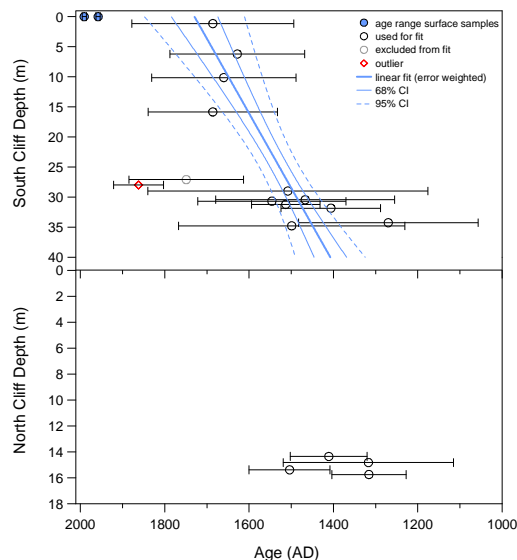
Fig. 2: Upper: Calibrated ages for the NIF south cliff with 1 sigma error bars and linear regression with confidence intervals at 1 and 2sigma. **Lower:** Calibrated ages for the bottom samples of the north cliff of NIF with corresponding 1 sigma error bars.

The dating is in good agreement with previous results from the 2009 campaign and also with ^{14}C ages of ice and soil samples published recently [6] and suggests that there is no horizon older than 800 years even close to bedrock. Therefore our ^{14}C ages support the hypothesis that the ice on Kilimanjaro's plateau has come and gone repeatedly throughout the Holocene [2] and cannot be reconciled with the postulated ice core-based basal age of 11'700 years [1]. It is possible that the cores collected further from the margin of the NIF contained older, relict ice, which is not present at the margins, implying a strong hiatus to the upper part and a non-continuous record. In ongoing work we will try to reduce the uncertainty of the dating points by determining additional ^{14}C ages from the parallel samples.

ACKNOWLEDGEMENT

Fig. 1: Left: South side of the NIF with the sampled cliff section indicated by the red box and a zoom with locations of all the cores sampled and on the top of the cliff the location of the surface samples. **Right**: North side of the NIF with the sampled cliff section.

[1] L.G. Thompson et al., Science, **298**, 589 (2002).
[2] G. Kaser et al., The Holocene (2010).
[3] T.M. Jenk et al., J. Geophys. Res. Atmospheres, **114**, (2009).
[4] M. Sigl et al., J. Glaciology **55**, 985 (2009).
[5] Y.L. Zhang et al., Atmos. Chem. Phys., **12**, 10841 (2012).
[6] A.C. Noell et al., The Holocene (2014).

A NEW THERMAL DRILLING SYSTEM FOR HIGH-ALTITUDE OR TEMPERATE GLACIERS

M. Schwikowski (PSI & Univ. Bern), T.M. Jenk (PSI), D. Stampfli, F. Stampfli (icedrill.ch)

For ice core drilling on high-elevation glaciers, lightweight and modular electromechanical (EM) drills are used to allow for transportation by porters or pack animals. However, application of EM drills is constrained to glaciers with temperatures well below the ice melting point. When drilling into temperate ice, liquid water accumulates in the borehole, hindering chip transport, filling the chip barrel and finally blocking the drill. Drilling into near temperate ice is also problematic as pressure induced melting can cause refreezing of melt water on the drill which then easily gets stuck in the borehole.

We use the lightweight, portable, electromechanical drill FELICS, constructed and manufactured by *icedrill.ch* in Switzerland. The drill is especially designed for operation on high-mountain glaciers where no transport facilities exist except porters [1]. In this project we developed a thermal drill (TD), meeting the requirements use on high-elevation glaciers.

The thermal drill can be used as stand-alone system or in combination with FELICS. Thus, the entire system consists of a tower, winch, cable, and energy supply, alternatively equipped with the modular lightweight EM drill or the TD. In order to allow for transportation by either porters or pack animals, the concept of a light and modular design was also followed for the TD, with a maximal weight of individual pieces not exceeding 30 kg. The total weight is 200 kg for the stand-alone TD, 179 kg for the stand-alone EM drill and 289 kg for of the combined system. This does not include the drilling tent and fuel for power supply.

For switching from the EM drill to the TD, the chips barrel, core barrel and the control unit is exchanged. The TD consists of an upper module and a core barrel which are combined with the existing FELICS drill hoisting system including drill-cable interface, cable and electrical winch. The head of the core barrel, containing an electrical heater element melts an annular space when in contact with the bottom of the borehole, separating the ice core from the glacier.

The crucial technical challenge is the design of the melting head mounted to the core barrel. Its central part is the heating element, a hotspring® coil heater (Hotset, microcoil WRP 3.3) with a diameter of 3.3 mm and 610 mm heated length and two windings. The coil heater is rated with 650 W at 230 V in air. Three designs of the melting head with the same heating element were tested. 1) The open heater has electrical connectors at both ends of the coil, resulting in a crossing over of the coil. 2) The simple aluminum heatspreader, where the connectors of the coil are single ended allowing a spiral shape. 3) The aluminum crown with 90 heatspreader fins, also with single ended connectors (Fig. 1). The coil heaters were used

with an actual power of 2000 W at 400 V. Operation under such high power requires constant contact with the ice for cooling, otherwise the coil heater fuses.

As power supply for the TD two gasoline generators were connected with nominal output of 2000 W each that produced together 1500 W at 3000 m altitude (20 kg each, EU2000i, Honda).

Fig. 1: Melting head with hotspring® coil heater of 100 mm outer diameter. Left: open heater, middle: simple aluminum heat spreader, right: aluminum crown with heatspreader fins.

The TD was used for ice core drilling on two temperate glaciers in the Swiss Alps. From 20 to 25 April 2011, a 101 meter long surface-to-bedrock ice core was collected from Silvretta glacier (46.85°N, 10.09°E, 2927 m a.s.l.). Borehole temperature was around 0ºC and the borehole was filled with melt water. The upper 12 m were drilled with the EM drill before switching to the thermal drill. Thermal ice core production rate was about 1.8 m/h and the total consumption was 70 l of alkylate fuel for the thermally drilled 89 m, corresponding to 0.8 L/m. From 5 to 9 June 2012, two parallel ice cores of 56 m and a 20 m were drilled on Plaine Morte glacier (46.38°N, 7.49°E, 2701 m a.s.l.). This glacier was snow and firn free and the thermal drill was used from the surface. Ice core production rate was higher with approximately 2.8 m/h since the new melting head consisting of the aluminum crown with heatspreader fins was used. The total consumption was 40 L alkylate fuel for 76 m drilled altogether, corresponding to 0.5 L/m. On both glaciers, the thermal drill produced none-fractured ice cores of excellent quality, with an average length of 68 cm of the targeted 70 cm [2].

[1] P. Ginot et al., Mem. Nat. Inst. Polar Research **56**, 38 (2002).
[2] M. Schwikowski et al., Ann. Glac. **55**, 131 (2014).

CHRONOLOGY OF $^{239/240}$Pu AND OF ^{236}U IN THE MIAOERGOU GLACIER FROM EASTERN TIEN SHAN, CHINA

H.W. Gäggeler (Univ. Bern & PSI), S. Hou, Ch. Wang, H. Pang, Y. Liu (Univ. Nanjing),
M. Christl, S. Maxeiner, H.-A. Synal, C. Vockenhuber (ETHZ)

A 57.6 m long ice core was drilled in 2005 to bedrock at the eastern-most glacier of the Tien Shan mountains ranging from Kirgistan to China (43°03'19"N; 94°19'21"E; 4512 m asl) [1]. The core ranges back to about 1851 [2]. This site is interesting since it is a possible collecting location of nuclear debris from the Chinese (Lop Nor) and/or former Soviet (Semipalatinsk) test sites. Indeed using β-counting increased activity was observed between 7 and 12 m depth [1]. Isotope ratios between ^{239}Pu and ^{240}Pu are a fingerprint of the emission source and can be measured very accurately even from ultra-trace amounts of plutonium stored in glacier ice cores using accelerator mass spectrometry (AMS). In addition, recently also ^{236}U has become a widely used tracer for environmental studies but its deposition rate chronology is still poorly known. This nuclide can also be determined via AMS.

The analytical treatment was performed in two steps. The first step was a separation of Pu and U from molten ice samples of about 1 kg in Lanchou by scavenging with manganese hydroxide. These samples were then further processed at Bern University in order to separate Pu and U. First 20 μL ^{233}U standard (91.29 pg/g ^{233}U) = 1.826 pg ^{233}U and 100 μL ^{242}Pu standard (9.16 pg/g = 0.916 pg total) was added. Then U was eluted from a DOWEX 1x8 column with a strong nitric acid solution prior to Pu that was separated with 0.1 M NH$_4$I in 9 M HCl solution to stabilize Pu^{IV}. The U was further purified using a ETUVA column by elution with 0.01 M HCl. Both samples were finally prepared for AMS measurement with 1 mg Fe^{3+} of ultra-pure quality.

Results from ^{239}Pu, ^{240}Pu and ^{236}U were determined with the compact 0.5 MV TANDY accelerator at ETH Zürich for the ice core section between 8 m and 15 m depth. This section corresponds to the period ~1940-1970 [2]. Each sample was 1 m in length for the first and two last samples (with background activity from β-counting) and 0.5 m in length for all other samples (with increased β-activity). The covered time ranges were about 4 years for the 1 m segments and 2 years for the 0.5 m segments, respectively.

The measured concentration pattern showed a pronounced double peak with the following tentative assignment: higher concentrations in the post-moratorium period (maximum at about 1963) compared to the pre-moratorium period (maximum at about 1958) (see Fig. 1 for ^{239}Pu). The ^{240}Pu to ^{239}Pu ratios varied between 0.18 and 0.21, except for the two lowermost samples (Fig. 2). These values are typical for global fallout and do not yield evidence for local sources from Lop Nor or Semipalatinsk.

The ratios (at/at) for ^{236}U to ^{239}Pu were between 0.15 and 0.52 (average 0.32) with rather large uncertainties due to some analytical problems in the separation of plutonium. These values agree with recently measured

values in ice cores from Antarctica that range between 0.18 and 1.4 [3]. Some measured values in sea and river water samples were, however, significantly higher; they ranged from 1.0 to 12.0 [4]. Still, the deposition rates for ^{236}U on a global scale are poorly known and need further study.
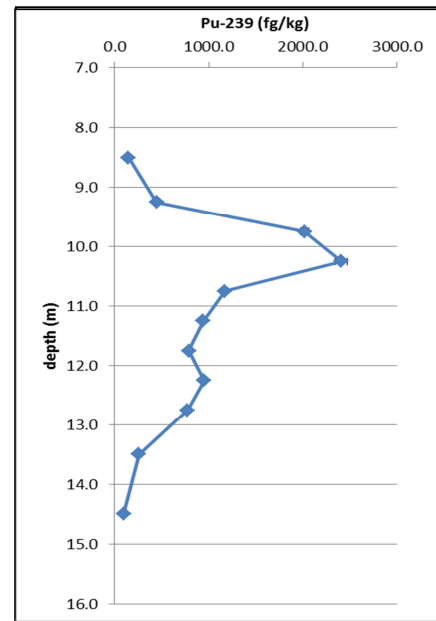
Fig. 1: ^{239}Pu concentration profile along the ice core. Tentatively, the higher peak at about 10 m is attributed to 1963 and the second peak at 12 m to 1958.
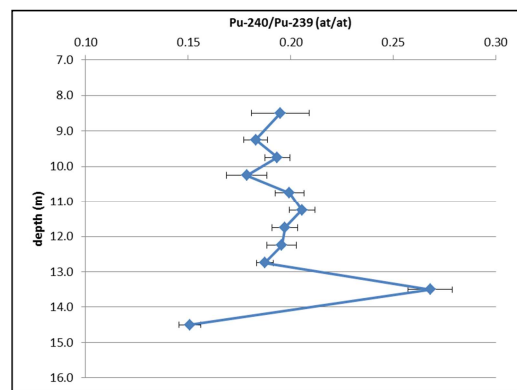
Fig. 2: ^{240}Pu/^{239}Pu ratios along the ice core. Within uncertainty, an average value of about 0.18 is observed. This resembles the global fallout value, hence without any indication for nearby emission sources.

[1] Y. Liu et al., J. Geophys. Res., **116**, D12307 (2011).
[2] Ch. Wang et al., Ann. Glaciol. **55**, 105 (2014).
[3] C.C. Wendel et al., Sci. Total Env. **461-462**, 734 (2013).
[4] R. Eigl et al., J. Env. Radioact. **116**, 54 (2013).

THE OECD-NEA HANDBOOK ON LEAD-BISMUTH EUTECTIC ALLOY AND LEAD PROPERTIES, MATERIALS COMPATIBILITY, THERMAL-HYDRAULICS AND TECHNOLOGIES

J. Neuhausen (PSI), A. Aerts (SCK CEN), J.-C. David (CEA), H. Glasbrenner (ENSI), S. Heinitz (PSI), M. Jolkkonen (KTH), Y. Kurata (JAEA), N. Thiollière (SUBATECH), L. Zanini (ESS AB)

Heavy liquid metals such as Lead-Bismuth Eutectic (LBE) or lead are promising candidate materials to be used as coolant and/or target material in future Accelerator Driven Systems, GenIV reactors and high power spallation targets. However, for their safe and reliable application a lot of knowledge still has to be generated. To co-ordinate and guide the research on nuclear applications of these liquid metals, an Expert Group on Heavy Liquid Metal (HLM) Technology has been founded in 2002 as part of the Working Party on Scientific issues of the Fuel Cycle of the OECD Nuclear Energy Agency (NEA). The aim of this group was to develop a set of requirements and standards as well as consistent methodology for experimentation, data collection and data analyses in this scientific field. The results of these efforts were published in the form of a handbook in 2007 [1].

This handbook has now been updated to include the latest results on topics such HLM properties, materials and testing issues, thermal-hydraulics and system technologies as well as test facilities, safety guidelines and open issues and perspectives of the technology.

LCH was leading the update of chapter 5 of the Handbook, dealing with "Properties of irradiated LBE and Pb". In a major effort, this chapter has been almost completely rewritten to cover topics such as

- Fundamental properties of binary and ternary systems with Pb, Bi and LBE

- Volatilization of hazardous nuclides from liquid metals, including equilibrium and non-equilibrium evaporation as well as gas phase purification

- Solubility of elements in Pb, Bi and LBE

- Polonium migration and surface enrichment in solidified LBE

- Evaluation of thermochemical data for binary systems with Pb and Bi by means of the semi-empirical Miedema model

In a second part of the chapter, experiences from medium and large scale experiments have been compiled, including

- Measurement of gas and volatile element production yields in a p-irradiated molten LBE target in the ISOLDE facility

- Distribution of radionuclides in the proton irradiated ISOLDE target

- Operational experiences from the MEGAPIE project

- Estimation of release of volatiles in accident scenarios for MEGAPIE licensing

- Experiences from the LiSoR irradiation

As the major focus point, the updated chapter now includes a survey of literature data on the thermodynamic quantities that influence the volatilization of radionuclides from liquid metals, arriving at a set of recommended functions for the conservative estimation of the release of volatiles. The chapter also compiles the results on the behaviour of radionuclides in liquid metals generated in the HLM related projects performed in the last ten years such as MEGAPIE [2, 3], EUROTRANS [4], ESS-PP [5], and points to open issues with regard to the behaviour of radioactive nuclear reaction products in liquid metals that have to be resolved to bring HLM technology to maturity. Thus, it is hoped that the text can serve both as a basis for safety assessments for HLM nuclear facilities and also as a foundation of future research in this field.

The single chapters of the updated handbook have undergone a peer-review by experts of high renown in the respective fields. It was very favourably received by the reviewers, and after a final revision by the authors it is now in the editorial phase and will be published late 2014 or early 2015 by the OECD-NEA in form of a download free-of-charge.

---

[1] https://www.oecd-nea.org/science/reports/2007/nea6195-handbook.html

[2] http://megapie.web.psi.ch/

[3] C. Fazio et al., Nucl. Eng. Design **238,** 1471 (2008).

[4] https://www.oecd-nea.org/pt/iempt9/Nimes_Presentations/KNEBEL.pdf

[5] http://web.archive.org/web/20100813093517/http://ess-neutrons.eu

ADSORPTION OF VOLATILE POLONIUM SPECIES ON PLATINUM IN VARIOUS GAS ATMOSPHERES

E. A. Maugeri (PSI), R. Misiak (HNINP), J. Neuhausen, R. Eichler, D. Schumann (PSI)

Polonium isotopes are considered the most hazardous radionuclides produced during the operation of accelerator driven systems (ADS) when lead-bismuth eutectic is used as reactor coolant and as spallation target material. In this work the use of platinum for filtering different polonium species from the cover gas of the ADS reactor was addressed by studying the interaction of Po with Pt using thermochromatography.

^{206}Po was used for the thermochromatographic investigations because of its easily detectable γ-rays and the suitable half-life of 8.8 d. The isotope was obtained by irradiation of bismuth metal disks with a 40 MeV proton beam with up to 3 μA of intensity according to the nuclear reaction: ^{209}Bi(p,4n)^{206}Po. Po was separated from the bismuth matrix before the thermochromatography experiments by evaporation at 1223 K under helium flow and deposited at lower temperatures on Au foils. The thermochromatography setup used in this work consists of a fused silica tube encapsulated in an Inconel® tube placed in a negative temperature gradient furnace, with a temperature profile ranging from 1227 to 168 K. The tube was lined inside with platinum foil placed along the entire temperature gradient.

Two samples, Exp. I and II Fig. 1 (A), were studied using as carrier gas dry He and H$_2$ (<10 ppm H$_2$O), respectively. The deposition pattern obtained in Exp. I is characterized by a peak at 993 K. Considering the chemical potential of the hydrogen carrier gas, elemental Po is the most likely observed species [1]. The thermochromatogram (TC) of Exp. II shows a peak at 1026 K. Considering the use of inert gas and the uncertainty of the method, ± 30 K, the deposited species is considered to be the same as in Exp. I, i.e. elemental Po.

The effects induced by the presence of different concentrations of water in the carrier gas were evaluated in Exp. III–VI. In Exp. III and IV, Fig. 1 (B), H$_2$ with 500 and 1277 ppm of H$_2$O, respectively, was used. The obtained TCs show the formation of a different Po species with higher affinity to Pt, expressed by a higher deposition temperature, 1172 K. Two additional samples were investigated using as carrier gas moist He and H$_2$, respectively, with higher concentration of water (> 2.3 wt.%). The obtained TCs, Exp. V and VI in Fig. 2 (A), show the deposition of one single species between 1217 and 1205 K. This indicates that the high concentration of water in the carrier gas induces the formation of a single Po species, most probably an oxyhydroxide [1], with high affinity for the Pt, in both H$_2$ and He. Another sample was studied using dried O$_2$ as carrier gas. The TC of Exp. VII (Figure 2 (B)) reveals a deposition pattern peaking at 933 K, probably due to the deposition of PoO$_2$.
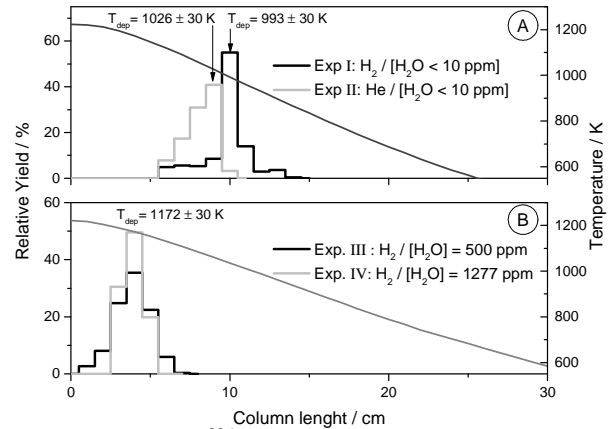
Fig. 1: (A) TCs of ^{206}Po, Exp. I and Exp. II: carrier gas dry H$_2$ and He, respectively. (B) TC of ^{206}Po, Exp. III and IV: carrier gas H$_2$, 500 and 1277 ppm of H$_2$O, respectively.
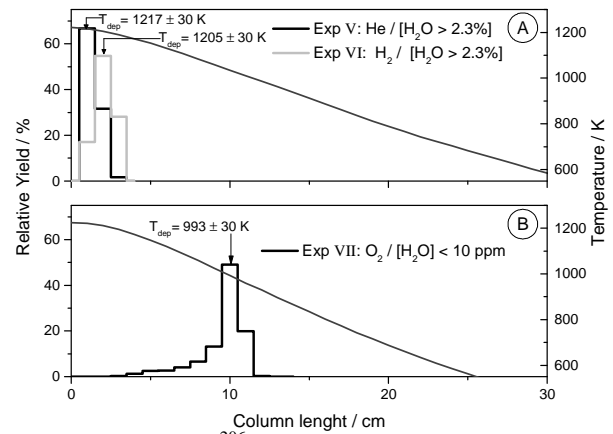
Fig. 2: (A) TCs of ^{206}Po, Exp. IV and Exp. V: carrier gas moist (H$_2$O > 2.3 wt.%) He and H$_2$, respectively. (B) TC of ^{206}Po, Exp. VII dried O$_2$ as carrier gas.

This work reveals that Po has high affinity to Pt, since it is adsorbed at high temperature, 1026 K. It was also demonstrated that the variation of water concentration in the carrier gas, induces the formation of different Po compounds. These species, which may be formed in an ADS reactor by an accidental ingress of water, have even higher affinity to Pt (adsorption temperature between 1217 and 1172 K) making this metal a good candidate for being used as getter material. The metallic state of the Pt has to be preserved, though.

[1]   E.A. Maugeri, et al., J. Nucl. Mater., **450**, 292 (2014).

THE EFFECTS OF WATER ON THE POLONIUM VOLATILISATION ASSESSED BY THERMOCHROMATOGRAPHY EXPERIMENTS

E. A. Maugeri (PSI), R. Misiak (HNINP), J. Neuhausen (PSI), R. Eichler (PSI), D. Schumann (PSI)

In a previous work [1] we studied the formation of Po compounds in different atmospheres using the thermochromatography method. The obtained results showed that water, in both inert and reducing atmosphere, enhanced the formation of species that are more volatile than elemental Po, some of which being gaseous even at room temperature. This project aimed at better understanding the role of water in the formation of these Po volatile species, using a device that allowed a precise measurement of the water concentration during the thermochromatographic experiment.

The preparation of the ^{206}Po used for thermochromatographic investigations and the thermochromatography setup are described in the previous report (with the only exception that in this work quartz columns were used as stationary phase). Moisture concentrations in the carrier gas were measured during the experiments using a dew-point hygrometer (Easidew, Michell Instruments®). Several experiments were performed using either helium or hydrogen as carrier gas, with varied concentrations of water. Three representative ones are presented in this report. Fig. 1, shows the thermochromatogram of ^{206}Po obtained in Exp. I using as carrier gas moist He. The water concentration linearly increased during the 2 hours experiment from 11 to 25 ppm. It is possible to distinguish two deposition patterns. The first, centered at 571 K, was attributed in a previous work to the deposition of elemental Po [2]. The second is a much broader deposition with maxima at 308, 314, 321 and 328 K, respectively. This result confirms that presence of water leads to the formation of various species more volatile than elemental Po. Exp. II was performed using the same carrier gas, helium, but with higher concentration of water, from 36 to 140 ppm. The result superimposed with the result form Exp. I is shown in Fig. 1. The thermochromatogram reveals that at these conditions elemental Po is entirely reacting to form more volatile species. This suggests that the increase of the amount of water in the otherwise inert carrier gas enhances the formation of volatile species, some of them volatile even at room temperature. This also indicates that Po is first at least partly deposited as element at around 571 K. Subsequently, it reacts with water forming new and more volatile species, which are transported to lower temperatures. However, the primary direct formation of part of the volatile species at the high starting temperatures around 1200 K cannot be ruled out. A reaction time in the order of the experimental duration at temperatures around 570 K was observed in Exp. I. The superposition of both effects can lead to split deposition maxima for the same species. Unfortunately, the used method does not allow for a chemical speciation of those volatile species, but the presence of multiple peaks indicates the formation of at least two different species. The carrier free amounts limit the possible species to hydroxides, or hydrides. In Exp. III a sample

was investigated using moist H$_2$ as carrier gas containing constantly 110 ± 7 ppm of water. Fig. 2 shows the thermochromatogram characterized by the presence of a broad deposition pattern between 520 and 340 K with maxima at 435 and 376 K, respectively. This result confirms the formation of species more volatile than elemental Po at reducing conditions in presence of water. Notably, at concentrations of water comparable to Exp. II in Exp. III species with lower volatility, most likely with lower oxidation states, are observed.
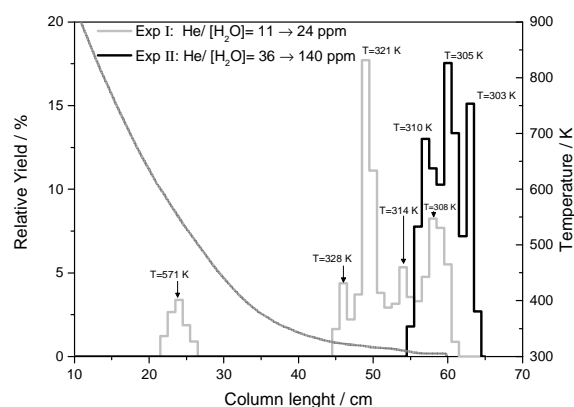
Fig. 1: Superimposed thermochromatograms of ^{206}Po using as carrier gas He with 11-25 ppm (Exp. I) and 36-140 ppm (Exp. II) of water.
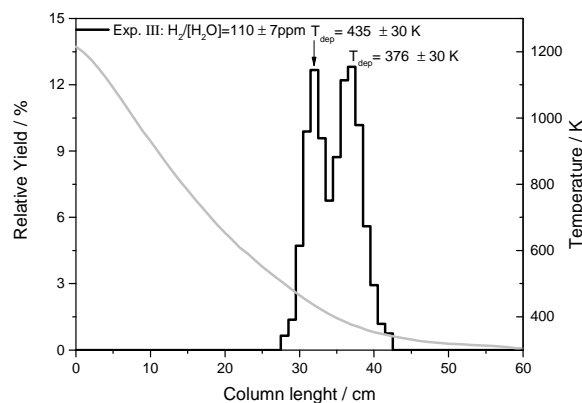
Fig. 2: Thermochromatogram of ^{206}Po using as carrier gas H$_2$ with 110 ppm of water (Exp. III).

This set of experiments confirmed once more that the presence of water enhances the formation of Po species that are more volatile than the elemental Po, and their amount is proportional to the water content. The species observed in carrier gas with moderate oxidation potential revealed a higher volatility compared to the species formed in carrier gas with reducing potential.

---

[1] E.A. Maugeri et al., J. Nucl. Mater., **450**, 292 (2014).

RADIOCHEMICAL DETERMINATION OF LANTHANIDES IN MEGAPIE

B. Hammer (PSI & Uni Bern), J. Neuhausen (PSI), V. Boutellier (PSI), M. Wohlmuther (PSI),
A. Türler (PSI & Uni Bern), D. Schumann (PSI)

After the successful operation of MEGAPIE in 2006 at PSI, an extended PIE program was started to examine the LBE target after irradiation. We reported earlier on the determination of Po isotopes [1] as well as of γ-emitters [2]. The α-emitter ^{148}Gd is safety-relevant because of its relatively long half-life (74ys). Earlier studies of p-irradiated LBE targets showed a high evidence for lanthanide depletion in bulk LBE and their accumulation on surfaces [2, 3]. To assess their distribution more precisely, we studied three kinds of LBE samples from MEGAPIE concerning their lanthanide content: i) samples from bulk LBE, ii) samples from the LBE-steel interface and iii) samples from the contact surface between LBE and the cover gas.

A chemical separation of the lanthanide fraction was performed in order to i) get rid of other γ-emitting isotopes hampering the measurement of ^{173}Lu and ii) prepare a pure, thin measurement sample for the α-spectroscopy of ^{148}Gd.

The sample taking is described elsewhere [2]. The samples were dissolved in HNO_3. After some procedures performed for the determination of I, Cl and Po, the remaining solution was evaporated to dryness and the residue dissolved in 2 ml 0.8M HCl. The solution was spiked with ^{153}Gd, a γ-emitting gadolinium isotope for monitoring the separation and the yield, and loaded on a DOWEX 50Wx8 column. Bismuth, rhodium and further impurities were eluted with 0.9M HCl and 1M HCl, respectively. The remaining lanthanide fraction was eluted with 9M HCl, evaporated to dryness and measured by γ-spectrometry.

The Gd fraction was then further purified using the specific Ln-resin from TRISKEM. The residue was loaded onto the column in 5 ml 0.01M HNO_3. After removing Ba and Au with the feeding solution, Gd is eluted with 0.6M HNO_3 and evaporated to dryness. The sample preparation was performed using molecular plating with 100 µl 0.01M HNO_3 and 2 ml butanol.

In Figure 1, the measured activity concentrations of ^{173}Lu in 4 bulk samples is shown. Compared to the expected concentrations obtained from theoretical predictions assuming homogeneous distribution in the LBE clearly lower concentrations are measured. Extrapolating from the average activity concentration of the measured samples, only about 7 % of the predicted ^{173}Lu are contained in the LBE (Tab. 1). ^{148}Gd concentrations in the LBE were below the detection limit.
A considerable amount of both ^{173}Lu and ^{148}Gd were detected on both types of surface samples. Assuming the activity per surface area measured in the interface samples is representative for all similar surfaces in the target, we roughly estimate the amount of the two nuclides deposited at the interfaces by scaling up to the total areas of the target container walls and the LBE

covergas interface obtained from construction drawings. The resulting activities are compiled in Table 1. It can be concluded that the major part of the produced ^{173}Lu and ^{148}Gd separates from the LBE and is deposited on the steel walls of the target container. The total activities estimated for the complete target from the analytical data agree fairly well with those obtained from theoretical predictions.
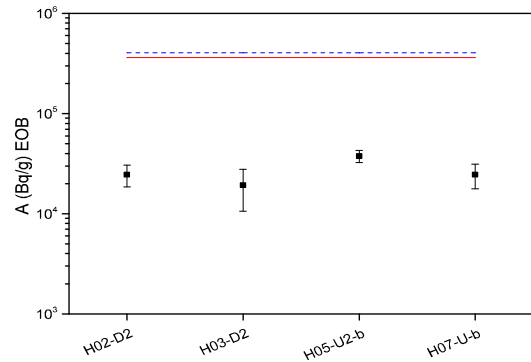
Fig. 1: Activity concentration of ^{173}Lu at EoB (21.12.2006) in 4 representative bulk LBE samples compared to FLUKA (red) and MCNPX blue dashed) predictions.

Tab. 1: Total ^{148}Gd (top) and ^{173}Lu (bottom) activities at EoB for bulk LBE and surfaces within the MEGAPIE target. [1]free surface estimated as 300cm^2; [2]inner surface of steel wall approx. 16m^2.

^{148}Gd	measured total [MBq]	predicted [MBq]	% of predicted amount
bulk	not detected		-
free surface[1]	1.1	153	<1
LBE/steel surface[2]	75.6		71
^{173}Lu	measured total [GBq]	predicted [GBq]	% of predicted amount
bulk	22.4		7
free surface[1]	6.1	321	<2
LBE/steel surface[2]	194.3		60

[1] B. Hammer et al., Nuclear Data Sheets, **119**, p. 280-283 (2014).
[2] B. Hammer et al., J. Nucl. Mater., **450**, p. 78-286 (2013).
[3] B. Hammer, Master Thesis, Univ. Bern, 2010.

PREPARATION OF A RADIOACTIVE THULIUM TARGET FOR CERN n_TOF

S. Heinitz, D. Schumann, R. Dressler, E. A. Maugeri (PSI), N. Kivel (PSI/AHL),
U. Köster (ILL), C. Guerrero Sanchez and the n_TOF collaboration (CERN)

In order to understand the natural abundances of the elements in the solar system, a detailed knowledge on the neutron capture reactions during element synthesis in stars is mandatory. Although the theoretical principles of the involved processes were described almost 60 years ago [1], reaction pathways involving unstable nuclei remain uncertain, since here neutron capture competes with radioactive decay. The CERN n_TOF community has the goal to precisely measure neutron cross section data for stable as well as for radioactive isotopes. However, samples of radioactive nuclides are hardly available to the scientific community in sufficiently high amounts. Among them, ^{171}Tm is a prominent example.

We have separated 4 mg of ^{171}Tm from 238 mg of irradiated ^{170}Er$_2$O$_3$ using ion exchange chromatography. The purified material contained 160 GBq of ^{171}Tm and was electrodeposited on two Al foils and delivered to the CERN n_TOF community for neutron cross section measurements.

A quartz ampule containing ^{170}Er$_2$O$_3$ enriched to 98.1 % was irradiated for 55d at the Institut Laue-Langevin, Grenoble, France, to accumulate approx. 270 GBq ^{171}Tm. After a 1 y cool-down and shipment to PSI, the ampule was cracked and the oxide dissolved in 5 ml 7M HNO$_3$ in a special apparatus placed inside a glovebox. After evaporation of the acid, the material was dissolved in H$_2$O and mixed with 1 MBq of ^{171}Er produced by neutron activation at the SINQ.
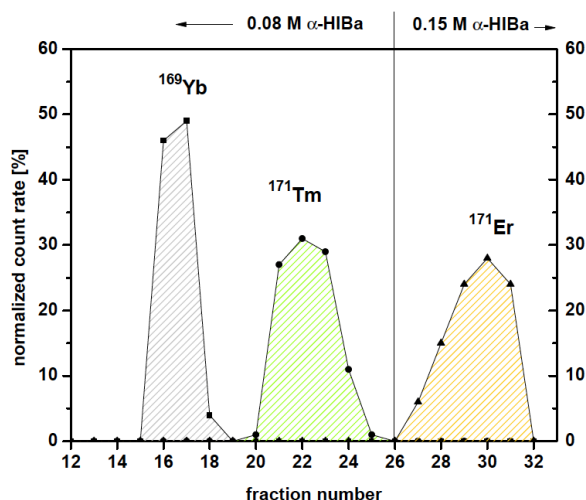
Fig. 1: Elution profile for the separation of ^{171}Tm

Five subsequent separations have been performed using two 25 cm long columns filled with Aminex HPX87H cation exchange resin. 0.08 M α–hydroxyisobutyric acid (α-HIBa) at pH = 4.40 served as elution medium. The elution profile is shown in Fig. 1. Finally, all solutions containing ^{171}Tm were unified, acidified to a pH of 0.5 and loaded on another column filled with the Eichrom LN1 resin for the final

purification from α-HIBa and remaining Er/Yb. The elution of Tm was performed with 4M Tracepur HNO$_3$ to yield a final solution that had a dose rate of approx. 10 mSv/h.

In order to characterize the purified material, several aliquots of the solution were taken and measurement techniques involving γ-spectroscopy, liquid scintillation and Cherenkov counting as well as ICP-MS are going to be used for sample characterization.

After evaporation of the final solution, the deposit was dissolved in 100 μL 0.01M HNO$_3$ and 2 ml isopropanol and divided in two equivalent fractions. Molecular plating of ^{171}Tm was performed with each fraction on a circular Al foil at a voltage of 300 V for 30 min.

The final target assembly consisted of two 5 μm thick Al foils, 25 mm in diameter, stacked between two 6 μm mylar foils mounted on a circular frame. The mylar foils were welded together to ensure an encapsulation of the radioactive material and to avoid contamination issues. The final target assembly is shown in Fig. 2.

Fig. 2: Final ^{171}Tm target delivered to the CERN n_TOF community.

Preliminary results from ICP-MS indicate that the sample contains Thulium in the isotopic composition of ^{169}Tm to ^{170}Tm to ^{171}Tm as 1/48 : 1/1500 : 1. A decontamination factor from the matrix material ^{170}Er of at least 10^4 was reached. The overall deposition yield on Al was 93.5%, the final target contains at least 145 GBq ^{171}Tm. A precise characterization of the delivered target is ongoing.

[1] E. M. Burbidge et al., Reviews of Modern Physics, vol. **29**, Issue 4, pp. 547-650 (1957).

^{210}Po INGROWTH FROM ^{210}Pb IN THE MEGAPIE TARGET

B. Hammer (PSI & Uni Bern), J. Neuhausen (PSI), M. Wohlmuther (PSI/ABE), A. Türler (PSI & Uni Bern), D. Schumann (PSI)

In future high power spallation targets and accelerator driven transmutation facilities lead-bismuth eutectic (LBE) is considered to be used as target and coolant material. One of the most significant problems when using LBE is the production of significant amounts of the highly radiotoxic ^{210}Po.

In the recent analysis of a lead target from SINQ surprisingly high ^{210}Po concentrations were observed, leading to further investigations of this phenomenon [1]. While in the beginning only nuclear reaction channels involving the interaction of protons and neutrons with the target material were considered for the production of ^{210}Po, the analysis of the Pb-target revealed that ^{210}Po is not only produced via ^{209}Bi that is either present as impurity in the target material or formed from ^{208}Pb by (n,γ) reaction, but also in a reaction channel involving ^{210}Pb. A possible reaction pathway for producing ^{210}Pb is the reaction of ^{208}Pb with secondary particles carrying two neutrons (^{3}H and ^{4}He). The double-neutron capture of ^{208}Pb seems unlikely due to the non-sufficient neutron flux and the short half-life of the intermediate ^{209}Pb.

^{208}Pb(^{3}H,p)^{210}Pb
^{208}Pb(α,$2p$)^{210}Pb
^{210}Pb(β^-)^{210}Bi(β^-)^{210}Po
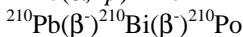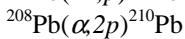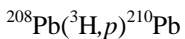
In this work, the contribution of this production channel for ^{210}Po via ^{210}Pb is studied for the MEGAPIE target.

The chemical separation of Po from irradiated LBE and the preparation of samples for α-spectrometry have been described in [2]. In these investigations, performed in 2012 after the MEGAPIE target had decayed for six years, all ^{210}Po produced both via neutron capture from ^{209}Bi and via the formation of ^{210}Pb by the above mentioned path were deposited from the solution and quantified by α-spectrometry. The ^{210}Pb remains in solution, and its decay leads to an ingrowth of ^{210}Po in the solution, allowing the assessment of its ^{210}Pb content via a second deposition and α-spectrometric determination of its daughter. For this purpose, the deposition of Po onto silver discs was repeated after 1.5 years of ^{210}Po ingrowth for several solutions studied in [2]. In this way, the contribution of the reaction path leading to the production of ^{210}Po via ^{210}Pb can be determined.

In Fig. 1, decay curves are presented that were calculated from the experimental results for the ^{210}Po content obtained in the first deposition [2] and the ^{210}Pb content obtained in the 2nd deposition. These are compared to MCNPX 2.5.0 (INCL4-ABLA) + CINDER'90 predictions [3]. In both cases, the predictions are slightly higher compared to the experimental results, but the agreement can be considered satisfactory. At end of beam, the amount of ^{210}Po resulting from

production channels via ^{209}Bi clearly dominates, as it was expected for a target material containing more than 50 % bismuth. However, ^{210}Po decays with a half-life of 138 days. As a result, after a decay period of about 10 years the contribution of ^{210}Po continuously produced by the decay of the more long-lived ^{210}Pb ($t_{1/2}$ = 22.3 y) contained in the irradiated target material becomes dominant. From this point in time onwards the ^{210}Po activity in the irradiated LBE will follow the decay behaviour of its long-lived mother ^{210}Pb. This behaviour has to be considered in the safety assessment for the disposal of the irradiated target.
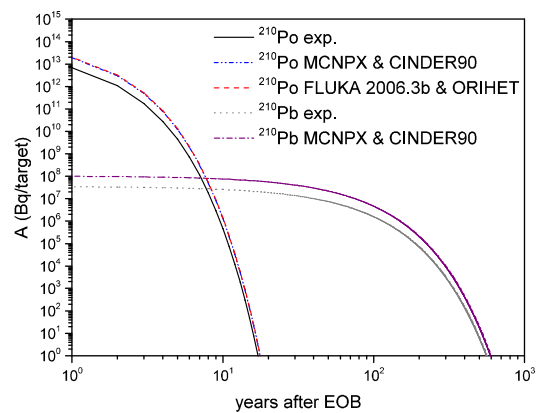
Fig. 1: Comparison of ^{210}Po contribution of ^{209}Bi and ^{210}Pb compared to predictions.

It was proven that ^{210}Po in MEGAPIE is not only produced directly or indirectly from ^{209}Bi but also via ^{210}Pb. The most likely reaction pathway for producing ^{210}Pb is the reaction of ^{208}Pb with secondary particles carrying two neutrons (^{3}H and ^{4}He). The contribution of ^{210}Po resulting from the latter mechanism in the MEGAPIE target was experimentally determined as 35 ± 3.49 MBq at EoB. Compared to ^{210}Po formed from stable Bi, this is negligible at EoB, however after decay times >10 y it becomes the dominating source of ^{210}Po in the irradiated target material. Both production channels are reasonably well represented in the version of the MCNPX code that was used to predict the MEGAPIE inventory [3].

[1] D. Kiselev et al., Po-production in lead: Calculation and measurement on SINQ-samples (PSI), SATIF-12 Proc. (2014).

[2] B. Hammer et al., Nucl. Data Sheets, p. 280-284 (2014).

[3] L. Zanini et al., PSI Report Nr. 08-04 (2008).

CORROSION OF TUNGSTEN IN THE SINQ COOLING WATER

D. Schumann, T. Stowasser. S. Köchli (PSI), J. Eikenberg, M. Rüthi (PSI/ASI), B. Blau, F. Heinrich,
K. Geissmann (PSI/ASQ), Y. Dai (PSI/LNM)

PSI operates one of the most powerful neutron spallation sources in the world - SINQ. The heat deposition in the target requires a high-sophisticated cooling system, consisting of three independent loops (target window, target and moderator). The target is composed of zircalloy-cladded lead rods. Some of the rods contain samples for material studies in the frame of the STIP program [1]. In the present target, among others, several tungsten pieces are placed.

In autumn 2013, a significant activity increase in the cooling water of the target cooling loop was observed, referring to a possible rod crack, as happened already in 2010. The data of the analysis are shown in Table 1. Interestingly, the nuclide vector was different from the one determined in 2010, being not typical for a broken lead rod due to missing ^{207}Bi and other radionuclides produced in lead. The enhanced content of Hf, Ta and lanthanide isotopes gives high evidence for a broken STIP rod containing tungsten samples.

Tab.1: Activity concentrations in [kBq/kg] of selected radionuclides in the water of the target cooling loop produced from W, measured on 10.1.2014.

^{175}Hf	^{182}Ta	^{184}Re	^{183}Re
390	236	37	17
^{171}Lu	^{172}Lu	^{173}Lu	^{177}Lu
37	206	137	105

Since the activity concentrations in all cooling loops did not exceed any limits, the target was also operated in 2014. However, in order to evaluate the impact of the tungsten corrosion on the performance of the target, we carried out a model experiment with identical STIP material and a sample from the cooling water.

A tungsten piece (mass 6.2 g, surface appr. 3.2 cm^2), identical to that present now in the SINQ target, was inserted into a two-neck flask. 100 ml of SINQ water (D_2O, ultrapure, completely deuterated) were added. The sample was heated up to 80°C for 4 weeks using reflux cooling, thus simulating the conditions in SINQ. A yellow precipitate was formed during the experiment, as can be seen in Figure 1. The precipitate, consisting of a mixture of H_2WO_4 and $WO_3 \cdot (H_2O)$ was dissolved in diluted NaOH and analysed concerning the tungsten content with Inductively-Coupled Optical Emission Spectrometry (ICP-OES).
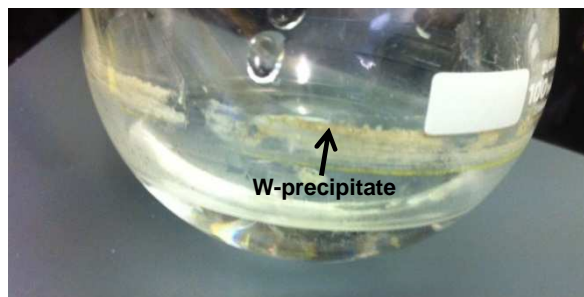
Fig. 1: Photo of the experiment vessel after 4 weeks heating to 80°C.

The analysis showed that 7 mg of tungsten dissolved in the SINQ water during 4 weeks at 80°C, corresponding to more than 0.1% of the total amount of tungsten present in the vessel. Literature data report corrosion values of 3.8 µg/m^{2}h at 38°C [1]. Taking into account, that our test does not meet all experimental conditions – we have no dynamic flow and the influence of irradiation on the solubility behaviour was not considered – the amount of dissolved tungsten for a SINQ operation time of several months is probably not negligible. In particular, the dissolved tungsten can be precipitated again on colder places.

Before the restart of SINQ in April 2014, a fresh filter was installed into the purification unit, in order to optimize the absorption capacity for the produced radionuclides. Though routine activity measurements showed indeed further presence of radionuclides produced from tungsten – in this case also the short-lived ^{187}W (T$_{1/2}$=1d) could be identified - (see values in Table 2), the rod damage did not affect the performance of the target. Further measurements later this year showed no significant activity increase, thus indicating the efficiency of the installed fresh filter.

Tab. 2: Activity concentrations in [kBq/kg] of selected radionuclides in the water of the target cooling loop produced from W, measured on 4.6.2014.

^{175}Hf	^{182}Ta	^{184}Re	^{183}Re
14	15	8	6
^{171}Lu	^{172}Lu	^{173}Lu	^{187}W
16	16	26	1521

[1] Y. Dai. et.al. „JNM 296 43 (2001).
[2] E. Lassner, W.-D. Schubert, Tungsten, Kluwer Academic/Plenum publishers, New York 1999 (2010).

THE RADIONUCLIDE INVENTORY OF A SINQ TARGET

T. Lorenz (Univ. Bern & PSI), D. Schumann, R. Dressler (PSI), Y. Dai (PSI/LNM), M. Wohlmuther,
D. Kiselev (PSI/ABE), A. Türler (Univ. Bern & PSI)

This work describes the investigation of the radionuclide inventory of a solid lead target from SINQ at PSI, operated from March 2000 to December 2001. A total beam charge of 10.03 Ah was deposited inside an arrangement of more than 300 lead filled steel rods. Samples from different positions in the target were obtained and a set of 19 relevant long-lived radionuclides was analysed using γ-ray spectrometry, α-particle spectrometry and accelerator mass spectrometry (AMS). This kind of data set is requested from the Swiss authorities to issue permission for conditioning and disposal of SINQ targets.

In previous works, the studies on the activity concentration of strong γ-emitters [1], of polonium [2], of ^{36}Cl and ^{129}I [3] and of α-particle emitting lanthanides ^{146}Sm, ^{148}Gd and ^{150}Gd [4] in samples from Rod 3 were presented. Further analysis of samples along the beam axis now provided a data basis to calculate the total radionuclide inventory and its spatial activity distribution. The sample positions are indicated in Fig. 1.
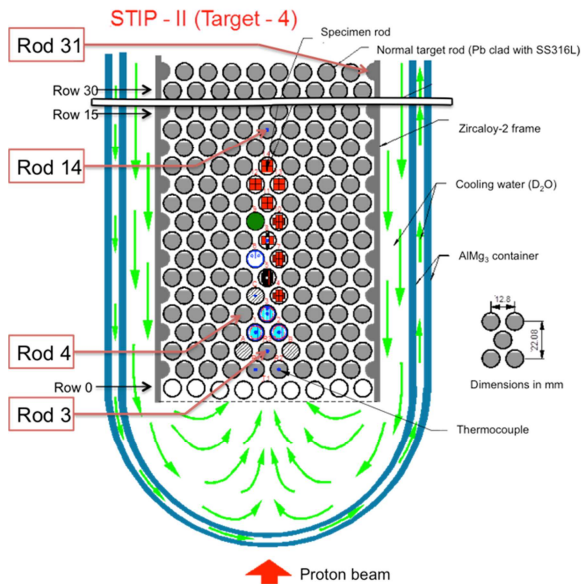
Fig. 1: Scheme of the arrangement of the rods in Target 4. The available rods for sampling are indicated.

Details on the separation and measurement of the relevant nuclides are given in the references above. The integral radioactive inventory was calculated using the computer assisted interpolation method of Kriging [5] and the scientific graphing and data analysis software Origin® from OriginLab.

The total spatial distribution radial and in direction of beam was visualized in a two-dimensional contour plot (see Fig. 2).
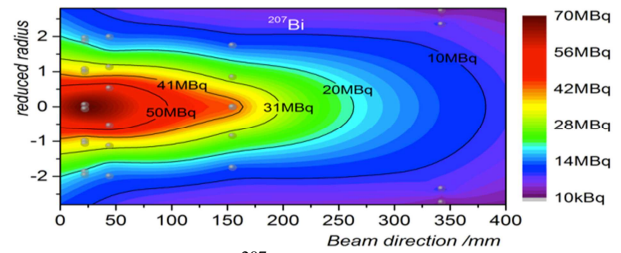
Fig. 2: Example of ^{207}Bi as contour plot of the 2D interpolation using the Kriging algorithm. The data points are indicated in grey. The resulting total activities of the relevant nuclides are given in Tab. 1 at end of beam (EOB

Tab. 1: Total activities of 19 relevant radionuclides for 31 kg of target material at EOB calculated based on measured values

Nuclide	Activity /Bq	Nuclide	Activity /Bq
^{173}Lu	$4.92 \cdot 10^{12}$	^{108m}Ag	$9.64 \cdot 10^{9}$
^{172}Hf	$2.06 \cdot 10^{12}$	^{202}Pb	$9.27 \cdot 10^{9}$
^{207}Bi	$1.33 \cdot 10^{12}$	^{209}Po	$7.43 \cdot 10^{8}$
^{102}Rh	$4.70 \cdot 10^{11}$	^{210}Pb	$7.08 \cdot 10^{8}$
^{125}Sb	$4.32 \cdot 10^{11}$	^{148}Gd	$2.16 \cdot 10^{8}$
^{194}Hg	$3.97 \cdot 10^{11}$	^{36}Cl	$6.97 \cdot 10^{5}$
^{60}Co	$1.73 \cdot 10^{11}$	^{150}Gd	$7.41 \cdot 10^{4}$
^{101}Rh	$1.66 \cdot 10^{11}$	^{129}I	$1.77 \cdot 10^{4}$
^{133}Ba	$6.15 \cdot 10^{10}$	^{146}Sm	$2.33 \cdot 10^{3}$
^{208}Po	$3.26 \cdot 10^{10}$	**TOTAL:**	$1.01 \cdot 10^{13}$

In most cases, the results are in good agreement with theoretical predictions using two physics models (see Fig. 3). Predictions of ^{108m}Ag, $^{208/209}$Po, and ^{210}Pb vary widely, due to differences in the simulation of the respective production mechanisms.
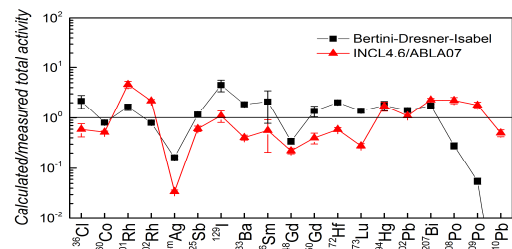
Fig. 3: Ratio of calculated to measured data.

[1] T. Lorenz et.al. Y. Dai, Radiochim. Acta, **101** (2013) 661.

[2] T. Lorenz et.al., Nucl. Data Sheets, **119** (2013) 284.

[3] T. Lorenz et.al., Ann. Rep., Lab. of Radio- & Environ. Chem., Univ. Bern & PSI, (2012), p. 46.

[4] T. Lorenz et.al., Ann. Rep., Lab. of Radio- & Environ. Chem., Univ. Bern & PSI, (2013), p. 48.

[5] G.M. Laslett, J. Am. Stat. Assoc., 89 (1994) 391.

NEW RbCl TARGETS FOR ^{82}Sr PRODUCTION

C. Vermeulen (PSI/CRS), N.P. van der Meulen (PSI)

The Positron Emission Tomography (PET) radioisotope, ^{82}Sr, is currently a sought after commodity for use in medical generators. Particularly in North America demand by particularly cardiologists has shown steady growth and increased markedly with the shortage of ^{99}Tc due to reactor outages. ^{82}Sr *(T$_{1/2}$=25.5d)* decays purely by EC to the short-lived ^{82}Rb *(T$_{1/2}$=1.3min, Iβ$^+$=95%, EC=5%; Eβ$^+$=3.1MeV, Eγ=776.5keV, Iγ=13.4%, Iγ=13.4%)* [1]

^{82}Rb *(T$_{1/2}$=76s)*, behaves physiologically much like potassium. It is therefore very effective for myocardial infusion imaging studies using PET [2]. This technique has shown better image resolution and image contrast than its Single Photon Emission Computed Tomography (SPECT) counterpart, ^{99}Tc-MIBI, for monitoring coronary disease patients [3]. ^{82}Rb has also found use PET measurement of blood-to-brain and blood-to-tumor transport of Rb [4].

Fig. 1: New RbCl target assembly. (Exploded View)

A new target has been developed for the production of ^{82}Sr at PSI in the IP2 irradiation facility. The target consists of a RbCl pellet encapsulated in Stainless Steel, situated in the high energy slot of a tandem configuration. The lower energy slot is occupied by an aluminium beam-stop, equipped with extra cooling channels to efficiently remove the energy deposited by the Bragg peak of the proton beam.

The target is intended to be run for a maximum bombardment of 10'000 µAh before being shipped to the US DOE laboratories at Los Almaos for processing. A test run was performed with full size production targets to develop beam parameters and collect initial radiation measurements. The 72 MeV proton beam was requested to have a diameter of ~30mm at 2 Sigma. The size and alignment of the beam was checked by performing a 10 min bombardment at the full requested intensity of 50uA and then exposing a radiochromic foil to the target [5]. Post activation analysis shows good alignment and excellent beam characteristics in the "direct shot" configuration of the IP2 injector cyclotron. (Fig. 2)

Visual inspection showed no visible change to the target and measurements of the target dimensions showed no detectable physical deformation.

The test targets were returned to the beam for another hour and inspected again. No changes were again detected in both visual appearance and physical dimensions. These results lead us to consider the targets ready for long term bombardments in 2015 and beyond.
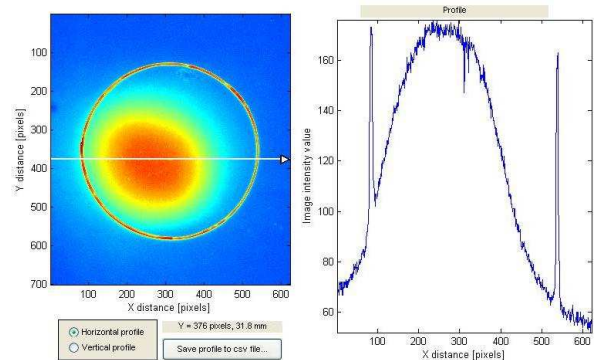
Fig. 2: Radiochromic film beam profile measurement

[1] S. Qaim et al., App. Radiat. Isot. **65**, 247-252, 2007.

[2] N. A. Mullani et al., J. Nucl. Med. **24**, 898-906, 1983.

[3] M. Schwaiger et al., Cardiac Positron Emission Tomography, Springer, 121-146, 1996.

[4] J. O. Jarden et al., Annals of neurology **18**, 636-646, 1985.

[5] J. F. Dempsey et al., Medical Physics **27**, 2462-2475, 2000.

^{43}Sc PRODUCTION DEVELOPMENT BY CYCLOTRON IRRADIATION OF ^{43}Ca AND ^{46}Ti

K. Domnanich (Univ. Bern & PSI), C. Müller (ETHZ & PSI), A. Sommerhalder (PSI), R. Schibli (ETHZ & PSI), A. Türler (Univ. Bern & PSI), N.P. van der Meulen (PSI), B. Lommel, V. Yakusheva (GSI)

The positron emitter ^{43}Sc is considered to be an attractive PET (positron emission tomography) radionuclidic alternative to ^{44}Sc (Table 1), due to its more favourable decay properties. What is more, the lower energetic gamma line will result in a lower radiation dose burden for the patient and the operator. [1]

Tab. 1: Comparison of nuclear properties of ^{43}Sc and ^{44}Sc

	^{43}Sc	^{44}Sc
$t_{1/2}$	3.89 h	3.97 h
β^+ emission	88%	95%
$E\beta_{max}$	1.20 MeV	1.47 MeV
Main γ-ray [keV]	372.8 (23%)	1157 (99%)

Together with ^{47}Sc, which demonstrates therapeutic effect by emitting soft β^- particles, it can be considered as a "matched pair", enabling tumour imaging and, based thereon, optimal therapy planning. The production of ^{43}Sc is described by several different nuclear reactions in literature: ^{42}Ca(d,n)^{43}Sc, ^{43}Ca(p,n)^{43}Sc, and ^{46}Ti(p,α)^{43}Sc [1-3]. The feasibility of the two latter production pathways was tested at the PSI Injector II cyclotron.

Irradiation. ^{43}Ca-targets were prepared by mixing either 10 mg of enriched ^{43}CaCO$_3$ or ^{46}Ti with 150 mg graphite powder, pressed and encapsulated in aluminium. The ^{43}CaCO$_3$ and ^{46}Ti targets were irradiated with 72 MeV protons, degraded to ~10.4, 12 and 17.7 MeV, respectively, at an integrated current of 75 µAh.

Chemical separation: To chemically separate ^{43}Ca from ^{43}Sc, the method optimised for ^{44}Sc-separation (see "Optimisation of ^{44}Sc Production by Cyclotron Irradiation of ^{44}Ca for Radiopharmaceutical Applications") was used. The final product was obtained in 700 µL 4.8 M NaCl/0.13 M HCl solution, which was used directly for labelling reactions with DOTANOC.
Separation of ^{46}Ti from ^{43}Sc: In order to dissolve the irradiated target, it was heated in 6 M HCl for 15-20 min. After adjusting the concentration to 4 M, the solution was passed over a DGA extraction chromatographic resin, where ^{43}Sc(III) was sorbed. As Ti(III) is not retained on the resin under these conditions, it was eluted from the column with further addition of 4 M HCl. 0.05 M HCl was used to elute ^{43}Sc from the DGA column and the solution passed over a second column, consisting of SCX cation exchange resin. The elution of the final product was performed with 700 µL 4.8 M NaCl/0.13 M HCl solution

For the production of ^{43}Ca(p,n)^{43}Sc, the ^{43}CaCO$_3$ target was irradiated with a 10.4 and 12.1 MeV proton beam for 1.5 h. The yield at the EOB (end of bombardment) and EOS (end of separation) are summarised in Table 2.

Tab. 2: Obtained ^{43}Sc activity at EOB (end of bombardment) and EOS (end of separation) and the ^{43}Sc/ total activity ratio

	~12 MeV		~10.4 MeV	
EOB ^{43}Sc [MBq]	910	584	455	186
EOS ^{43}Sc [MBq]	312	348	270	120
^{43}Sc/ (^{43}Sc+^{44}Sc)	66%	66%	65%	67%

The percentage of ^{44}Sc is about 33% of the total activity after EOS. This ratio is first influenced by the enrichment of the ^{43}Ca used, which still contains 12.4% ^{44}Ca and can yield ^{44}Sc via the ^{44}Ca(p,n)^{44}Sc reaction. Secondly, the energy of the proton beam has a crucial role to play, as the optimum yield centres at around 10 MeV.

The produced ^{43}Sc was used to perform a PET phantom study at the ETH Zürich, showing promising preliminary results for ^{43}Sc being a superior PET nuclide to its ^{44}Sc counterpart. The lower positron emission energy of ^{43}Sc increases the resolution of the obtained PET image, compared to ^{44}Sc.
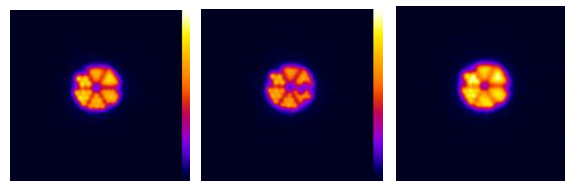
Fig. 1: PET-Phantom Scans from 10 MBq and 4 MBq ^{43}Sc (left and middle image) and 4 MBq ^{44}Sc (right image)

The labelling of the obtained ^{43}Sc with DOTANOC could be performed at a maximum specifity of 7 MBq ^{43}Sc/nmol DOTANOC.
Since enriched Ti is only available in oxide form, the first step was the reduction of 97% ^{46}TiO$_2$ to ^{46}Ti at GSI, Darmstadt [4].The production of ^{46}Ti(p,α)^{43}Sc was done by irradiating the target with ~17.7 MeV protons for 1.5 h, yielding 30 MBq ^{43}Sc at EOB. At EOS 24 MBq ^{43}Sc could be eluted, with <0.01% ^{46}Sc measured as an impurity. The irradiation conditions require optimisation.

[1] S. Krajewski et al., ichti Annual Report 2012, Warszawa, (2013), p. 35.
[2] P. Kopecky et al., Appl. Radiat. Isotope. Vol. **44**, No. 4, pp. 681-692, (1993).
[3] EXFOR- database, version from 03.12.2014
[4] B. Lommel et al., J Radioanal Nucl Chem, **299**, 977 (2014).

OPTIMISATION OF ^{44}Sc PRODUCTION BY CYCLOTRON IRRADIATION OF ^{44}Ca FOR RADIOPHARMACEUTICAL APPLICATIONS

K. Domnanich (Univ. Bern & PSI), C. Müller (ETHZ & PSI), A. Sommerhalder (PSI), R. Schibli (ETHZ & PSI), A. Türler (Univ. Bern & PSI), N.P. van der Meulen (PSI)

^{44}Sc is a promising β^+ emitter for PET (positron emission tomography) imaging ($t_{1/2}$ = 3.97 h, $E_{\beta+}$ 1475.4 keV, 94.34%) and could be an alternative to the currently-used short-lived ^{68}Ga ($t_{1/2}$ = 68 min). It has been shown that Sc^{3+} behaves chemically similarly to the lanthanides and rare earth elements (^{90}Y^{3+}, ^{177}Lu^{3+}), forming DOTA complexes with coordination number 8, whereas ^{68}Ga^{3+} forms octahedral complexes. ^{44}Sc can be used in already established labelling reactions for radiopharmaceutical purposes [1-3]. The aim of this study was the further development of the ^{44}Sc separation method and subsequent radiolabelling experiments. A method for target recycling was developed. Recently, the produced DOTATOC-radiolabelled ^{44}Sc was applied to two patients, enabling the recording of several whole-body PET/CT scans.

Irradiation. ^{44}Ca-targets were prepared by mixing 10 mg enriched ^{44}CaCO$_3$ with 150 mg graphite powder, pressed and encapsulated in aluminium. The targets were irradiated at PSI with 72 MeV protons, degraded to 11.5 MeV, at a beam current of 75 μAh.

Chemical separation. 3 M HCl was used to dissolve the ^{44}CaCO$_3$ and the resultant solution was loaded on to DGA extraction chromatographic resin, where ^{44}Sc(III) was sorbed. ^{44}Ca(II) is not retained and was eluted from the column with further addition of 3 M HCl. ^{44}Sc(III) was eluted with 0.1 M HCl from the column and sorbed on the second column consisting of SCX cation exchange resin. It was, subsequently, eluted with 700 μL 4.8 M NaCl/ 0.13 M HCl and directly used for labelling reactions with DOTANOC.

^{44}Ca target recovery. The liquid ^{44}Ca-containing waste was evaporated to complete dryness, dissolved in water and precipitated as ^{44}Ca-Oxalate in the pH range of 4.5-5. The precipitate was then filtered through a porcelain filter crucible and the oxalate converted to the carbonate by slowly heating it to 500 °C. The overall yield of the described method was 98%.

Chemical Separation

The previously-used separation method for ^{44}Sc included the use of Dowex 50W-X2 as the second column, a cation exchange resin for concentration purposes. The elution required up to 1.5-2 mL NH$_4$Ac/ HCl solution, fractionised in three vials, while the currently-implemented SCX cation exchange column requires only 700 μL 4.8 M NaCl/0.13 M HCl solution.

This method is also currently used for the elution of ^{68}Ga from the ^{68}Ge/^{68}Ga generator [4]. The results obtained showed a 98% ±0.24 trapping of ^{44}Sc in the final eluate.

Radiolabelling

The radiolabelling reaction with ^{44}Sc was performed with a specificity of 10 MBq ^{44}Sc/nmol DOTANOC, yielding a high percentage of radiolabelled compound (99% ± 1.6) in the pH range of 3-4.5. Labelling yields dropped dramatically to 49.3% ±31 when decreasing the pH to 2-2.5. The obtained results indicate a robust, reproducible radiolabelling in the pH range of 3-4.5.

Recently, the produced ^{44}Sc was shipped over 600 km to Germany to the THERANOSTICS Research Center (TRC) at Zentralklinik Bad Berka (ZBB), where radiolabelling was performed using DOTATOC with high radiolabelling purity. Whole-body PET/CT scans (Biograph mCT Flow 64) were performed in 2 patients post injection (p.i.) of 100 MBq of Sc-44 DOTATOC at 10, 25, 60 minutes as well as 2, 4 and 16 and 23 hours. The scans showed excellent uptake (best seen after 2 to 4 h p.i.) and even very small hepatic metastases from a well differentiated neuroendocrine tumor of the pancreas could be detected with very high resolution and excellent contrast (Figure 1). More hepatic lesions were detected by Sc-44 DOTATOC PET/CT as compared to MRI and ultrasound (which were performed in the patient on the same day) and a tiny new lesion was newly recognized in one patient when compared to a previous Ga-68 DOTATOC study performed 9 months before.
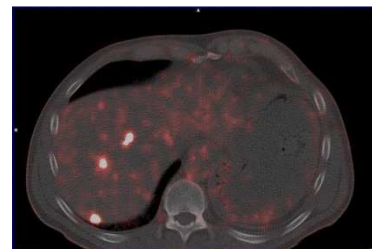
Fig. 1: Whole-body PET/CT scan (4 h p.i.) of a 63-year-old male patient with somatostatin receptor positive liver metastases from a pancreatic neuroendocrine neoplasms and one corresponding transversal slice through the liver, demonstrating small metastases in the right hepatic lobe. [5]

[1] K. Zhernosekov et al., Radiother. Oncol. **102**, 141 (2012).

[2] S. Krajewski et al., Radiochim. Acta, **101**, 5, 333-338 (2013).

[3] A. Majkowska-Philip et al., J. Inorg. Biochem., **105**, 2, 313- 320 (2011).

[4] D. Mueller *et al.*, Recent Results Cancer Res., 194:77-87 (2013).

[5] PET/CT scans performed and kindly provided by Prof. Dr. med. R.P. Baum, THERANOSTICS Center for Molecular Radiotherapy and Molecular Imaging (PET/CT).

^{47}Sc PRODUCTION DEVELOPMENT FROM ^{47}Ca AND ^{47}Ti FOR RADIOPHARMACEUTICAL APPLICATIONS

K. Domnanich (Univ. Bern & PSI), U. Köster (ILL), S. Haller, K. Siwowska, C. Müller, R. Schibli (ETHZ & PSI), A. Türler (Univ. Bern & PSI), N.P. van der Meulen (PSI)

^{47}Sc is a radionuclide of potential value for radioimmunotherapy. Together with its positron-emitting counterpart ^{43}Sc, it is known as a "matched pair", expressing the same chemical behaviour, but different physical properties, enabling the use of different Sc radionuclides for diagnostic and therapeutic purposes.

Tab. 1: Comparison of nuclear properties of ^{47}Sc and ^{177}Lu

	^{47}Sc	^{177}Lu
$t_{1/2}$	3.4 d	6.7 d
Eβ^-_{av} [keV]	162	134
Main γ-ray [keV]	159.4 (68.3%)	208.4 (11.0%)

Radionuclides with low-energy β-emission (E$_{max}$= 400-800 keV) and several days half- life are considered for targeted tumour therapy of small tumours and cancer metastases. The most promising is ^{177}Lu, but ^{47}Sc is considered as good alternative (Table 1). Moreover, the photon of 159.4 keV is optimal for medical SPECT/CT- imaging and could be useful for preliminary low-dose *in vivo* studies, such as antibody uptake in the tumour and radiation dose estimates. ^{47}Sc can be produced in two neutron-induced reactions: ^{47}Ti(n, p)^{47}Sc and ^{46}Ca(n,γ)^{47}Ca which decays with a half-life of 4.5 d to ^{47}Sc [1-3].

Reduction of Ti: *E*nriched Ti can only be purchased in oxide form; it was reduced prior to irradiation in collaboration with GSI, Darmstadt. Briefly, TiO$_2$, with 40% surplus CaH$_2$, were pressed into tablets and heated to 900 °C in Ar-atmosphere for 1 h. The coproduced CaO was dissolved with dilute acetic acid [4].

Irradiation. Ampoules with 0.4 and 0.2 mg ^{46}Ca (in ^{46}Ca(NO$_3$)$_2$ solution, enrichment 37.1%) were prepared and irradiated at the high flux reactor at the Institute Laue-Langevin (ILL), Grenoble, France, for about 24 hours at a neutron flux of 1.5*10^{15} n/cm^2*s. Up to 30 mg Ti were irradiated for several days (6-10 d) at the SINQ facility at PSI with a neutron flux of 4*10^{13} n/cm^2*s.

Chemical separation: *Separation of ^{47}Ca from ^{47}Sc*: After crushing the ampoule, the separation was performed according to the established procedure for ^{44}Sc (see: "Optimisation of ^{44}Sc Production by Cyclotron Irradiation of ^{44}Ca for Radiopharmaceutical Application"). The final product was obtained in 700 μL 4.8 M NaCl/0.13 M HCl solution, which was used for cell experiments and the recording of a SPECT-CT image of a tumour-bearing mouse.

Separation of Ti from ^{47}Sc: The initial experimental runs were performed using natural Ti. The separation was performed as described in "^{43}Sc Production Development by Cyclotron Irradiation of ^{43}Ca and ^{46}Ti".

Neutron irradiation of natural Ti yielded up to 3.5 MBq ^{47}Sc, however, about 3% ^{46}Sc was coproduced as an impurity. Other impurities were swiftly removed (Fig 1).
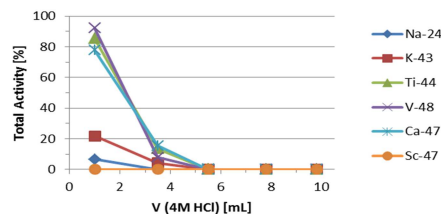
Fig. 1: Elution profile of the starting solution (4 M HCl) on the DGA column, showing that all the produced coproducts are eluted with the first few mL and Sc^{3+} was strongly retained by the resin.

Neutron irradiation of 0.2 mg ^{46}Ca activated up to 500 MBq ^{47}Ca, while 0.4 mg ^{46}Ca yielded nearly 1 GBq ^{47}Ca. ^{47}Ca and ^{47}Sc behave like a generator system, which made the separation of ^{47}Sc from Ca three times after ingrowth of ^{47}Sc possible. The maximum ^{47}Sc activity was reached after 135 h (5.6 days). The obtained ^{47}Sc was used for cell experiments and to record SPECT-CT images of tumour-bearing mice (Fig. 2).
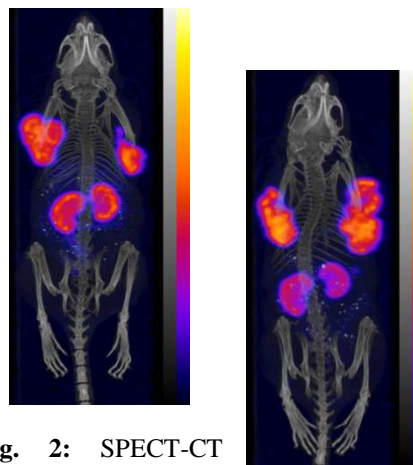
Fig. 2: SPECT-CT images of AR4J2 pancreatic tumour xenograft bearing mice after injection of 12 MBq ^{47}Sc-DOTANOC (left) and 40 MBq ^{177}Lu-DOTANOC (right).

[1] B. Bartos et al., Radiochim. Acta **100**, 457–461, (2012).

[2] L.F. Mausner et al., Appl. Radiat. Isot. **49**, 4, 285-294, (1998).

[3] C. Müller et al., J Nucl Med, **55**, 1658–1664, (2014).

[4] B. Lommel et al., J Radioanal Nucl Chem, **299**, 977 (2014).

THE NEW DCB-UNIBE RADIOPHARMACEUTICAL LABORATORY AT SWAN HOUSE (INSELSPITAL BERN)

J. Moreno, O. Leib, M. Bunka, T. Basaco (Univ. Bern), A. Türler (Univ. Bern & PSI)

Our work is related to all aspects of producing diagnostic and therapeutic radiopharmaceuticals under Good Manufacturing Practice (GMP) conditions. The work includes validation of production– and quality control (QC) methods, qualification of instrumentation, routine production of approved radiopharmaceuticals for clinical studies, as well as applied research for example related to the preparation of radioimmunoconjugates for radioimmunotherapy.

A view of the GMP production premises is shown in Fig. 1. This area has been designed, constructed and equipped with hot cells, glove boxes and associated instrumentation, which meets the highest requirements, set by both radiation protection and aseptic manufacturing regulations.

Fig. 1: GMP production area at DCB-UNIBE laboratory

The QC laboratory shown in Fig. 2 is equipped with an HPLC/TLC system coupled with UV and radiation detectors needed to determine the radiochemical and chemical purity of radiopharmaceuticals. In addition, a gas chromatography system is used to measure organic residues in the product. For the determination of the radionuclide purity in radiopharmaceuticals, a high resolution gamma-ray spectrometry system has been set up.

Fig. 2: QC Radiochemical Laboratory

In January 2014, this laboratory received the license from Swissmedic to produce somatostatin peptide analogues labelled with ^{68}Ga as radiotracer to image neuroendocrine tumors using Positron Emission Tomography coupled with Computer Tomography (PET/CT). This radiotracer allows obtaining a high degree of sensitivity, specificity, and diagnostic accuracy for gastroenteropancreatic neuroendocrine tumors. Within the frame of a clinical study called "GaIN", which has been coordinated by the Department of Nuclear Medicine at the Inselspital and SWAN, approximately 20 production batches of [^{68}Ga]-DOTATATE have been released for the diagnosis of patients during 2014.

Fig. 3 shows a PET/CT image of a patient diagnosed with [^{68}Ga]-DOTATATE (left) compared to the standard [^{111}In]-pentetreotide (right) Single-Photon Emission Computed Tomography scintigraphy (SPECT/CT) imaging. The picture on the left clearly reveals superior image resolution and allows detection of smaller lesions.

The production also covers the treatment of individual patients who have received a special authorization from Swissmedic for diagnosis and/or treatment. In this year 10 batches of [^{68}Ga]-DOTATATE have been released.
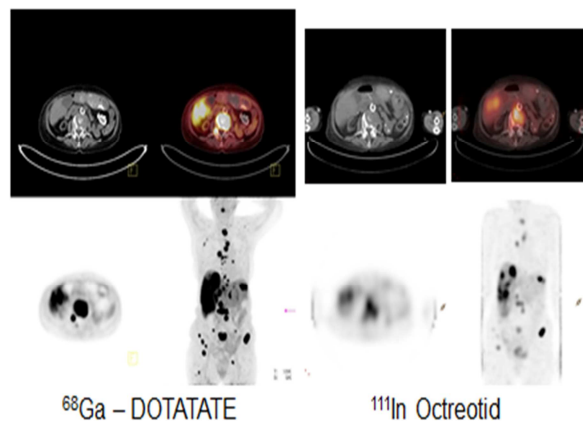
Fig. 3: Diagnostic accuracy of ^{68}Ga-DOTATATE PET/CT compared to standard ^{111}In-pentetreotide scintigraphy (SPECT/CT)*

In addition to the diagnostic agent [^{68}Ga]-DOTATATE, we have initiated validation work for the preparation of therapeutic radiopharmaceuticals based on beta emitting radionuclides ^{90}Y and ^{177}Lu.

_____

*   T. Krause, Nuklearmedizin Inselspital Bern, private communication.

ONLINE COUPLING OF PURE O$_2$ THERMO OPTICAL METHODS – ^{14}C AMS FOR CARBONACEOUS AEROSOLS SOURCE APPORTIONMENT STUDY

K. Agrios, M. Vonwiller (Univ. Bern & PSI), Y.-L. Zhang (Univ. Bern & PSI, Yale-NUIST),
V. G. Ciobanu (PSI/LAC), M. Battaglia, M. Luginbühl, G. Salazar, S. Szidat (Univ. Bern)

We report here on novel analytical techniques for sample preparation and direct determination of ^{14}C in organic carbon (OC) and elemental carbon (EC), two sub-fractions of total carbon (TC) of atmospheric air particulate matter. ^{14}C is an important tool in separating fossil from non-fossil sources providing unique information of carbonaceous aerosols source apportionment [1]. Until recently, separation of OC and EC has been performed offline by manual and time-consuming techniques [2, 3]. We present here two online hyphenated techniques between a Sunset OC/EC analyzer using pure O$_2$ as carrier gas and the MICA-DAS accelerator mass spectrometer (AMS) equipped with a gas ion source [4]. We demonstrate that it is feasible to bypass manual cryogenic CO$_2$ trapping into ampoules (offline trapping) for the measurement of real atmospheric samples (trapping online method, Fig. 1). In this approach, the CO$_2$ is collected in a zeolite trap at room temperature and then released by heating first into a gas-tight syringe and then injected steadily in the ion source mixed with He. Figure 2 compares the trapping online method with the offline trapping yielding good agreement for OC and EC samples.

Additionally, for a first series of reference materials analysis, CO$_2$ gas is directly fed into the ion source without using intermediate enrichment steps. This way we can benefit from a real-time injection avoiding the averaging of ^{14}C signal over large trapped CO$_2$ fractions. Combustion gases are scrubbed free from O$_2$ via the reaction $2Cu + O_2 \rightarrow 2CuO$ by a Cu reactor heated at 580 ºC (Fig. 3) so that only the tolerable gases are transmitted to the ion source. The system is reliable for some fast injections of CO$_2$ gas that resulted in relatively high ^{12}C$^+$ currents (Fig. 4).

Fig. 1: Schematic of the OC/EC analyser coupled to the gas introduction system (GIS) for the MICADAS gas ion source at University of Bern.
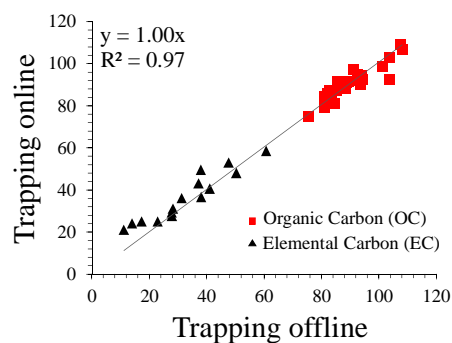
Fig. 2: Comparison of ^{14}C measurement of OC and EC using the offline and trapping online methods with aerosol samples from Switzerland [5].
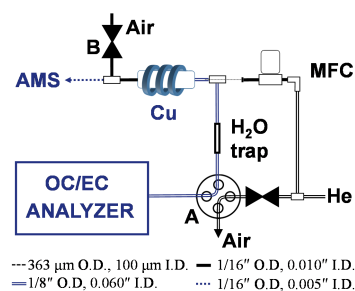
Fig. 3: The technical scheme for continuous-flow ^{14}C measurements. Valve A is shown in the configuration for ^{14}C measurement of CO$_2$.
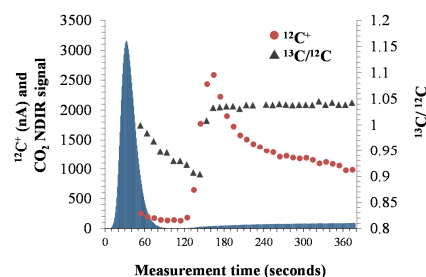
Fig. 4: Continuous-flow ^{14}C measurement of NIST-HOx2. The respective IR trace for total carbon combustion is overlaid with the ^{12}C$^+$ current and the ^{13}C/^{12}C ratio.

[1] S. Szidat, Chimia, 2009, **63**, 157 (2009).
[2] S. Szidat et al., Nucl. Instr. Meth. Phys. Res. B, **223-224**, 829 (2004).
[3] M. Ruff et al., Radiocarbon, **49**, 307 (2007).
[4] S. Szidat et al., Radiocarbon, **56**, 561 (2014).
[5] P. Zotter et al., Atmos. Chem. Phys., in press (2014).

SOURCE APPORTIONMENT USING RADIOCARBON AND ORGANIC TRACERS FOR PM$_{2.5}$ CARBONACEOUS AEROSOLS IN GUANGZHOU, SOUTH CHINA

J.-W. Liu (CAS-GIG, Univ. Bern), J. Li, G. Zhang (CAS-GIG), Y.-L. Zhang (Univ. Bern & PSI), S. Szidat (Univ. Bern)

The haze period in China in winter 2012/2013 with high loading of air-borne particulate matter initiated a debate about effective measures for air quality improvement [1]. In order to study the influence from local emissions and accumulation of aerosols from regional sources, we analysed radiocarbon (^{14}C) in Guangzhou, China [2]. During eight episodes of normal and haze conditions (Fig. 1), we observed two different trends of the fraction of modern carbon (f_m) of elemental carbon (EC), which differentiates fossil (EC$_f$, $f_m = 0$) and biomass-burning EC (EC$_{bb}$, $f_m = 1.1$).

- Episodes GIG02 and GIG08 show the highest PM$_{2.5}$ concentrations. They are influenced from local sources as indicated from air-mass back trajectory and wind speed analysis. Compared to the other samples, these two haze samples were impacted by fossil emissions (lowest f_m(EC) values) mainly from traffic exhaust.

- Episodes GIG06 and GIG07 also represent haze conditions, but these were caused by accumulation of aerosols from regional sources. f_m(EC) values and levoglucosan measurements indicate emissions from biomass burning.
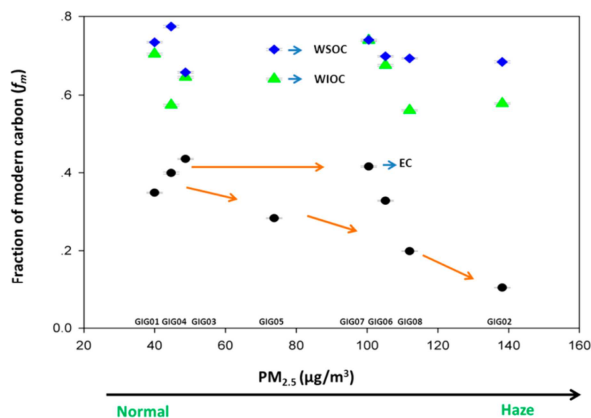
Fig. 1: Fraction of modern carbon versus PM$_{2.5}$ concentrations for elemental carbon (EC), water-soluble organic carbon (WSOC) and water-insoluble organic carbon (WIOC) from Guangzhou during eight episodes (GIG01-08) in winter 2012/2013 [2].

Figure 2 presents the complete source apportionment based on ^{14}C measurements of EC, water-soluble organic carbon (WSOC) and water-insoluble organic carbon (WIOC). In contrast to EC, the non-fossil (nf) fractions of WSOC and WIOC may include other sources than biomass burning, especially secondary organic aerosols (SOA) from biogenic precursor gases. Figure 2 displays, how the visibility was reduced in Guangzhou during the haze days. The source apportionment changes substantially from December 18 (episode GIG01) to December 20 (episode GIG02). The relative contributions of the fossil fractions EC$_f$, WIOC$_f$ and WSOC$_f$ increased on the average by a factor of 2, whereas mainly WSOC$_{nf}$ decreases. As mentioned above, episode GIG02 was impacted from local sources.
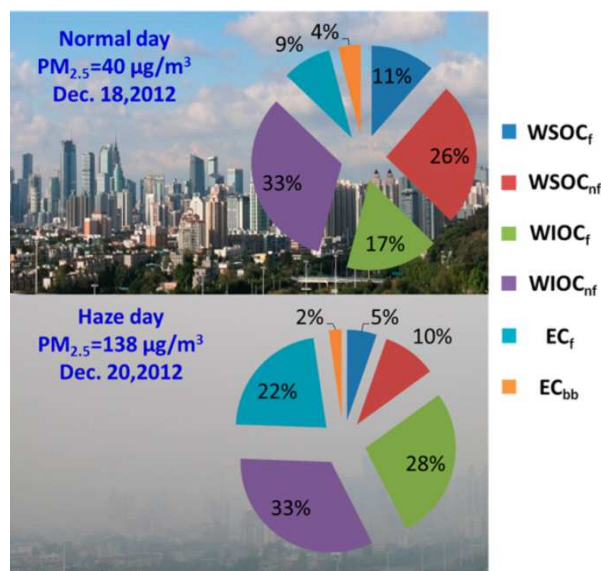
Fig. 2: Complete source apportionment based on ^{14}C measurements of EC, WSOC and WIOC for December 18 (episode GIG01) and December 20, 2012 (episode GIG02) [2].

_____

[1] R.-J. Huang et al., Nature, **514**, 218 (2014).
[2] J.-W. Liu et al., Environ. Sci. Technol, **48**, 12002 (2014).

COUPLING OF AN ELEMENTAL ANALYZER WITH AMS FOR FAST ^{14}C ANALYSIS OF AEROSOL SAMPLES

G. Salazar (Univ. Bern), Y.L. Zhang (Univ. Bern & PSI, Yale-NUIST), K. Agrios (Univ. Bern & PSI), S. Szidat (Univ. Bern)

^{14}C analysis by Accelerator Mass Spectrometry (AMS) helps to apportion the origin of aerosols between wood burning, biogenic emission or fossil-fuel combustion. However, aerosol sample preparation is highly effort and time consuming (1 hr/sample) [1, 2]. This report describes two types of online couplings of an elemental analyzer (EA) with AMS for the fast analysis of the total carbon (TC) from aerosol samples. The CO_2 trapping coupling is based on a method of a previous study [3] and the real-time coupling is based on a gas interface developed by our laboratory.

Samples are oxidized in the EA and the CO_2 is transferred into a Gas Interface System (GIS) that traps the gas and slowly injects the CO_2 into the ion source of the AMS (Fig 1). Constant contamination is studied by consecutively injecting the same radiocarbon standard (NIST oxalic acid 2, 134.066 pMC; IAEA C7, 49.53 pMC; Merck fossil sodium acetate, 0 pMC) to eliminate cross contamination. For the cross contamination, injections of oxalic acid and fossil standards are alternated. For the real-time coupling (Fig 3), two flow separators are used to extract the high load of carrier gas from the CO_2 that is being injected and proof-of-principle data are shown for this coupling.
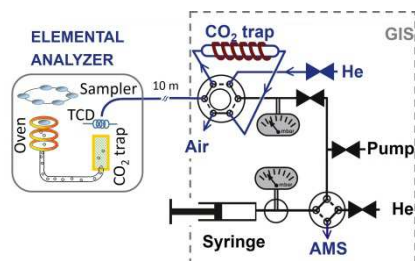
Fig. 1: Illustration of the CO_2 trapping coupling.

The equation of the contamination model is:

$$drift = m_k/m_s \, (R_k\text{-}R_s) + \phi m_x/m_s \, (R_x\text{-}R_s) \text{ (Eq. 1)}.$$

The results for constant contamination are presented in Fig. 2a-c. At low carbon masses, the measured ratio drifts away from the nominal value due to the radiocarbon content of the contaminant. The non-linear least squares fitting of Eq. 1 gives $m_k = 1.4\pm0.2$ µg and $R_k = 70\pm7$ pMC. For the cross contamination, the ϕ factor is $(0.2\pm0.1)\%$ (Fig. 2d). The contamination is corrected from the measurement by the following mass balance equation:

$$R'_m = (m_sR_m \text{-} m_kR_k \text{-} \phi m_xR_x) \, / \, (m_s\text{-}m_k\text{-}\phi m_x) \text{ (Eq. 2)}.$$

The typical uncertainty range for the corrected value is 1.5% to 5%.
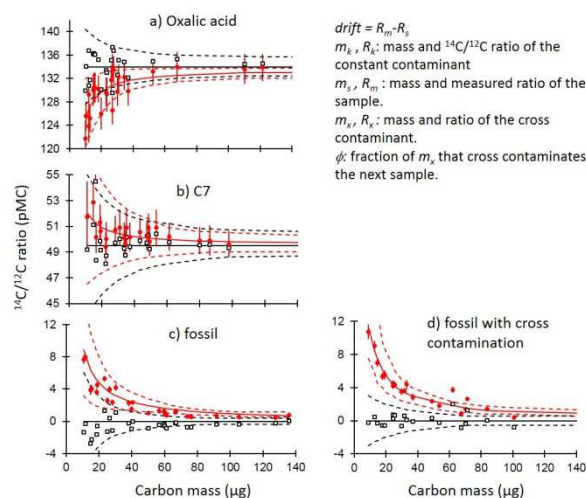
Fig. 2: Contamination model. The red line represents the drift model ($r^2 = 0.84$) with 1σ confidence bands. Black opened squares show the corrected R_m with confidence bands and the nominal value.
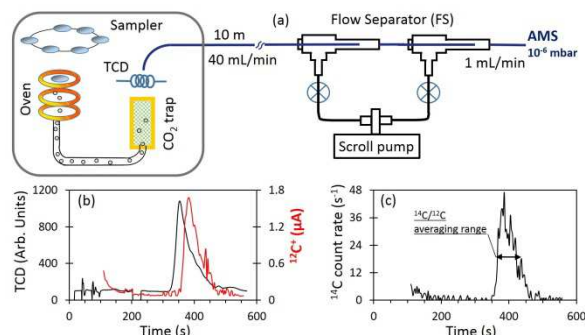
Fig. 3: a) Schematic of the real-time coupling of the EA with AMS. b) and c) Typical signals at 50 µg C.

The ^{12}C$^+$ and ^{14}C signals present chromatography-like peaks and the uncertainty of their ratio ranges from 5-7% for C7. These results show the potential application for fast ^{14}C measurement and for coupling other analytical techniques with AMS instruments. The real-time online method looks promising for even faster analysis or for tracing or surveying the ^{14}C of the sample.

[1] S. Szidat et al., Nucl. Instr. and Meth. Phys. Res. B, **223-224**, 829 (2004).
[2] S. M. Fahrni et al., Nucl. Instr. and Meth. Phys. Res. B, **268**, 787 (2010).
[3] L. Wacker et al., Nucl. Instr. and Meth. Phys. Res. B, **294**, 315 (2013).

FOSSIL VS. NON-FOSSIL SOURCES OF FINE CARBONACEOUS AEROSOLS IN FOUR CHINESE CITIES DURING THE EXTREME WINTER HAZE EPISODE IN 2013

Y.L. Zhang (Univ. Bern & PSI, Yale-NUIST), R. Huang, I. El Haddad, P. Zotter, C. Bozzetti, A.S.H. Prévôt (PSI-LAC), J. Schnelle-Kreis (HZ München), J.-J. Cao (CAS-IEE), M. Schwikowski (PSI), G. Salazar, S. Szidat (Univ. Bern)

During January 2013, the severe problem of air pollution in China became a worldwide concern, as extremely high concentrations of $PM_{2.5}$ were reported [1]. To investigate sources and formation mechanisms of fine carbonaceous aerosols from this high pollution episode across China, an intensive field experiment was carried out in the four large cities Xian, Beijing, Shanghai and Guangzhou. These measurements were used in conjunction with an effective statistical approach, Latin-hypercube sampling (LHS) [2] of a combined dataset from elemental carbon (EC) and organic carbon (OC), radiocarbon (^{14}C), to elucidate the origins of the carbonaceous aerosol during the haze event as well as the importance of primary and secondary formation of OC.

Figure 1 shows the concentrations of $PM_{2.5}$, OC and EC as well as EC to OC ratios (EC/OC) in the four Chinese cities. The average PM2.5 mass concentrations at the Xian, Beijing, Shanghai, and Guangzhou sampling sites during the sampling periods were 345 ± 125 μg m^{-3}, 158 ± 81 μg m^{-3}, 90 ± 31 μg m^{-3}, and 68 ± 23 μg m^{-3}, respectively. OC and EC concentrations showed similar spatial distributions as the $PM_{2.5}$ mass in the same order of the four cities. The EC/OC ratios were comparable for Xian, Shanghai and Guangzhou, but considerably lower at Beijing.

Six filters were selected per sampling site for ^{14}C analysis, three from days with a very high PM loading and three representing an average loading. A thermo-optical OC/EC analyzer was used for the isolation of different carbon fractions for subsequent ^{14}C measurements using a four-step thermo-optical protocol Swiss_4S [3]. Source apportionment results are obtained by LHS using the dataset from measured OC, EC, and levoglucosan mass concentrations, estimated emission ratios as well as ^{14}C contents of OC and EC [4].

Figure 2 shows concentrations of EC from fossil and biomass-burning emissions (EC_f and EC_{bb}, respectively, fossil OC from primary and secondary formation ($OC_{pri,f}$ and $OC_{sec,f}$, respectively), primary OC from biomass burning (OC_{bb}) and other non-fossil OC ($OC_{other,nf}$) including secondary non-fossil OC for moderately and heavily polluted days as well as the difference of these two as the pollution excess. Although secondary OC (i.e. $OC_{sec,f}$ and the majority of $OC_{other,nf}$) was already considerable for moderately polluted days, its contribution even increased by 70% on the average for the heavily polluted days. This underlines that the episodes with bad air quality were mainly caused by additional SOC formation and accumulation of similar pollutants as for average winter conditions.

Fig. 1: Whisker-box plots of mass concentrations (a), OC (b) and EC (c) as well as EC/OC ratios (d) for Xian (XA), Beijing (BJ), Shanghai (SH) and Guangzhou (GZ) during winter of 2013 [4].
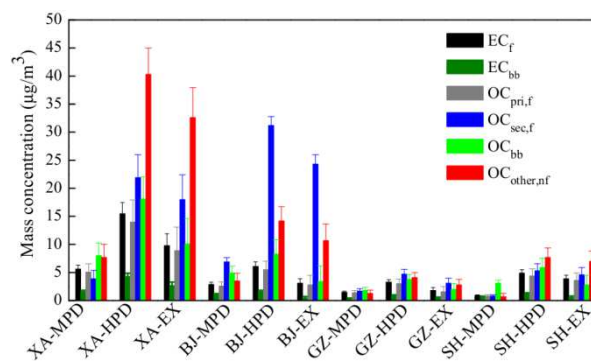
Fig. 2: Average mass concentrations of OC and EC from different sources (see text) during moderately polluted days (MPD), heavily polluted days (HPD) and their corresponding excess (EX = HPD–MPD) [4].

[1] R.-J. Huang et al., Nature, **514**, 218 (2014).
[2] A. Gelencsér et al., J. Geophys. Res., **112**, D23S04, (2007).
[3] Y.-L. Zhang et al., Atmos. Chem. Phys., **12**, 10841 (2012).
[4] Y.-L. Zhang et al., Atmos. Chem. Phys. Discuss., **14**, 26257 (2014).

LIST OF PUBLICATIONS

Heavy Elements

Y. Demidov, A. Zaitsevskii, R. Eichler
First principles based modeling of the adsorption of atoms of element 120 on a gold surface
Phys. Chem. Chem. Phys. **16** (6): 2268-2270, doi: 10.1039/C3CP54485K (2014).

R. Eichler
Superheavy element chemistry
Nuclear Physics: Present and Future, Greiner, W. (Editor), Springer International Publishing. p. 33-43, doi: 10.1007/978-3-319-10199-6_4 (2014).

R. Eichler, B. Eichler
Thermochemical data from gas-phase adsorption and methods of their estimation
The Chemistry of Superheavy Elements, Schädel, M. and Shaughnessy, D. (Editors). Springer Berlin Heidelberg. p. 375-413, doi: 10.1007/978-3-642-37466-1_7 (2014).

J. Even, A. Yakushev, C. E. Düllmann, J. Dvorak, R. Eichler, O. Gothe, W. Hartmann, D. Hild, E. Jäger, J. Khuyagbaatar, B. Kindler, J. V. Kratz, J. Krier, B. Lommel, L. Niewisch, H. Nitsche, I. Pysmenetska, M. Schädel, B. Schausten, A. Türler, N. Wiehl, D. Wittwer
In-situ formation, thermal decomposition, and adsorption studies of transition metal carbonyl complexes with short-lived radioisotopes
Radiochim. Acta **102** (12): 1093–1110, doi: 10.1515/ract-2013-2198 (2014).

J. Even, A. Yakushev, C. E. Düllmann, H. Haba, M. Asai, T. K. Sato, H. Brand, A. Di Nitto, R. Eichler, F. L. Fan, W. Hartmann, M. Huang, E. Jäger, D. Kaji, J. Kanaya, Y. Kaneya, J. Khuyagbaatar, B. Kindler, J. V. Kratz, J. Krier, Y. Kudou, N. Kurz, B. Lommel, S. Miyashita, K. Morimoto, K. Morita, M. Murakami, Y. Nagame, H. Nitsche, K. Ooe, Z. Qin, M. Schädel, J. Steiner, T. Sumita, M. Takeyama, K. Tanaka, A. Toyoshima, K. Tsukada, A. Türler, I. Usoltsev, Y. Wakabayashi, Y. Wang, N. Wiehl, S. Yamaki
Synthesis and detection of a seaborgium carbonyl complex
Science **345** (6203): 1491-1493, doi: 10.1126/science.1255720 (2014).

H. W. Gäggeler
Nucleon transfer reactions in very heavy ion systems
Nuclear Physics: Present and Future Greiner, W. (Editor), Springer International Publishing. p. 45-53, doi: 10.1007/978-3-319-10199-6_5 (2014).

H. W. Gäggeler, A. Türler
Gas-phase chemistry of superheavy elements
The Chemistry of Superheavy Elements, Schädel, M. and Shaughnessy, D. (Editors). Springer Berlin Heidelberg. p. 415-483, doi: 10.1007/978-3-642-37466-1_8 (2014).

J. Khuyagbaatar, A. Yakushev, C. E. Düllmann, D. Ackermann, L. L. Andersson, M. Asai, M. Block, R. A. Boll, H. Brand, D. M. Cox, M. Dasgupta, X. Derkx, A. Di Nitto, K. Eberhardt, J. Even, M. Evers, C. Fahlander, U. Forsberg, J. M. Gates, N. Gharibyan, P. Golubev, K. E. Gregorich, J. H. Hamilton, W. Hartmann, R. D. Herzberg, F. P. Heßberger, D. J. Hinde, J. Hoffmann, R. Hollinger, A. Hübner, E. Jäger, B. Kindler, J. V. Kratz, J. Krier, N. Kurz, M. Laatiaoui, S. Lahiri, R. Lang, B. Lommel, M. Maiti, K. Miernik, S. Minami, A. Mistry, C. Mokry, H. Nitsche, J. P. Omtvedt, G. K. Pang, P. Papadakis, D. Renisch, J. Roberto, D. Rudolph, J. Runke, K. P. Rykaczewski, L. G. Sarmiento, M. Schädel, B. Schausten, A. Semchenkov, D. A. Shaughnessy, P. Steinegger, J. Steiner, E. E. Tereshatov, P. Thörle-Pospiech, K. Tinschert, T. Torres De Heidenreich, N. Trautmann, A. Türler, J. Uusitalo, D. E. Ward, M. Wegrzecki, N. Wiehl, S. M. Van Cleve, V. Yakusheva
$^{48}Ca+^{249}Bk$ fusion reaction leading to element $z=117$: Long-lived α-decaying ^{270}Db and discovery of ^{266}Lr
Phys. Rev. Lett. **112** (17): 172501, doi: 10.1103/PhysRevLett.112.172501 (2014).

K. Nishio, H. Ikezoe, S. Hofmann, F. P. Heßberger, D. Ackermann, S. Antalic, Y. Aritomo, V. F. Comas, C. E. Düllman, A. Gorshkov, R. Graeger, S. Heinz, J. A. Heredia, K. Hirose, J. Khuyagbaatar, B. Kindler, I. Kojouharov, B. Lommel, H. Makii, R. Mann, S. Mitsuoka, Y. Nagame, I. Nishinaka, T. Ohtsuki, A. G. Popeko, S. Saro, M. Schädel, A. Türler, Y. Wakabayashi, Y. Watanabe, A. Yakushev, A. V. Yeremin
Study of heavy-ion induced fission for heavy-element synthesis
EPJ Web of Conferences **66:** 03065, doi: 10.1051/epjconf/20146603065 (2014).

K. Nishio, H. Ikezoe, S. Hofmann, D. Ackermann, Y. Aritomo, V.F. Comas, Ch.E. Düllmann, S. Heinz, J.A. Heredia, F.P. Heßberger, K. Hirose, J. Khuyagbaatar, B. Kindler, I. Kojouharov, B. Lommel, M. Makii, R. Mann, S. Mitsuoka, I. Nishinaka, T. Ohtsuki, S. Saro, M. Schädel, A.G. Popeko, A. Türler, Y. Wakabayashi, Y. Watanabe, A. Yakushev, A. Yeremin
Study of Heavy-ion Induced Fission for Heavy Element Synthesis
Nucl. Data Sheets **119**: 299-302, doi: 10.1016/j.nds.2014.08.082 (2014).

V. Pershina, A. Borschevsky, M. Iliaš, A. Türler
Theoretical predictions of properties and volatility of chlorides and oxychlorides of group-4 elements. II. Adsorption of tetrachlorides and oxydichlorides of Zr, Hf, and Rf on neutral and modified surfaces
The J. Chem. Phys. **141** (6): 064315, doi: 10.1063/1.4891531 (2014).

D. Rudolph, U. Forsberg, P. Golubev, L. G. Sarmiento, A. Yakushev, L. L. Andersson, A. Di Nitto, C. E. Düllmann, J. M. Gates, K. E. Gregorich, C. J. Gross, R. D. Herzberg, F. P. Heßberger, J. Khuyagbaatar, J. V. Kratz, K. Rykaczewski, M. Schädel, S. Åberg, D. Ackermann, M. Block, H. Brand, B. G. Carlsson, D. Cox, X. Derkx, K. Eberhardt, J. Even, C. Fahlander, J. Gerl, E. Jäger, B. Kindler, J. Krier, I. Kojouharov, N. Kurz, B. Lommel, A. Mistry, C. Mokry, H. Nitsche, J. P. Omtvedt, P. Papadakis, I. Ragnarsson, J. Runke, H. Schaffner, B. Schausten, P. Thörle-Pospiech, T. Torres, T. Traut, N. Trautmann, A. Türler, A. Ward, D. E. Ward, N. Wiehl
Alpha-photon coincidence spectroscopy along element 115 decay chains
Acta Phys. Pol., B **45** (2): 263-272, doi: 10.5506/APhysPolB.45.263 (2014).

A. Türler, K. Gregorich
Experimental techniques
The Chemistry of Superheavy Elements, Schädel, M. and Shaughnessy, D. (Editors). Springer Berlin Heidelberg. p. 261-308, doi: 10.1007/978-3-642-37466-1_5 (2014).

I. Usoltsev, R. Eichler, G. K. Vostokin, A. V. Sabel'nikov, N. V. Aksenov, Y. V. Albin, G. A. Bozhikov, V. I. Chepigin, S. N. Dmitriev, V. Y. Lebedev, O. N. Malyshev, O. V. Petrushkin, D. Piguet, G. Y. Starodub, A. I. Svirikhin, A. Türler, A. V. Yeremin
Preparation and high intensity heavy ion irradiation tests of intermetallic $^{243}Am/Pd$ targets
Nucl. Instrum. Methods Phys. Res., Sect. B **318**: 297-305, doi: 10.1016/j.nimb.2013.10.019 (2014).

Y. Wang, Z. Qin, F.-L. Fan, F.-Y. Fan, S,-W. Cao, X.-L. Wu, X. Zhang, J. Bai, X.-J. Yin, L.-L. Tian. L. Zhao, W. Tian, Z. Li, C.-M. Tan, J.-S. Guo, H.W. Gäggeler
Gas-phase chemistry of Mo, Ru, W, and Os metal carbonyl complexes
Radiochim. Acta, **102** (1,2) 69-76, doi: 10.1515/ract-2014-2157 (2014).

A. Yakushev, J. M. Gates, A. Türler, M. Schädel, C. E. Düllmann, D. Ackermann, L.-L. Andersson, M. Block, W. Brüchle, J. Dvorak, K. Eberhardt, H. G. Essel, J. Even, U. Forsberg, A. Gorshkov, R. Graeger, K. E. Gregorich, W. Hartmann, R.-D. Herzberg, F. P. Heßberger, D. Hild, A. Hübner, E. Jäger, J. Khuyagbaatar, B. Kindler, J. V. Kratz, J. Krier, N. Kurz, B. Lommel, L. J. Niewisch, H. Nitsche, J. P. Omtvedt, E. Parr, Z. Qin, D. Rudolph, J. Runke, B. Schausten, E. Schimpf, A. Semchenkov, J. Steiner, P. Thörle-Pospiech, J. Uusitalo, M. Wegrzecki, N. Wiehl
Superheavy element flerovium (element 114) is a volatile metal
Inorg. Chem. **53** (3): 1624-1629, doi: 10.1021/ic4026766 (2014).

SURFACE CHEMISTRY

T. Bartels-Rausch, H. W. Jacobi, T. F. Kahan, J. L. Thomas, E. S. Thomson, J. P. D. Abbatt, M. Ammann, J. R. Blackford, H. Bluhm, C. Boxe, F. Domine, M. M. Frey, I. Gladich, M. I. Guzmán, D. Heger, T. Huthwelker, P. Klán, W. F. Kuhs, M. H. Kuo, S. Maus, S. G. Moussa, V. F. McNeill, J. T. Newberg, J. B. C. Pettersson, M. Roeselová, J. R. Sodeau
A review of air – ice chemical and physical interactions (AICI): liquids, quasi-liquids, and solids in snow
Atmos. Chem. Phys. **14** (3): 1587-1633, doi: 10.5194/acp-14-1587-2014 (2014).

C. George, B. D'Anna, H. Herrmann, C. Weller, V. Vaida, D. J. Donaldson, T. Bartels-Rausch, M. Ammann
Emerging areas in atmospheric photochemistry
Topics in Current Chemistry: Atmospheric Chemistry (**399**), Ariya, P. A. (Editor), Springer: Berlin Heidelberg. p. 1-53, doi: 10.1007/128_2012_393 (2014).

G. Gržinić, T. Bartels-Rausch, M. Birrer, A. Türler, M. Ammann
*Production and use of ^{13}N labeled N_2O_5 to determine gas – aerosol interaction kinetics*Radiochim. Acta **102** (11): 1025-1034, doi: 10.1515/ract-2014-2244 (2014).

M. Legrand, S. Preunkert, M. Frey, T. Bartels-Rausch, A. Kukui, M. D. King, J. Savarino, M. Kerbrat, B. Jourdain
Large mixing ratios of atmospheric nitrous acid (HONO) at Concordia (East Antarctic Plateau) in summer: A strong source from surface snow?
Atmos. Chem. Phys. **14** (18): 9963-9976, doi: 10.5194/acp-14-9963-2014 (2014).

J. G. Pruyne, M.-T. Lee, C. Fábri, A. Beloqui Redondo, A. Kleibert, M. Ammann, M. A. Brown, M. J. Krisch
Liquid–vapor interface of formic acid solutions in salt water: A comparison of macroscopic surface tension and microscopic in situ X-ray photoelectron spectroscopy measurements
J. Phys. Chem. C: **118**(50): 29350-29360, doi: 10.1021/jp5056039 (2014).

S. S. Steimer, M. Lampimäki, E. Coz, G. Grzinic, M. Ammann
The influence of physical state on shikimic acid ozonolysis: A case for in situ microspectroscopy
Atmos. Chem. Phys. **14** (19): 10761-10772, doi: 10.5194/acp-14-10761-2014 (2014).

ANALYTICAL CHEMISTRY

A. Eichler, L. Tobler, S. Eyrikh, N. Malygina, T. Papina, M. Schwikowski
Ice-core based assessment of historical anthropogenic heavy metal (Cd, Cu, Sb, Zn) emissions in the Soviet Union
Environ. Sci. Technol. **48** (5): 2635-42, doi: 10.1021/es404861n (2014).

S. Kaspari, T. H. Painter, M. Gysel, S. M. Skiles, M. Schwikowski
Seasonal and elevational variations of black carbon and dust in snow and ice in the Solu-Khumbu, Nepal and estimated radiative forcings
Atmos. Chem. Phys. **14** (15): 8089-8103, doi: 10.5194/acp-14-8089-2014 (2014).

I. Mariani, A. Eichler, T. M. Jenk, S. Brönnimann, R. Auchmann, M. C. Leuenberger, M. Schwikowski
Temperature and precipitation signal in two Alpine ice cores over the period 1961-2001
Clim. Past **10** (3): 1093-1108, doi: 10.5194/cp-10-1093-2014 (2014).

C. Mayer, A. Lambrecht, H. Oerter, M. Schwikowski, E. Vuillermoz, N. Frank, G. Diolaiuti
Accumulation studies at a high elevation glacier site in central Karakoram
Adv. Meteorol. **2014**: 1-12, doi: 10.1155/2014/215162 (2014).

C. Müller-Tautges, A. Eichler, M. Schwikowski, T. Hoffmann
A new sensitive method for the quantification of glyoxal and methylglyoxal in snow and ice by stir bar sorptive extraction and liquid desorption-HPLC-ESI-MS
Anal. Bioanal. Chem. **406** (11): 1-8, doi: 10.1007/s00216-014-7640-z (2014).

P. A. Pavlova, P. Schmid, C. Bogdal, C. Steinlin, T. M. Jenk, M. Schwikowski
Polychlorinated biphenyls in glaciers. 1. Deposition history from an Alpine ice core
Environ. Sci. Technol. **48** (14): 7842-8, doi: 10.1021/es5017922 (2014).

P. A. Pavlova, P. Schmid, M. Zennegg, C. Bogdal, M. Schwikowski
Trace analysis of hydrophobic micropollutants in aqueous samples using capillary traps
Chemosphere **106**: 51-56, doi: 10.1016/j.chemosphere.2013.12.092 (2014).

M. Schwikowski, T. M. Jenk, D. Stampfli, F. Stampfli
A new thermal drilling system for high-altitude or temperate glaciers
Ann. Glaciol. **55** (68): 131-136, doi: 10.3189/2014AoG68A024 (2014).

M. Schwikowski, A. Eichler, T.M. Jenk, I. Mariani
Annually resolved climate signals in high-alpine ice cores
Past Global Changes Magazine Vol. 22 (1), 28-29 (2014).

C. Steinlin, C. Bogdal, M. Scheringer, P. A. Pavlova, M. Schwikowski, P. Schmid, K. Hungerbühler
Polychlorinated biphenyls in glaciers. 2. Model results of deposition and incorporation processes
Environ. Sci. Technol. **48** (14): 7849-57, doi: 10.1021/es501793h (2014).

C. Wang, S. Hou, H. Pang, Y. Liu, H. W. Gäggeler, L. Tobler, S. Szidat, E. Vogel
^{210}Pb dating of the Miaoergou ice core from the eastern Tien Shan, China
Ann. Glaciol. **55** (66): 105 -110, doi: 10.3189/2014AoG66A151 (2014).

I. A. Wendl, J. A. Menking, R. Färber, M. Gysel, S. D. Kaspari, M. J. G. Laborde, M. Schwikowski
Optimized method for black carbon analysis in ice and snow using the single particle soot photometer
Atmos. Meas. Tech. **7** (8): 2667-2681, doi: 10.5194/amt-7-2667-2014 (2014).

RADWASTE ANALYTICS

A. Aerts, S. Danaci, B. Gonzalez Prieto, J. Van den Bosch, J. Neuhausen
Evaporation of mercury impurity from liquid lead–bismuth eutectic
J. Nucl. Mater. **448** (1–3): 276-281, doi: 10.1016/j.jnucmat.2014.02.013 (2014).

T. Al-Abdullah, S. Akhmadaliev, M. Ayranov, D. Bemmerer, R. Dressler, Z. Elekes, N. Kivel, K. Schmidt, D. Schumann, M. Sobiella, T. Stowasser, M. P. Takács, K. Zuber
The feasibility of direct measurement of the ^{44}Ti(α, p)^{47}V and ^{40}Ca(α, p)^{43}Sc reactions in forward kinematics at astrophysically relevant temperatures
Eur Phys J A **50** (9): 1-9, doi: 10.1140/epja/i2014-14140-8 (2014).

J. Balibrea, E. Mendoza, D. Cano-Ott, C. Guerrero, E. Berthoumieux, S. Altstadt, J. Andrzejewski, L. Audouin, M. Barbagallo, V. Bécares, F. Bečvář, F. Belloni, J. Billowes, V. Boccone, D. Bosnar, M. Brugger, M. Calviani, F. Calviño, C. Carrapiço, F. Cerutti, E. Chiaveri, M. Chin, N. Colonna, G. Cortés, M. A. Cortés-Giraldo, M. Diakaki, C. Domingo-Pardo, I. Duran, R. Dressler, N. Dzysiuk, C. Eleftheriadis, A. Ferrari, K. Fraval, S. Ganesan, A. R. García, G. Giubrone, M. B. Gómez-Hornillos, I. F. Gonçalves, E. González-Romero, E. Griesmayer, F. Gunsing, P. Gurusamy, D. G. Jenkins, E. Jericha, Y. Kadi, F. Käppeler, D. Karadimos, T. Kawano, N. Kivel, P. Koehler, M. Kokkoris, G. Korschinek, M. Krtička, J. Kroll, C. Langer, C. Lampoudis, C. Lederer, H. Leeb, L. S. Leong, R. Losito, A. Manousos, J. Marganiec, T. Martínez, P. F. Mastinu, M. Mastromarco, C. Massimi, M. Meaze, A. Mengoni, P. M. Milazzo, F. Mingrone, M. Mirea, W. Mondelaers, C. Paradela, A. Pavlik, J. Perkowski, M. Pignatari, A. Plompen, J. Praena, J. M. Quesada, T. Rauscher, R. Reifarth, A. Riego, F. Roman, C. Rubbia, R. Sarmento, P. Schillebeeckx, S. Schmidt, D. Schumann, I. Stetcu, M. Sabaté, G. Tagliente, J. L. Tain, D. Tarrío, L. Tassan-Got, A. Tsinganis, S. Valenta, G. Vannini, V. Variale, P. Vaz, A. Ventura, R. Versaci, M. J. Vermeulen, V. Vlachoudis, R. Vlastou, A. Wallner, T. Ware, M. Weigand, C. Weiß, T. J. Wright, P. Žugec
Measurement of the neutron capture cross section of the fissile isotope ^{235}U with the CERN n_TOF total absorption calorimeter and a fission tagging based on micromegas detectors
Nucl. Data Sheets **119**: 10-13, doi: 10.1016/j.nds.2014.08.005 (2014).

M. Barbagallo, N. Colonna, M. J. Vermeulen, S. Altstadt, J. Andrzejewski, L. Audouin, V. Bécares, F. Bečvář, F. Belloni, E. Berthoumieux, J. Billowes, V. Boccone, D. Bosnar, M. Brugger, M. Calviani, F. Calviño, D. Cano-Ott, C. Carrapiço F. Cerutti, E. Chiaveri, M. Chin, G. Cortés, M. A. Cortés-Giraldo, M. Diakaki, C. Domingo-Pardo, I. Duran, R. Dressler, C. Eleftheriadis, A. Ferrari, K. Fraval, S. Ganesan, A. R. García, G. Giubrone, I. F. Gonçalves, E. González-Romero, E. Griesmayer, C. Guerrero, F. Gunsing, A. Hernández-Prieto, D. G. Jenkins, E. Jericha, Y. Kadi, F. Käppeler, D. Karadimos, N. Kivel, P. Koehler, M. Kokkoris, M. Krtička, J. Kroll, C. Lampoudis, C. Langer, E. Leal-Cidoncha, C. Lederer, H. Leeb, L. S. Leong, R. Losito, A. Mallick, A. Manousos, J. Marganiec, T. Martínez, C. Massimi, P. F. Mastinu, M. Mastromarco, E. Mendoza, A. Mengoni, P. M. Milazzo, F. Mingrone, M. Mirea, W. Mondalaers, C. Paradela, A. Pavlik, J. Perkowski, A. Plompen, J. Praena, J. M. Quesada, T. Rauscher, R. Reifarth, A. Riego, M. S. Robles, C. Rubbia, M. Sabaté-Gilarte, R. Sarmento, A. Saxena, P. Schillebeeckx, S. Schmidt, D. Schumann, G. Tagliente, J. L. Tain, D. Tarrío, L. Tassan-Got, A. Tsinganis, S. Valenta, G. Vannini, V. Variale, P. Vaz, A. Ventura, V. Vlachoudis, R. Vlastou, A. Wallner, T. Ware, M. Weigand, C. Weiß, T. Wright, P. Žugec
Capture cross section of ^{236}U: The n_TOF results
Nucl. Data Sheets **119**: 45-47, doi: 10.1016/j.nds.2014.08.014 (2014).

E. Chiaveri, S. Altstadt, J. Andrzejewski, L. Audouin, M. Barbagallo, V. Bécares, F. Bečvář, F. Belloni, E. Berthoumieux, J. Billowes, V. Boccone, D. Bosnar, M. Brugger, M. Calviani, F. Calviño, D. Cano-Ott, C. Carrapiço, F. Cerutti, M. Chin, N. Colonna, G. Cortés, M. A. Cortés-Giraldo, M. Diakaki, C. Domingo-Pardo, I. Duran, R. Dressler, N. Dzysiuk, C. Eleftheriadis, A. Ferrari, K. Fraval, S. Ganesan, A. R. García, G. Giubrone, M. B. Gómez-Hornillos, I. F. Gonçalves, E. González-Romero, E. Griesmayer, C. Guerrero, F. Gunsing, P. Gurusamy, A. Hernández-Prieto, D. G. Jenkins, E. Jericha, Y. Kadi, F. Käppeler, D. Karadimos, N. Kivel, P. Koehler, M. Kokkoris, M. Krtička, J. Kroll, C. Lampoudis, C. Langer, E. Leal-Cidoncha, C. Lederer, H. Leeb, L. S. Leong, R. Losito, A. Mallick, A. Manousos, J. Marganiec, T. Martínez, C. Massimi, P. F. Mastinu, M. Mastromarco, M. Meaze, E. Mendoza, A. Mengoni, P. M. Milazzo, F. Mingrone, M. Mirea, W. Mondalaers, C. Paradela, A. Pavlik, J. Perkowski, A. Plompen, J. Praena, J. M. Quesada, T. Rauscher, R. Reifarth, A. Riego, M. S. Robles, F. Roman, C. Rubbia, M. Sabaté-Gilarte, R. Sarmento, A. Saxena, P. Schillebeeckx, S. Schmidt, D. Schumann, G. Tagliente, J. L. Tain, D. Tarrío, L. Tassan-Got, A. Tsinganis, S. Valenta, G. Vannini, V. Variale, P. Vaz, A. Ventura, R. Versaci, M. J. Vermeulen, V. Vlachoudis, R. Vlastou, A. Wallner, T. Ware, M. Weigand, C. Weiss, T. Wright, P. Žugec
The CERN n_TOF facility: Neutron beams performances for cross section measurements
Nucl. Data Sheets **119**: 1-4, doi: 10.1016/j.nds.2014.08.003 (2014).

C.-Y. Chuang, P. H. Santschi, Y. Jiang, Y.-F. Ho, A. Quigg, L. Guo, M. Ayranov, D. Schumann
Important role of biomolecules from diatoms in the scavenging of particle-reactive radionuclides of thorium, protactinium, lead, polonium, and beryllium in the ocean: A case study with Phaeodactylum tricornutum
Limnol. Oceanogr. **59** (4): 1256-1266, doi: 10.4319/lo.2014.59.4.1256 (2014).

K. Fraval, F. Gunsing, S. Altstadt, J. Andrzejewski, L. Audouin, M. Barbagallo, V. Bécares, F. Bečvář, F. Belloni, E. Berthoumieux, J. Billowes, V. Boccone, D. Bosnar, M. Brugger, M. Calviani, F. Calviño, D. Cano-Ott, C. Carrapiço, F. Cerutti, E. Chiaveri, M. Chin, N. Colonna, G. Cortés, M. A. Cortés-Giraldo, M. Diakaki, C. Domingo-Pardo, I. Duran, R. Dressler, N. Dzysiuk, C. Eleftheriadis, A. Ferrari, S. Ganesan, A. R. García, G. Giubrone, M. B. Gómez-Hornillos, I. F. Gonçalves, E. González-Romero, E. Griesmayer, C. Guerrero, P. Gurusamy, A. Hernández-Prieto, D. G. Jenkins, E. Jericha, Y. Kadi, F. Käppeler, D. Karadimos, N. Kivel, P. Koehler, M. Kokkoris, M. Krtička, J. Kroll, C. Lampoudis, C. Langer, E. Leal-Cidoncha, C. Lederer, H. Leeb, L. S. Leong, R. Losito, A. Mallick, A. Manousos, J. Marganiec, T. Martínez, C. Massimi, P. F. Mastinu, M. Mastromarco, M. Meaze, E. Mendoza, A. Mengoni, P. M. Milazzo, F. Mingrone, M. Mirea, W. Mondalaers, C. Paradela, A. Pavlik, J. Perkowski, A. Plompen, J. Praena, J. M. Quesada, T. Rauscher, R. Reifarth, A. Riego, M. S. Robles, F. Roman, C. Rubbia, M. Sabaté-Gilarte, R. Sarmento, A. Saxena, P. Schillebeeckx, S. Schmidt, D. Schumann, G. Tagliente, J. L. Tain, D. Tarrío, L. Tassan-Got, A. Tsinganis, S. Valenta, G. Vannini, V. Variale, P. Vaz, A. Ventura, R. Versaci, M. J. Vermeulen, V. Vlachoudis, R. Vlastou, A. Wallner, T. Ware, M. Weigand, C. Weiß, T. Wright, P. Žugec
Measurement and analysis of the ^{241}Am (n,γ) cross section with liquid scintillator detectors using time-of-flight spectroscopy at the n_TOF facility at CERN
Phys. Rev. C **89** (4): 044609, doi: 10.1103/PhysRevC.89.044609 (2014).

G. Giubrone, C. Domingo-Pardo, J. L. Taín, C. Lederer, S. Altstadt, J. Andrzejewski, L. Audouin, M. Barbagallo, V. Bécares, F. Bečvář, F. Belloni, E. Berthoumieux, J. Billowes, V. Boccone, D. Bosnar, M. Brugger, M. Calviani, F. Calviño, D. Cano-Ott, C. Carrapiço, F. Cerutti, E. Chiaveri, M. Chin, N. Colonna, G. Cortés, M. A. Cortés-Giraldo, M. Diakaki, I. Duran, R. Dressler, N. Dzysiuk, C. Eleftheriadis, A. Ferrari, K. Fraval, S. Ganesan, A. R. García, M. B. Gómez-Hornillos, I. F. Gonçalves, E. González-Romero, E. Griesmayer, C. Guerrero, F. Gunsing, P. Gurusamy, D. G. Jenkins, E. Jericha, Y. Kadi, F. Käppeler, D. Karadimos, N. Kivel, P. Koehler, M. Kokkoris, G. Korschinek, M. Krtička, J. Kroll, C. Langer, H. Leeb, L. S. Leong, R. Losito, A. Manousos, C. Massimi, J. Marganiec, T. Martínez, P. F. Mastinu, M. Mastromarco, M. Meaze, E. Mendoza, A. Mengoni, P. M. Milazzo, F. Mingrone, M. Mirea, W. Mondelaers, C. Paradela, A. Pavlik, J. Perkowski, M. Pignatari, A. Plompen, J. Praena, J. M. Quesada, T. Rauscher, R. Reifhart, A. Riego, F. Roman, C. Rubbia, R. Sarmento, P. Schillebeeckx, S. Schmidt, D. Schumann, G. Tagliente, D. Tarrio, L. Tassan-Got, A. Tsinganis, S. Valenta, G. Vannini, V. Variale, P. Vaz, A. Ventura, R. Versaci, M. J. Vermeulen, V. Vlachoudis, R. Vlastou, A. Wallner, T. Ware, M. Weigand, C. Weiß, T. Wright, P. Žugec
Measurement of the ^{54,57}Fe(n,γ) cross section in the resolved resonance region at CERN n_TOF
Nucl. Data Sheets **119**: 117-120, doi: 10.1016/j.nds.2014.08.033 (2014).

B. Gonzalez Prieto, J. Van den Bosch, J.A. Martens, J. Neuhausen, A. Aerts
Equilibrium evaporation of trace polonium from liquid lead–bismuth eutectic at high temperature
J. Nucl. Mater. **450**(1-3): 299-303, doi:10.1016/j.jnucmat.2013.06.037 (2014).

B. Gonzalez Prieto, J. Lim, A. Marien, K. Rosseel, J.A. Martens, J. Van den Bosch, J. Neuhausen, A. Aerts
Non-uniform polonium distribution in lead-bismuth eutectic revealed by evaporation experiments
J. Radioanal. Nucl. Chem. **302** (1): 195-200, doi: 10.1007/s10967-014-3264-1 (2014).

B. Gonzalez Prieto, A. Marino, J. Lim, K. Rosseel, J. Martens, M. Rizzi, J. Neuhausen, J. Van den Bosch, A. Aerts
Use of the transpiration method to study polonium evaporation from liquid lead-bismuth eutectic at high temperature
Radiochim. Acta, **102** (12): 1083-1091, doi: 10.1515/ract-2014-2263 (2014).

C. Guerrero, S. Altstadt, J. Andrzejewski, L. Audouin, M. Barbagallo, V. Bécares, F. Bečvář, F. Belloni, E. Berthoumieux,
J. Billowes, V. Boccone, D. Bosnar, M. Brugger, M. Calviani, F. Calviño, D. Cano-Ott, C. Carrapiço, F. Cerutti,
E. Chiaveri, M. Chin, N. Colonna, G. Cortés, M. A. Cortés-Giraldo, M. Diakaki, C. Domingo-Pardo, I. Duran, R. Dressler,
N. Dzysiuk, C. Eleftheriadis, A. Ferrari, K. Fraval, S. Ganesan, A. R. García, G. Giubrone, M. B. Gómez-Hornillos,
I. F. Gonçalves, E. González-Romero, E. Griesmayer, F. Gunsing, P. Gurusamy, D. G. Jenkins, E. Jericha, Y. Kadi,
F. Käppeler, D. Karadimos, N. Kivel, P. Koehler, M. Kokkoris, G. Korschinek, M. Krtička, J. Kroll, C. Langer, C. Lederer,
H. Leeb, L. S. Leong, R. Losito, A. Manousos, J. Marganiec, T. Martínez, P. F. Mastinu, M. Mastromarco, C. Massimi,
M. Meaze, E. Mendoza, A. Mengoni, P. M. Milazzo, F. Mingrone, M. Mirea, W. Mondelaers, C. Paradela, A. Pavlik,
J. Perkowski, M. Pignatari, A. Plompen, J. Praena, J. M. Quesada, T. Rauscher, R. Reifarth, A. Riego, F. Roman,
C. Rubbia, R. Sarmento, P. Schillebeeckx, S. Schmidt, D. Schumann, G. Tagliente, J. L. Tain, D. Tarrío, L. Tassan-Got,
A. Tsinganis, S. Valenta, G. Vannini, V. Variale, P. Vaz, A. Ventura, R. Versaci, M. J. Vermeulen, V. Vlachoudis,
R. Vlastou, A. Wallner, T. Ware, M. Weigand, C. Weiß, T. J. Wright, P. Žugec
Investigation of neutron-induced reactions at n_TOF: An overview of the 2009–2012 experimental program
Nucl. Data Sheets **119**: 5-9, doi: 10.1016/j.nds.2014.08.004 (2014).

B. Hammer, J. Neuhausen, V. Boutellier, H. P. Linder, N. Shcherbina, M. Wohlmuther, A. Türler, D. Schumann
Analysis of the ^{207}Bi, ^{194}Hg/Au and ^{173}Lu distribution in the irradiated MEGAPIE target
J. Nucl. Mater. **450** (1-3): 278-286, doi: 10.1016/j.jnucmat.2013.09.016 (2014).

B. Hammer, D. Schumann, J. Neuhausen, M. Wohlmuther, A. Türler
Radiochemical determination of polonium in liquid metal spallation targets
Nucl. Data Sheets **119**: 280-283, doi: 10.1016/j.nds.2014.08.077 (2014).

C. Lederer, G. Giubrone, C. Massimi, P. Žugec, M. Barbagallo, N. Colonna, C. Domingo-Pardo, C. Guerrero, F. Gunsing,
F. Käppeler, J. L. Tain, S. Altstadt, J. Andrzejewski, L. Audouin, V. Bécares, F. Bečvář, F. Belloni, E. Berthoumieux,
J. Billowes, V. Boccone, D. Bosnar, M. Brugger, M. Calviani, F. Calviño, D. Cano-Ott, C. Carrapiço, F. Cerutti,
E. Chiaveri, M. Chin, G. Cortés, M. A. Cortés-Giraldo, M. Diakaki, I. Duran, R. Dressler, N. Dzysiuk, C. Eleftheriadis,
A. Ferrari, K. Fraval, S. Ganesan, A. R. García, M. B. Gómez-Hornillos, I. F. Gonçalves, E. González-Romero,
E. Griesmayer, P. Gurusamy, D. G. Jenkins, E. Jericha, Y. Kadi, D. Karadimos, N. Kivel, P. Koehler, M. Kokkoris,
G. Korschinek, M. Krtička, J. Kroll, C. Langer, H. Leeb, L. S. Leong, R. Losito, A. Manousos, J. Marganiec, T. Martínez,
P. F. Mastinu, M. Mastromarco, M. Meaze, E. Mendoza, A. Mengoni, P. M. Milazzo, F. Mingrone, M. Mirea,
W. Mondelaers, C. Paradela, A. Pavlik, J. Perkowski, M. Pignatari, A. Plompen, J. Praena, J. M. Quesada, T. Rauscher,
R. Reifarth, A. Riego, F. Roman, C. Rubbia, R. Sarmento, P. Schillebeeckx, S. Schmidt, D. Schumann, G. Tagliente,
D. Tarrío, L. Tassan-Got, A. Tsinganis, S. Valenta, G. Vannini, V. Variale, P. Vaz, A. Ventura, R. Versaci,
M. J. Vermeulen, V. Vlachoudis, R. Vlastou, A. Wallner, T. Ware, M. Weigand, C. Weiß, T. J. Wright
Neutron capture reactions on Fe and Ni isotopes for the astrophysical s-process
Nucl. Data Sheets **120**: 201-204, doi: 10.1016/j.nds.2014.07.046 (2014).

C. Lederer, C. Massimi, E. Berthoumieux, N. Colonna, R. Dressler, C. Guerrero, F. Gunsing, F. Käppeler, N. Kivel,
M. Pignatari, R. Reifarth, D. Schumann, A. Wallner, S. Altstadt, S. Andriamonje, J. Andrzejewski, L. Audouin,
M. Barbagallo, V. Bécares, F. Bečvář, F. Belloni, B. Berthier, J. Billowes, V. Boccone, D. Bosnar, M. Brugger,
M. Calviani, F. Calviño, D. Cano-Ott, C. Carrapiço, F. Cerutti, E. Chiaveri, M. Chin, G. Cortés, M. A. Cortés-Giraldo,
I. Dillmann, C. Domingo-Pardo, I. Duran, N. Dzysiuk, C. Eleftheriadis, M. Fernández-Ordóñez, A. Ferrari, K. Fraval,
S. Ganesan, A. R. García, G. Giubrone, M. B. Gómez-Hornillos, I. F. Gonçalves, E. González-Romero, F. Gramegna,
E. Griesmayer, P. Gurusamy, S. Harrisopulos, M. Heil, K. Ioannides, D. G. Jenkins, E. Jericha, Y. Kadi, D. Karadimos,
G. Korschinek, M. Krtička, J. Kroll, C. Langer, E. Lebbos, H. Leeb, L. S. Leong, R. Losito, M. Lozano, A. Manousos,
J. Marganiec, S. Marrone, T. Martinez, P. F. Mastinu, M. Mastromarco, M. Meaze, E. Mendoza, A. Mengoni,
P. M. Milazzo, F. Mingrone, M. Mirea, W. Mondalaers, C. Paradela, A. Pavlik, J. Perkowski, R. Plag, A. Plompen,
J. Praena, J. M. Quesada, T. Rauscher, A. Riego, F. Roman, C. Rubbia, R. Sarmento, P. Schillebeeckx, S. Schmidt,
G. Tagliente, J. L. Tain, D. Tarrío, L. Tassan-Got, A. Tsinganis, L. Tlustos, S. Valenta, G. Vannini, V. Variale, P. Vaz,
A. Ventura, M. J. Vermeulen, R. Versaci, V. Vlachoudis, R. Vlastou, T. Ware, M. Weigand, C. Weiß, T. J. Wright,
P. Žugec, n-TOF. Collaboration
^{62}Ni (n,γ) and ^{63}Ni (n,γ) cross sections measured at the n_TOF facility at CERN
Phys. Rev. C **89** (2): 025810, doi: 10.1103/PhysRevC.89.025810 (2014).

T. Lorenz, Y. Dai, D. Schumann, A. Türler
Proton-induced polonium production in lead
Nucl. Data Sheets **119**: 284-287, doi: 10.1016/j.nds.2014.08.078 (2014).

V. Margerin, A. S. J. Murphy, T. Davinson, R. Dressler, J. Fallis, A. Kankainen, A. M. Laird, G. Lotay, D. J. Mountford, C. D. Murphy, C. Seiffert, D. Schumann, T. Stowasser, T. Stora, C. H. T. Wang, P. J. Woods
Study of the reaction and implications for core collapse supernovae
Phys. Lett. B **731**: 358-361, doi: 10.1016/j.physletb.2014.03.003 (2014).

C. Massimi, P. Koehler, F. Mingrone, S. Altstadt, J. Andrzejewski, L. Audouin, M. Barbagallo, V. Bécares, F. Bečvář, F. Belloni, E. Berthoumieux, J. Billowes, D. Bosnar, M. Brugger, M. Calviani, F. Calviño, D. Cano-Ott, C. Carrapiço, F. Cerutti, E. Chiaveri, M. Chin, N. Colonna, G. Cortés, M. A. Cortés-Giraldo, M. Diakaki, C. Domingo-Pardo, I. Duran, R. Dressler, C. Eleftheriadis, A. Ferrari, K. Fraval, S. Ganesan, A. R. García, G. Giubrone, I. F. Gonçalves, E. González-Romero, E. Griesmayer, C. Guerrero, F. Gunsing, A. Hernández-Prieto, D. G. Jenkins, E. Jericha, Y. Kadi, F. Käppeler, D. Karadimos, N. Kivel, M. Krtička, J. Kroll, C. Lampoudis, C. Langer, E. Leal-Cidoncha, C. Lederer, H. Leeb, L. S. Leong, R. Losito, A. Mallick, A. Manousos, J. Marganiec, T. Martínez, P. F. Mastinu, M. Mastromarco, E. Mendoza, A. Mengoni, P. M. Milazzo, M. Mirea, W. Mondalaers, C. Paradela, A. Pavlik, J. Perkowski, A. Plompen, J. Praena, J. M. Quesada, T. Rauscher, R. Reifarth, A. Riego, M. S. Robles, C. Rubbia, M. Sabaté-Gilarte, R. Sarmento, A. Saxena, P. Schillebeeckx, S. Schmidt, D. Schumann, G. Tagliente, J. L. Tain, D. Tarrío, L. Tassan-Got, A. Tsinganis, S. Valenta, G. Vannini, V. Variale, P. Vaz, A. Ventura, M. J. Vermeulen, V. Vlachoudis, R. Vlastou, A. Wallner, T. Ware, M. Weigand, C. Weiß, T. Wright, P. Žugec
New measurement of the ^{25}Mg(n,γ) reaction cross section
Nucl. Data Sheets **119**: 110-112, doi: 10.1016/j.nds.2014.08.031 (2014).

E. A. Maugeri, J. Neuhausen, R. Eichler, D. Piguet, T. M. Mendonça, T. Stora, D. Schumann
Thermochromatography study of volatile polonium species in various gas atmospheres
J. Nucl. Mater. **450** (1-3): 292-298, doi: 10.1016/j.jnucmat.2013.11.024 (2014).

E. Mendoza, D. Cano-Ott, C. Guerrero, S. Altstadt, J. Andrzejewski, L. Audouin, M. Barbagallo, V. Bécares, F. Bečvář, F. Belloni, E. Berthoumieux, J. Billowes, V. Boccone, D. Bosnar, M. Brugger, M. Calviani, F. Calviño, C. Carrapiço, F. Cerutti, E. Chiaveri, M. Chin, N. Colonna, G. Cortés, M. A. Cortés-Giraldo, M. Diakaki, C. Domingo-Pardo, I. Duran, R. Dressler, N. Dzysiuk, C. Eleftheriadis, A. Ferrari, K. Fraval, S. Ganesan, A. R. García, G. Giubrone, M. B. Gómez-Hornillos, I. F. Gonçalves, E. González-Romero, E. Griesmayer, F. Gunsing, P. Gurusamy, D. G. Jenkins, E. Jericha, Y. Kadi, F. Käppeler, D. Karadimos, N. Kivel, P. Koehler, M. Kokkoris, G. Korschinek, M. Krtička, J. Kroll, C. Langer, C. Lederer, H. Leeb, L. S. Leong, R. Losito, A. Manousos, J. Marganiec, T. Martínez, P. F. Mastinu, M. Mastromarco, C. Massimi, M. Meaze, A. Mengoni, P. M. Milazzo, F. Mingrone, M. Mirea, W. Mondelaers, C. Paradela, A. Pavlik, J. Perkowski, M. Pignatari, A. Plompen, J. Praena, J. M. Quesada, T. Rauscher, R. Reifarth, A. Riego, F. Roman, C. Rubbia, R. Sarmento, P. Schillebeeckx, S. Schmidt, D. Schumann, G. Tagliente, J. L. Tain, D. Tarrío, L. Tassan-Got, A. Tsinganis, S. Valenta, G. Vannini, V. Variale, P. Vaz, A. Ventura, R. Versaci, M. J. Vermeulen, V. Vlachoudis, R. Vlastou, A. Wallner, T. Ware, M. Weigand, C. Weiß, T. J. Wright, P. Žugec
Measurement of the ^{241}Am and the ^{243}Am neutron capture cross sections at the n_TOF facility at CERN
Nucl. Data Sheets **119**: 65-68, doi: 10.1016/j.nds.2014.08.020 (2014).

E. Mendoza, D. Cano-Ott, C. Guerrero, E. Berthoumieux and the n_TOF collaboration
Pulse pile-up and dead time corrections for digitized signals from a BaF$_2$ calorimeter
Nucl. Instrum. Methods Phys. Res., Sect. A **768**: 55-61, doi: 10.1016/j.nima.2014.09.010 (2014).

F. Mingrone, C. Massimi, S. Altstadt, J. Andrzejewski, L. Audouin, M. Barbagallo, V. Bécares, F. Bečvář, F. Belloni, E. Berthoumieux, J. Billowes, D. Bosnar, M. Brugger, M. Calviani, F. Calviño, D. Cano-Ott, C. Carrapiço, F. Cerutti, E. Chiaveri, M. Chin, N. Colonna, G. Cortés, M. A. Cortés-Giraldo, M. Diakaki, C. Domingo-Pardo, I. Duran, R. Dressler, C. Eleftheriadis, A. Ferrari, K. Fraval, S. Ganesan, A. R. García, G. Giubrone, I. F. Gonçalves, E. González-Romero, E. Griesmayer, C. Guerrero, F. Gunsing, A. Hernández-Prieto, D. G. Jenkins, E. Jericha, Y. Kadi, F. Käppeler, D. Karadimos, N. Kivel, P. Koehler, M. Kokkoris, M. Krtička, J. Kroll, C. Lampoudis, C. Langer, E. Leal-Cidoncha, C. Lederer, H. Leeb, L. S. Leong, R. Losito, A. Mallick, A. Manousos, J. Marganiec, T. Martínez, P. F. Mastinu, M. Mastromarco, E. Mendoza, A. Mengoni, P. M. Milazzo, M. Mirea, W. Mondelaers, C. Paradela, A. Pavlik, J. Perkowski, A. Plompen, J. Praena, J. M. Quesada, T. Rauscher, R. Reifarth, A. Riego, M. S. Robles, C. Rubbia, M. Sabaté-Gilarte, R. Sarmento, A. Saxena, P. Schillebeeckx, S. Schmidt, D. Schumann, G. Tagliente, J. L. Tain, D. Tarrío, L. Tassan-Got, A. Tsinganis, S. Valenta, G. Vannini, V. Variale, P. Vaz, A. Ventura, M. J. Vermeulen, V. Vlachoudis, R. Vlastou, A. Wallner, T. Ware, M. Weigand, C. Weiß, T. Wright, P. Žugec
Measurement of the ^{238}U radiative capture cross section with C6D6 at the CERN n_TOF facility
Nucl. Data Sheets **119**: 18-21, doi: 10.1016/j.nds.2014.08.007 (2014).

K. Rijpstra, A. Van Yperen-De Deyne, J. Neuhausen, V. Van Speybroeck, S. Cottenier
Solution enthalpy of Po and Te in solid lead–bismuth eutectic
J. Nucl. Mater. **450** (1-3): 287-291, doi: 10.1016/j.jnucmat.2013.07.004 (2014).

M. Rizzi, J. Neuhausen, R. Eichler, A. Türler, T. M. Mendonça, T. Stora, B. Gonzalez Prieto, A. Aerts, D. Schumann
Polonium evaporation from dilute liquid metal solutions
J. Nucl. Mater. **450** (1–3): 304-313, doi: 10.1016/j.jnucmat.2014.01.047 (2014).

D. Schumann, J. C. David
Cross sections and excitation functions for the production of long-lived radionuclides in nuclear reactions of lead and bismuth with protons
Nucl. Data Sheets **119**: 288-291, doi: 10.1016/j.nds.2014.08.079 (2014).

D. Schumann, T. Stowasser, B. Volmert, I. Günther-Leopold, H. Linder, E. Wieland
Determination of the ^{14}C content in activated steel components from a neutron spallation source and a nuclear power plant
Anal. Chem. **86** (11): 5448-5454, doi: 10.1021/ac500654a (2014).

A. Tsinganis, E. Berthoumieux, C. Guerrero, N. Colonna, M. Calviani, R. Vlastou, S. Andriamonje, V. Vlachoudis, F. Gunsing, C. Massimi, S. Altstadt, J. Andrzejewski, L. Audouin, M. Barbagallo, V. Bécares, F. Bečvář, F. Belloni, J. Billowes, V. Boccone, D. Bosnar, M. Brugger, F. Calviño, D. Cano-Ott, C. Carrapiço, F. Cerutti, M. Chin, G. Cortés, M. A. Cortés-Giraldo, M. Diakaki, C. Domingo-Pardo, I. Duran, R. Dressler, N. Dzysiuk, C. Eleftheriadis, A. Ferrari, K. Fraval, S. Ganesan, A. R. García, G. Giubrone, M. B. Gómez-Hornillos, I. F. Gonçalves, E. González-Romero, E. Griesmayer, P. Gurusamy, A. Hernández-Prieto, D. G. Jenkins, E. Jericha, Y. Kadi, F. Käppeler, D. Karadimos, N. Kivel, P. Koehler, M. Kokkoris, M. Krtička, J. Kroll, C. Lampoudis, C. Langer, E. Leal-Cidoncha, C. Lederer, H. Leeb, L. S. Leong, R. Losito, A. Mallick, A. Manousos, J. Marganiec, T. Martínez, C. Massimi, P. F. Mastinu, M. Mastromarco, M. Meaze, E. Mendoza, A. Mengoni, P. M. Milazzo, F. Mingrone, M. Mirea, W. Mondalaers, C. Paradela, A. Pavlik, J. Perkowski, A. Plompen, J. Praena, J. M. Quesada, T. Rauscher, R. Reifarth, A. Riego, M. S. Robles, F. Roman, C. Rubbia, M. Sabaté-Gilarte, R. Sarmento, A. Saxena, P. Schillebeeckx, S. Schmidt, D. Schumann, G. Tagliente, J. L. Tain, D. Tarrío, L. Tassan-Got, S. Valenta, G. Vannini, V. Variale, P. Vaz, A. Ventura, R. Versaci, M. J. Vermeulen, A. Wallner, T. Ware, M. Weigand, C. Weiss, T. Wright, P. Žugec
Measurement of the $^{242}Pu(n,f)$ cross section at the CERN n_TOF facility
Nucl. Data Sheets **119**: 58-60, doi: 10.1016/j.nds.2014.08.018 (2014).

C. Weiß, C. Guerrero, E. Griesmayer, J. Andrzejewski, G. Badurek, E. Chiaveri, R. Dressler, S. Ganesan, E. Jericha, F. Käppeler, P. Koehler, C. Lederer, H. Leeb, J. Marganiec, A. Pavlik, J. Perkowski, T. Rauscher, R. Reifarth, D. Schumann, G. Tagliente, V. Vlachoudis, S. Altstadt, L. Audouin, M. Barbagallo, V. Bécares, F. Bečvář, F. Belloni, E. Berthoumieux, J. Billowes, V. Boccone, D. Bosnar, M. Brugger, M. Calviani, F. Calviño, D. Cano-Ott, C. Carrapiço, F. Cerutti, M. Chin, N. Colonna, G. Cortés, M. A. Cortés-Giraldo, M. Diakaki, C. Domingo-Pardo, I. Duran, N. Dzysiuk, C. Eleftheriadis, A. Ferrari, K. Fraval, A. R. García, G. Giubrone, M. B. Gómez-Hornillos, I. F. Gonçalves, E. González-Romero, F. Gunsing, P. Gurusamy, A. Hernández-Prieto, D. G. Jenkins, Y. Kadi, D. Karadimos, N. Kivel, M. Kokkoris, M. Krtička, J. Kroll, C. Lampoudis, C. Langer, E. Leal-Cidoncha, L. S. Leong, R. Losito, A. Mallick, A. Manousos, T. Martínez, C. Massimi, P. F. Mastinu, M. Mastromarco, M. Meaze, E. Mendoza, A. Mengoni, P. M. Milazzo, F. Mingrone, M. Mirea, W. Mondalaers, C. Paradela, A. Plompen, J. Praena, J. M. Quesada, A. Riego, M. S. Robles, F. Roman, C. Rubbia, M. Sabaté-Gilarte, R. Sarmento, A. Saxena, P. Schillebeeckx, S. Schmidt, J. L. Tain, D. Tarrío, L. Tassan-Got, A. Tsinganis, S. Valenta, G. Vannini, V. Variale, P. Vaz, A. Ventura, R. Versaci, M. J. Vermeulen, R. Vlastou, A. Wallner, T. Ware, M. Weigand, T. Wright, P. Žugec
The (n, α) reaction in the s-process branching point ^{59}Ni
Nucl. Data Sheets **120**: 208-210, doi: 10.1016/j.nds.2014.07.048 (2014).

T. Wright, C. Guerrero, J. Billowes, T. Ware, D. Cano-Ott, E. Mendoza, C. Massimi, F. Mingrone, F. Gunsing, E. Berthoumieux, C. Lampoudis, S. Altstadt, J. Andrzejewski, L. Audouin, M. Barbagallo, V. Bécares, F. Bečvář, F. Belloni, V. Boccone, D. Bosnar, M. Brugger, M. Calviani, F. Calviño, C. Carrapiço, F. Cerutti, E. Chiaveri, M. Chin, N. Colonna, G. Cortés, M. A. Cortés-Giraldo, M. Diakaki, C. Domingo-Pardo, I. Duran, R. Dressler, N. Dzysiuk, C. Eleftheriadis, A. Ferrari, K. Fraval, S. Ganesan, A. R. García, M. B. Gómez-Hornillos, I. F. Gonçalves, E. González-Romero, E. Griesmayer, G. Giubrone, P. Gurusamy, D. G. Jenkins, E. Jericha, Y. Kadi, F. Käppeler, D. Karadimos, N. Kivel, P. Koehler, M. Kokkoris, G. Korschinek, M. Krtička, J. Kroll, C. Langer, C. Lederer, H. Leeb, L. S. Leong, R. Losito, A. Manousos, J. Marganiec, T. Martínez, P. F. Mastinu, M. Mastromarco, M. Meaze, A. Mengoni, P. M. Milazzo, M. Mirea, W. Mondelaers, C. Paradela, A. Pavlik, J. Perkowski, M. Pignatari, A. Plompen, J. Praena, J. M. Quesada, T. Rauscher, R. Reifarth, A. Riego, F. Roman, C. Rubbia, R. Sarmento, P. Schillebeeckx, S. Schmidt, D. Schumann, G. Tagliente, J. L. Tain, D. Tarrío, L. Tassan-Got, A. Tsinganis, S. Valenta, G. Vannini, V. Variale, P. Vaz, A. Ventura, R. Versaci, M. J. Vermeulen, V. Vlachoudis, R. Vlastou, A. Wallner, M. Weigand, C. Weiß, P. Žugec
High-precision measurement of the $^{238}U(n,\gamma)$ cross section with the total absorption calorimeter (TAC) at n_TOF, CERN
Nucl. Data Sheets **119**: 26-30, doi: 10.1016/j.nds.2014.08.009 (2014).

P. Žugec, N. Colonna, D. Bosnar, S. Altstadt, J. Andrzejewski, L. Audouin, M. Barbagallo, V. Bécares, F. Bečvář, F. Belloni, E. Berthoumieux, J. Billowes, V. Boccone, M. Brugger, M. Calviani, F. Calviño, D. Cano-Ott, C. Carrapiço, F. Cerutti, E. Chiaveri, M. Chin, G. Cortés, M. A. Cortés-Giraldo, M. Diakaki, C. Domingo-Pardo, R. Dressler, I. Duran, N. Dzysiuk, C. Eleftheriadis, A. Ferrari, K. Fraval, S. Ganesan, A. R. García, G. Giubrone, M. B. Gómez-Hornillos, I. F. Gonçalves, E. González-Romero, E. Griesmayer, C. Guerrero, F. Gunsing, P. Gurusamy, S. Heinitz, D. G. Jenkins, E. Jericha, Y. Kadi, F. Käppeler, D. Karadimos, N. Kivel, P. Koehler, M. Kokkoris, M. Krtička, J. Kroll, C. Langer, C. Lederer, H. Leeb, L. S. Leong, S. Lo Meo, R. Losito, A. Manousos, J. Marganiec, T. Martínez, C. Massimi, P. F. Mastinu, M. Mastromarco, M. Meaze, E. Mendoza, A. Mengoni, P. M. Milazzo, F. Mingrone, M. Mirea, W. Mondalaers, C. Paradela, A. Pavlik, J. Perkowski, A. Plompen, J. Praena, J. M. Quesada, T. Rauscher, R. Reifarth, A. Riego, F. Roman, C. Rubbia, R. Sarmento, A. Saxena, P. Schillebeeckx, S. Schmidt, D. Schumann, G. Tagliente, J. L. Tain, D. Tarrío, L. Tassan-Got, A. Tsinganis, S. Valenta, G. Vannini, V. Variale, P. Vaz, A. Ventura, R. Versaci, M. J. Vermeulen, V. Vlachoudis, R. Vlastou, A. Wallner, T. Ware, M. Weigand, C. Weiß, T. Wright
GEANT4 simulation of the neutron background of the C6D6 set-up for capture studies at n_TOF
Nucl. Instrum. Methods Phys. Res., Sect. A **760**: 57-67, doi: 10.1016/j.nima.2014.05.048 (2014).

P. Žugec, N. Colonna, D. Bosnar, A. Mengoni, S. Altstadt, J. Andrzejewski, L. Audouin, M. Barbagallo, V. Bécares, F. Bečvář, F. Belloni, E. Berthoumieux, J. Billowes, V. Boccone, M. Brugger, M. Calviani, F. Calviño, D. Cano-Ott, C. Carrapiço, F. Cerutti, E. Chiaveri, M. Chin, G. Cortés, M. A. Cortés-Giraldo, L. Cosentino, M. Diakaki, C. Domingo-Pardo, R. Dressler, I. Duran, C. Eleftheriadis, A. Ferrari, P. Finocchiaro, K. Fraval, S. Ganesan, A. R. García, G. Giubrone, M. B. Gómez-Hornillos, I. F. Gonçalves, E. González-Romero, E. Griesmayer, C. Guerrero, F. Gunsing, P. Gurusamy, S. Heinitz, D. G. Jenkins, E. Jericha, F. Käppeler, D. Karadimos, N. Kivel, M. Kokkoris, M. Krtička, J. Kroll, C. Langer, C. Lederer, H. Leeb, L. S. Leong, S. Lo Meo, R. Losito, A. Manousos, J. Marganiec, T. Martínez, C. Massimi, P. Mastinu, M. Mastromarco, E. Mendoza, P. M. Milazzo, F. Mingrone, M. Mirea, W. Mondalaers, A. Musumarra, C. Paradela, A. Pavlik, J. Perkowski, A. Plompen, J. Praena, J. Quesada, T. Rauscher, R. Reifarth, A. Riego, F. Roman, C. Rubbia, R. Sarmento, A. Saxena, P. Schillebeeckx, S. Schmidt, D. Schumann, G. Tagliente, J. L. Tain, D. Tarrío, L. Tassan-Got, A. Tsinganis, S. Valenta, G. Vannini, V. Variale, P. Vaz, A. Ventura, R. Versaci, M. J. Vermeulen, V. Vlachoudis, R. Vlastou, A. Wallner, T. Ware, M. Weigand, C. Weiß, T. Wright, n-TOF Collaboration
Measurement of the ^{12}C (n, p) ^{12}B cross section at n_TOF at CERN by in-beam activation analysis
Phys. Rev. C **90** (2): 021601, doi: 10.1016/j.nima.2014.05.048 (2014).

RADIONUCLIDE DEVELOPMENT - CHEMISTRY

M. Bunka, C. Müller, K. A. Domnanich, R. Schibli, A. Türler, N. P. van der Meulen
^{44}Sc production development from ^{44}Ca for radiopharmaceutical application
Nucl. Med. Biol. **41** (7): 646-646, doi: 10.1016/j.nucmedbio.2014.05.051 (2014).

J. Grünberg, D. Lindenblatt, H. Dorrer, S. Cohrs, K. Zhernosekov, U. Köster, A. Türler, E. Fischer, R. Schibli
Anti-L1CAM radioimmunotherapy is more effective with the radiolanthanide terbium-161 compared to lutetium-177 in an ovarian cancer model
Eur. J. Nucl. Med. Mol. Imag. **41** (10): 1907-1915, doi: 10.1007/s00259-014-2798-3 (2014).

C. Müller, M. Bunka, S. Haller, U. Köster, V. Groehn, P. Bernhardt, N. van der Meulen, A. Türler, R. Schibli
Promising prospects for ^{44}Sc-/^{47}Sc-based theragnostics: Application of ^{47}Sc for radionuclide tumor therapy in mice
J. Nucl. Med. **55** (10): 1658-1664, doi: 10.2967/jnumed.114.141614 (2014).

C. Müller, M. Bunka, S. Haller, U. Koster, N. van der Meulen, A. Türler, R. Schibli
Preclinical application of ^{47}Sc-folate - A pilot study in tumor-bearing mice
Nucl. Med. Biol. **41** (7): 638-638, doi: 10.1016/j.nucmedbio.2014.05.026 (2014).

C. Müller, E. Fischer, M. Behe, U. Köster, H. Dorrer, J. Reber, S. Haller, S. Cohrs, A. Blanc, J. Grünberg, M. Bunka, K. Zhernosekov, N. van der Meulen, K. Johnston, A. Türler, R. Schibli
Future prospects for SPECT imaging using the radiolanthanide terbium-155 — production and preclinical evaluation in tumor-bearing mice
Nucl. Med. Biol. **41**: 58-65, doi: 10.1016/j.nucmedbio.2013.11.002 (2014).

C. Müller, J. Reber, S. Haller, H. Dorrer, P. Bernhardt, K. Zhernosekov, A. Türler, R. Schibli
Direct in vitro and in vivo comparison of ^{161}Tb and ^{177}Lu using a tumour-targeting folate conjugate
Eur. J. Nucl. Med. Mol. Imag. **41** (3): 476-485, doi: 10.1007/s00259-013-2563-z (2014).

C. Müller, J. Reber, S. Haller, H. Dorrer, U. Köster, K. Johnston, K. Zhernosekov, A. Türler, R. Schibli
Folate receptor targeted alpha-therapy using terbium-149
Pharmaceuticals **7** (3): 353-365, doi: 10.3390/ph7030353 (2014).

G. F. Steyn, C. Vermeulen, F. Szelecsényi, Z. Kovács, A. Hohn, N. P. van der Meulen, R. Schibli, T. N. van der Walt
Cross sections of proton-induced reactions on ^{152}Gd, ^{155}Gd and ^{159}Tb with emphasis on the production of selected Tb radionuclides
Nucl. Instrum. Methods Phys. Res., Sect. B **319**: 128-140, doi: 10.1016/j.nimb.2013.11.013 (2014).

N. P. van der Meulen, T. N. van der Walt, G. F. Steyn, H. G. Raubenheimer
Erratum to "The production of ^{82}Sr using larger format RbCl targets" [Appl. Radiat. Isotopes 72 (2013) 96–99]
Appl. Radiat. Isot. **83**: 36, doi: 10.1016/j.apradiso.2013.09.017 (2014).

ENVIRONMENTAL RADIONUCLIDES UNIVERSITÄT BERN

R.-J. Huang, Y. Zhang, C. Bozzetti, K.-F. Ho, J.-J. Cao, Y. Han, K. R. Daellenbach, J. G. Slowik, S. M. Platt, F. Canonaco, P. Zotter, R. Wolf, S. M. Pieber, E. A. Bruns, M. Crippa, G. Ciarelli, A. Piazzalunga, M. Schwikowski, G. Abbaszade, J. Schnelle-Kreis, R. Zimmermann, Z. An, S. Szidat, U. Baltensperger, I. El Haddad, A. S. H. Prevot
High secondary aerosol contribution to particulate pollution during haze events in China
Nature **514** (7521): 218-222, doi: 10.1038/nature13774 (2014).

A. Kotrschal, S. Szidat, B. Taborsky
Developmental plasticity of growth and digestive efficiency in dependence of early-life food availability
Funct. Ecol. **28** (4): 878-885, doi: 10.1111/1365-2435.12230 (2014).

J. Liu, J. Li, Y. Zhang, D. Liu, P. Ding, C. Shen, K. Shen, Q. He, X. Ding, X. Wang, D. Chen, S. Szidat, G. Zhang
Source apportionment using radiocarbon and organic tracers for PM2.5 carbonaceous aerosols in Guangzhou, South China: Contrasting local- and regional-scale haze events
Environ. Sci. Technol. **48** (20): 12002-12011, doi: 10.1021/es503102w (2014).

M. Pandolfi, X. Querol, A. Alastuey, J. L. Jimenez, O. Jorba, D. Day, A. Ortega, M. J. Cubison, A. Comerón, M. Sicard, C. Mohr, A. S. H. Prévôt, M. C. Minguillón, J. Pey, J. M. Baldasano, J. F. Burkhart, R. Seco, J. Peñuelas, B. L. van Drooge, B. Artiñano, C. Di Marco, E. Nemitz, S. Schallhart, A. Metzger, A. Hansel, J. Lorente, S. Ng, J. Jayne, S. Szidat
Effects of sources and meteorology on particulate matter in the Western Mediterranean Basin: An overview of the DAURE campaign
J. Geophys. Res.-Atmos. **119** (8): 4978-5010, doi: 10.1002/2013JD021079 (2014).

S. Szidat, G. A. Salazar, E. Vogel, M. Battaglia, L. Wacker, H.-A. Synal, A. Türler
^{14}C analysis and sample preparation at the new Bern Laboratory for the Analysis of Radiocarbon with AMS (LARA)
Radiocarbon **56** (2): 561-566, doi: 10.2458/56.17457 (2014).

Y.-L. Zhang, J. Li, G. Zhang, P. Zotter, R.-J. Huang, J.-H. Tang, L. Wacker, A. S. H. Prévôt, S. Szidat
Radiocarbon-based source apportionment of carbonaceous aerosols at a regional background site on Hainan Island, South China
Environ. Sci. Technol. **48** (5): 2651-2659, doi: 10.1021/es4050852 (2014).

Y.-L. Zhang, J.-W. Liu, G. A. Salazar, J. Li, P. Zotter, G. Zhang, R.-R. Shen, K. Schäfer, J. Schnelle-Kreis, A. S. H. Prévôt, S. Szidat
Micro-scale (µg) radiocarbon analysis of water-soluble organic carbon in aerosol samples
Atmos. Environ. **97**: 1-5, doi: 10.1016/j.atmosenv.2014.07.059 (2014).

P. Zotter, V. G. Ciobanu, Y. L. Zhang, I. El-Haddad, M. Macchia, K. R. Daellenbach, G. A. Salazar, R. J. Huang, L. Wacker, C. Hueglin, A. Piazzalunga, P. Fermo, M. Schwikowski, U. Baltensperger, S. Szidat, A. S. H. Prévôt
Radiocarbon analysis of elemental and organic carbon in Switzerland during winter-smog episodes from 2008 to 2012 – Part 1: Source apportionment and spatial variability
Atmos. Chem. Phys. **14** (24): 13551-13570, doi: 10.5194/acp-14-13551-2014 (2014).

P. Zotter, I. El-Haddad, Y. Zhang, P. L. Hayes, X. Zhang, Y.-H. Lin, L. Wacker, J. Schnelle-Kreis, G. Abbaszade, R. Zimmermann, J. D. Surratt, R. Weber, J. L. Jimenez, S. Szidat, U. Baltensperger, A. S. H. Prévôt
Diurnal cycle of fossil and nonfossil carbon using radiocarbon analyses during CalNex
J. Geophys. Res.-Atmos. **119** (11): 6818-6835, doi: 10.1002/2013JD021114 (2014).

CONTRIBUTIONS TO CONFERENCES, WORKSHOPS AND SEMINARS

HEAVY ELEMENTS

N. Chiera, R. Eichler, A. Türler
Towards selenides of the superheavy elements Cn and Fl
17th Radiochemical Conference, Marianske Lazne, Czech Republic, 11-16 May, 2014.

N. Chiera, R. Eichler, A. Türler
Towards selenides of the superheavy elements Cn and Fl
248th ACS National Meeting & Exposition, San Francisco, USA, 10-14 August, 2014.

N. Chiera
Towards the selenides of the superheavy elements copernicium and flerovium
1st year Graduate Symposium, University of Bern, Switzerland, 8 September, 2014.

N. Chiera
Towards the selenides of the superheavy elements copernicium and flerovium
Seminar of the Laboratory of Radiochemistry and Environmental Chemistry, Paul Scherrer Institut and University of Berne, Bern, Switzerland, 12 December 2014.

R. Eichler, N. Chiera, P. Steinegger, A. Türler, I. Usoltsev
Potential and future of chemical investigations with superheavy elements
VII International Symposium on Exotic Nuclei "EXON", Kaliningrad, Russia, 9 September 2014.

R. Eichler
Gas phase adsorption of radon: Tritium meets superheavy elements
27th KATRIN Collaboration Meeting, Karlsruhe, Germany, 15-17 October, 2014.

H.W. Gäggeler
Progress in heavy element research at PSI
Massey University, Institute for theoretical Physics and Chemistry, Albany, New Zealand, 19 Febrary, 2014.

H.W. Gäggeler
Progress in heavy element research at PSI
University of Auckland, New Zealand, 4 March, 2014.

P. Steinegger
On-line isothermal vacuum chromatography
Seminar of the Laboratory of Radiochemistry and Environmental Chemistry, Paul Scherrer Institut and University of Berne, Bern, Switzerland, 12 December, 2014.

A. Türler
Synthese und Charakterisierung Superschwerer Elemente
Helmholtzzentrum Dresden-Rossendorf, HZDR Kolloquium, Rossnedorf, Germany, 5 May, 2014.

A. Türler
Positioning the New Elements in the Periodic Table
17th Radiochemical Conference, Marianske Lazne, Czech Republic, 11-16 May, 2014.

A. Türler
Chemistry of Superheavy Elements
European Commission, Joint Research Centre (JRC), Institute for Transuranium Elements, Karlsruhe, 11 June, 2014.

A. Türler
Heavy and Superheavy Elements Research
8th International Conference on Isotopes and Expo, Chicago, United States, 24-28 Augus,t 2014.

A. Türler
Recent Results from the Field of Superheavy Element Research
Zakopane Conference on Nuclear Physics, Zakopane, Poland, 31 August - 7 September, 2014.

A. Türler
Transactinide Cabonyl Complexes: a New Class of Compounds in Superheavy Element Chemistry
VII International Symposium on Exotic Nuclei "EXON", Kaliningrad, Russia, 8-13 September, 2014.

A. Türler
Recent Results from the Field of Superheavy Element Research in Europe
Fourth Joint Meeting of the Nuclear Physics Divisions of the American Physical Society and The Physical Society of Japan, Hilton Waikoloa Village, Hawaii, United States, 7-11 October, 2014.

I. Usoltsev
Decomposition studies of W and Mo carbonyl complexes and their implications for future experiments with $Sg(CO)_6$
17th Radiochemical Conference, Marianske Lazne, Czech Republic, 11-16 May, 2014.

I. Usoltsev
Group VI metal hexacarbonyl complexes: production, decomposition, modelling
TASCA 14, 13th Workshop on Recoil Separator for Superheavy Element Chemistry, GSI, Darmstadt, Germany, 21 October, 2014.

SURFACE CHEMISTRY

M. Ammann
The reaction of ozone with aerosol particles: Kinetics and spectroscopy
Kolloquium Laboratorium für Physikalische Chemie, ETH Zürich, Switzerland, 4 March, 2014.

M. Ammann, M. Lampimäki, S. Schreiber, V. Zelenay, A. Krepelová, R. Chang, H. Bluhm, Z. Liu
Photocatalysis of NO_X on TiO_2 caught in the act
PhotoPAQ Conference 2014: Photocatalysis: Science and Application for Urban Air Quality, Lyon, France, 15-17 April, 2014.

M. Ammann
Adsorption of acidic gases on ice: Dissociation and effects on the hydrogen bonding environment
Ice workshop, Department of Chemistry and Molecular Biology, University of Gothenburg, Gothenburg, Sweden, 3 June, 2014.

M. Ammann
Oxidant exchange between the gas and aerosol phase: Physical state effects, photochemistry and the role of surfaces
Telluride Workshop New Insights Into Gas-Phase Atmospheric Chemistry, Telluride, Colorado, USA, 28 July - 1 August, 2014.

M. Ammann
The role of the surface in chemical transformations of aerosol particles
Towards a Molecular-Level Understanding of Atmospheric Aerosols, Ascona, Switzerland, 31 August - 5 September, 2014.

M. Ammann
Photoelectron spectroscopy on ice, mineral oxides and aqueous solutions of atmospheric relevance
AVS 61st International Symposium and Exhibition, Baltimore, USA, 9-14 November, 2014.

M. Ammann
Photoelectron spectroscopy on ice, mineral oxides and aqueous solutions of atmospheric relevance
International workshop on: Surface Chemistry and Near-Ambient Pressure Photoemission, Synchrotron SOLEIL, Paris, France, 10-12 December, 2014.

T. Bartels-Rausch
Surface and bulk uptake of hydrogen peroxide to snow: What we have learned in 30 years from lab studies
13th International Conference on the Physics and Chemistry of Ice, Hanover, USA, 17-20 March, 2014.

T. Bartels-Rausch, T. Ulrich, M. Ammann
Surface and bulk uptake of H_2O_2 to snow: Insights from laboratory studies
European Geosciences Union General Assembly, Vienna, Austria, 27 April - 2 May, 2014.

T. Bartels-Rausch
Can laboratory data explain field observations? The fluxes of HNO_3 and HNO_4 from snowin the lab and in Antarctica
Workshop on Chemical Atmosphere – snow - sea Ice Interactions: Taking the next big step in the field, lab & modelling, Cambridge, United Kingdom, 13-15 October, 2014.

G. Gržinić, T. Bartels-Rausch, A. Türler, M. Ammann
Humidity dependence of N_2O_5 uptake to citric acid aerosol particles
2014 International Aerosol Conference, Bexco, Busan, South Korea, 28 August - 2 September 2014.

M. T. Lee, M. A. Brown, T. Bartels-Rausch, S. Kato, M. Lampimäki, J. A. v. Bokhoven, F. Nolting, A. Kleibert, A. Türler, M. Ammann
The sea-salt solution - air interfacial composition via liquid microjet XPS
Evolution of Surface Science and Technologies, Fribourg, Switzerland, 24 January, 2014.

M. T. Lee
The effect of organic surfactants on the distribution of ions at the electrolyte solution – air interface
Seminar of the Laboratory of Radiochemistry and Environmental Chemistry, Paul Scherrer Institut and University of Berne, University of Bern, Bern, Switzerland, 11 April, 2014.

M. T. Lee, M. Brown, S. Kato, A. Kleibert, A. Türler, J. v. Bokhoven, M. Ammann
Composition of the sea-salt solution - air interface as effected by organics
248th American Chemical Society National Meeting & Exposition, San Francisco, USA, 11 August, 2014.

M. T. Lee, F. Orlando, M. Brown, S. Kato, A. Kleibert, A. Türler, M. Ammann
Composition of the sea-salt solution - air interface as effected by organics
International workshop on: Surface Chemistry and Near-Ambient Pressure Photoemission, Synchrotron SOLEIL, Paris, France, 10-12 December, 2014.

P. S. J. Matthews, M. Krapf, J. Dommen, I. J. George, L. K. Whalley, T. Ingham, M. T. Baeza-Romero, M. Ammann, D. E. Heard
The uptake of HO_2 radicals to organic aerosols
European Geosciences Union General Assembly, Vienna, Austria, 27 April - 2 May, 2014.

H. Meusel, Y. Elshorbany, T. Bartels-Rausch, K. Selzle, J. Lelieveld, M. Ammann, U. Pöschl, H. Su, Y. Cheng
Photo-induced formation of nitrous acid (HONO) on protein surfaces
European Geosciences Union General Assembly, Vienna, Austria, 27 April - 2 May, 2014.

F. Orlando, A. Waldner, M. T. Lee, M. Birrer, T. Bartels-Rausch, C. Proff, J. A. v. Bokhoven, M. Ammann
A novel analysis chamber for near ambient pressure XPS of solid surfaces for environmental and catalysis research
International workshop on: Surface Chemistry and Near-Ambient Pressure Photoemission, Synchrotron SOLEIL, Paris, France, 10-12 December, 2014.

S. Steimer
Influence of physical state on shikimic acid ozonolysis
Seminar of the Laboratory of Radiochemistry and Environmental Chemistry, Paul Scherrer Institut and University of Berne, Villigen, Switzerland, 09 May, 2014.

S. Steimer, U. Krieger, M. Lampimäki, T. Peter, M. Ammann
Influence of physical state on shikimic acid ozonolysis
Goldschmidt 2014, Sacramento, USA, 08-13 June, 2014.

S. Steimer, U. Krieger, M. Lampimäki, T. Peter, M. Ammann
Interplay of diffusivity and reactivity in organic aerosol ageing
Towards a Molecular-Level Understanding of Atmospheric Aerosols, Ascona, Switzerland, 31 August - 5 September, 2014.

S. Steimer, U. Krieger, M. Lampimäki, T. Peter, M. Ammann
Influence of physical state on the ozonolysis of shikimic acid
European Geosciences Union General Assembly, Vienna, Austria, 27 April - 02 May, 2014.

A. Waldner, M. Ammann, T. Peter, T. Bartels-Rausch
Molecular picture of acids adsorbed at ice surfaces - Surface sensitive Near Ambient Pressure Photoemission Spectroscopy at SLS
The European Network, Atmospheric Composition Change Summer School, Urbino, Italy, 22-29 June 2014.

A. Waldner, M. Ammann, T. Peter, T. Bartels-Rausch
Acidic trace gas adsorption on ice: XPS and NEXAFS analysis with the new NAPP solid chamber at SLS
Workshop on Chemical Atmosphere – snow - sea Ice Interactions: Taking the next big step in the field, lab & modelling, Cambridge, UK, 13-15 October, 2014.

A. Waldner
Ice: Surface sensitive investigations of the interaction of atmospheric acidic trace gases with ice surfaces
Seminar of the Laboratory of Radiochemistry and Environmental Chemistry, Paul Scherrer Institut and University of Berne, Villigen, Switzerland, 14 November, 2014.

ANALYTICAL CHEMISTRY

A. Eichler, G. Gramlich, T. Kellerhals, L. Tobler, M. Schwikowski
Two millennia of Pb pollution related to Altiplano metallurgical activities and leaded gasoline in South America from Illimani ice core
AGU Fall Meeting, San Francisco, USA, 15-19 December, 2014.

S. Eyrikh, L. Tobler, N. Malygina, T. Papina, M. Schwikowski
The mercury signature of anthropogenic and natural events recorded in 300-years ice core from a Belukha glacier (Altai region)
17th Int. Conference on Heavy Metals in the Environment (ICHMET), Guiyang, China, 22-25 September, 2014.

J. Gabbi, M. Huss, A. Bauder, M. Schwikowski
The impact of Saharan dust events on long-term glacier mass balance in the Alps
12th Swiss Geoscience Meeting, Fribourg, Switzerland, 21-22 November, 2014.

J. Gabbi, M. Huss, A. Bauder, M. Schwikowski
The impact of Saharan dust events on long-term glacier mass balance in the Alps
AGU Fall Meeting, San Francisco, USA, 15-19 December, 2014.

H.W. Gäggeler
From joint KUER engagement to beryllium-10 endeavors
Symposium to honor Prof. Dr. Jürg Beer, EAWAG, Dübendorf, Switzerland 16 October, 2014.

G. Gramlich, L. Tobler, A. Eichler, T. Kellerhals, M. Schwikowski
Evidence for pre-Incan lead pollution from Illimani ice core
Int. Conference on Culture Climate and Environment Interactions at Prehistoric Wetland Sites, University of Bern, Switzerland, 11-14 June, 2014.

T.M. Jenk, P.-A. Herren, A. Eichler, M. Schwikowski
Climate reconstructions from high-alpine ice cores: Example from the Mongolian Altai
OCCR Plenary Meeting, University of Bern, Switzerland, 11 September, 2014.

P. Pavlova, P. Schmid, C. Bogdal, C. Steinlin, M. Schwikowski
Effect of melting on redistribution and release of PCBs from Alpine glaciers
34th Int. Symposium on Halogenated Persistent Organic Pollutants – Dioxin 2014, Madrid, Spain,
31 August - 5 September, 2014.

M. Schwikowski
Personal experience as member of the ERC Starting Grant panel in 2013
Information Event "HORIZON 2020" at PSI, Paul Scherrer Institut, Switzerland, 20 January, 2014.

M. Schwikowski
Schnee von gestern - Gletscher als Archiv zur Rekonstruktion der Luftverschmutzung,
Chemie plus Userday 2014, Metrohm International Headquarters, Herisau, Switzerland, 30 April, 2014.

M. Schwikowski, G. Gramlich, L. Tobler, A. Eichler, T Kellerhals
Evidence for climate influences on the decline of the pre-Incan Tiwanaku civilization from Illimani ice core
LOTRED-SA 3rd Int. Symposium on Climate Change and Human Impact in Central and South America over the last 2000 years, Observations and Models, Medellín, Colombia, 9-11, July 2014.

M. Schwikowski
Glaciers as archives of past climatic and environmental conditions
Seminar of the Center for Radiopharmaceutical Sciences, Paul Scherrer Institut, Switzerland, 3 October, 2014.

M. Schwikowski
Into thin ice: Drilling on high-alpine glaciers
Swiss Geoscience Meeting, Fribourg, Switzerland, 21-22 November, 2014.

L. Sold, M. Huss, A. Eichler, M. Schwikowski, M. Hoelzle
Recent accumulation rates of an Alpine glacier derived from repeated airborne GPR and firn cores
European Geosciences Union General Assembly, Vienna, Austria, 27 April - 02 May, 2014.

C. Steinlin, C. Bogdal, M.P. Lüthi, M. Scheringer, P.A. Pavlova, M. Schwikowski, P. Schmid, K. Hungerbühler
The fate of polychlorinated biphenyls in Alpine glaciers
34th Int. Symposium on Halogenated Persistent Organic Pollutants – Dioxin 2014, Madrid, Spain,
31 August - 5 September, 2014.

RADWASTE ANALYTICS

R. Dressler, D. Schumann
Accelerator Waste – a source for exotic isotopes
8th ICI, Chicago, USA, 24-28 August, 2014.

C. Guerrero, C. Domingo-Pardo, D. Schumann, S. Heinitz, U. Köster
Hunting the s-process branching points ^{147}Pm, ^{171}Tm and ^{204}Tl at CERN
XIII Nuclei in the Cosmos, Debrecen, Hungary, 7-11 July, 2014.

S. Heinitz
Sample preparation
n_TOF annual meeting, CERN, Switzerland, 10-11 December, 2014.

D. Kiselev, T. Lorenz, Yong Dai, J.-Ch. David, D. Schumann, M. Wohlmuther
Po-production in lead: Calculation and measurement on SINQ-samples (PSI)
SATIF-12, Fermilab, USA, 28-30 April, 2014.

D. Kiselev, M. Wohlmuther, J.-Ch. David, Y. Dai, T. Lorenz, D. Schumann
Polonium-Produktion in Blei: Berechnung und Messung an SINQ Proben
ASI Mittagsseminar, Paul Scherrer Institut, Switzerland, 11 November, 2014.

N. Kivel, H.-D. Potthast, D. Schumann
Separation of isobaric interferences in HR-ICP-MS
8th ICI, Chicago, USA, 24-28 August, 2014.

E. A. Maugeri, J. Neuhausen, R. Eichler, D. Schumann
Thermochromatography study of volatile Po species in various gas atmospheres
SEARCH/MAXSIMA International Workshop 2014 Karlsuhe, Germany, 7 October, 2014.

J. Neuhausen, E. A. Maugeri, R. Eichler
SEARCH WP6 - Release, gas phase transport and capture studies of volatiles
Joint SEARCH and MAXIMA technical review meeting, Ghent, Belgium, 28-30 April, 2014.

J. Neuhausen
Release of volatile radionuclides from ADS and their capture
Seminar of the Laboratory of Radiochemistry and Environmental Chemistry, Paul Scherrer Institut and University of Berne, Villigen, Switzerland, 09 May, 2014.

J. Neuhausen
Properties of irradiated LBE and Pb
OECD Heavy Liquid Metal Expert Group Meeting, Issy-les Moulineaux, France, 25 June, 2014.

A. Nucciotti, B. Alpert, M. Balat, D. Bennett, M. Biasotti, C. Boragno, C. Brofferio, V. Ceriale, M. De Gerone, R. Dressler, M. Faverzani, E. Ferri, J. Fowler, F. Gatti, A. Giachero, St. Heinitz, M. Lusignoli, G. Hilton, U. Köster, M. Maino, J. Mates, S. Nisi, R. Nizzolo, G. Pessina, G. Pizzigoni, A. Puiu, S. Ragazzi, C. Reintsema, M. Ribeiro-Gomes, D. Schmidt, D. Schumann, M. Sisti, D. Swetz, F. Terranova, J. Ullom
The HOLMES experiment,
Neutrino 2014, Boston, USA, 02-04 June, 2014.

D. Schumann
ERAWAST
CHANDA WP3, Paul Scherrer Institut, Villigen, 15 March, 2014.

D. Schumann
The ERAWAST initiative – how radioactive waste can be used for astrophysics experiments
CERN ISOLDE, Switzerland, 06 May, 2014.

D. Schumann
ERAWAST – radioactive samples for nuclear astrophysics
UCLA, Los Angeles, USA, 22 August, 2014.

D. Schumann, M. Ayranov, T. Stowasser
Separation of ^{7}Be from the cooling water of a neutron spallation source
8th ICI, Chicago, USA, 24-28 August, 2014.

D. Schumann, J. Neuhausen, B. Hammer, M. Wohlmuther, D. Kiselev, V. Boutellier, H.-P. Linder, N. Shcherbina
MEGAPIE – the impact of radiochemical investigations
MEGAPIE final TRM, Bregenz, Austria, 23-24 October, 2014.

B. Thomas, K. Sonnabend, C. Arda, A. Endres, P. Erbacher, S. Fiebiger, O. Hinrichs, M. Reich, R. Reifarth, S. Schmidt, J. Glorius, U. Giesen, R. Dressler, D. Schumann, H. Kim
Production of ^{91}Nb for a measurement of the $^{91}Nb(p,\gamma)$ reaction at FRANZ
XIII Nuclei in the Cosmos, Debrecen, Hungary, 7-11 July, 2014.

RADIONUCLIDE DEVELOPMENT

K. Domnanich
The potential production of selected Sc radionuclides
Seminar of the Laboratory of Radiochemistry and Environmental Chemistry, Paul Scherrer Institut and University of Berne, Bern, Switzerland, 11 April, 2014.

K. Domnanich , M. Bunka , C. Müller , Prof. R. Schibli , Prof. A. Türler , N.P. van der Meulen
Development of production routes for scandium radionuclides for radiopharmaceutical applications
Center of Radiopharmaceutical Sciences external audit, Paul Scherrrer Institut, Villigen, Switzerland, 24 June, 2014.

G.F. Steyn, C. Vermeulen
Saturation conditions in elongated single-cavity boiling water targets
WTTC15, Prague, Czech Republic, 18-21 August, 2014.

A. Türler
Production of Artificial Radionuclides for Radiopharmaceutical Purposes – Theory
Production of Artificial Radionuclides for Radiopharmaceutical Purposes – Practice
Postgraduate Certificate Course in Radiopharmaceutical Chemistry/Radiopharmacy, ETH Zürich, Zürich, Switzerland, 28 January, 2014.

A. Türler
Radiochemie für das Schweizerische Zentrum für Radionukliddiagnostik, -therapie und Forschung
Workshop zum Konzept „Schweizerisches Zentrum für Radionukliddiagnostik, -therapie und Forschung", Paul Scherrer Institute, Villigen PSI, Switzerland, 20 May, 2014.
A. Türler
New Radionuclides for PET Imaging
Annual Congress of the European Association of Nuclear Medicine, Gothenburg, Sweden, 18-22 October, 2014.

A. Türler
Theragnosis: Diagnostik und Therapie von Krebs mit Radionukliden
BioChemie am Samstag, Departement Chemie und Biochemie, Universität Bern, Bern, Switzerland, 8 November, 2014.

A. Türler
Radionuclides for medical diagnostics and therapy
Colloquium Albert Einstein Centre for Fundamental Physics, University of Bern, Bern, Switzerland, 17 December, 2014.

N. P. van der Meulen
The role of Radionuclide Development at the Center of Radiopharmaceutical Sciences
Center of Radiopharmaceutical Sciences external audit, Paul Scherrrer Institut, Villigen, Switzerland, 24 June, 2014.

N.P. van der Meulen
^{44}Sc production development from ^{44}Ca for radiopharmaceutical application
Terachem 14, Bressanone, Italy, 12 September, 2014.

N.P. van der Meulen
The production of Tb-radionuclides for diagnostic and therapeutic application in nuclear medicine
Topical Day on medical applications of ISOL@MYRRHA, Mol, Belgium, 25 November, 2014.

C. Vermeulen, G.F. Steyn, N.P. van der Meulen
Neutron activation as an independent indicator of expected total yield in the production of ^{82}Sr and ^{68}Ge with 66 MeV protons
WTTC15, Prague, Czech Republic, 18-21August, 2014.

C. Vermeulen
Experiences with bombardments, monitoring and interlocking in high intensity split beam operations using 66 MeV protons delivered by a separated sector cyclotron
8th International Conference on Isotopes, Chicago, USA, 27 August, 2014.

C. Vermeulen
Aspects of the high intensity production of radioisotopes at iThemba LABS
GFA seminar, Paul Scherrer Institut, Villigen, Switzerland, 20 October, 2014.

Environmental Radionuclides Universität Bern

K. Agrios, G. Salazar, Y.L. Zhang, M. Battaglia, S. Szidat
Online coupling of thermal fractionation - ^{14}C AMS for source apportionment of carbonaceous aerosols
13th International Conference on Accelerator Mass Spectrometry, Aix en Provence, France, 24-29 August, 2014.

E. Chavez, C. Solis, E. Ortiz, E. Andrade, S. Szidat, L. Wacker
AMS-^{14}C analysis of graphite from aerosol filters prepared in an automatized graphitization unit (AGE III)
13th International Conference on Accelerator Mass Spectrometry, Aix en Provence, France, 24-29 August, 2014.

K.R. Dällenbach, I. El-Haddad, C. Bozzetti, J.G. Slowik, R.-J. Huang, P. Zotter, F. Canonaco, Y.L. Zhang, V.G. Ciobanu, A. Vlachou, A. Piazzalunga, P. Fermo, U. Baltensperger, S. Szidat, A.S.H. Prévôt
Assessing the factors related with winter haze events in Europe and Asia
European Geosciences Union (EGU) General Assembly 2014, Vienna, Austria, 27 April - 02 May, 2014.

E. Edgerton, Y.L. Zhang, S. Szidat, A. Prévôt, S. Shaw, J. Jansen, K. Baumann, C. Blanchard
Radiocarbon measurements of PM2.5 total carbon and elemental carbon from Centreville, AL during the SOAS field study
33rd Annual Conference of the American Association for Aerosol Research (AAAR), Orlando (FL), USA, 20-24 October, 2014.

P. Hayes, A. Carlton, K. Baker, R. Ahmadov, R. Washenfelder, S. Alvarez, B. Rappenglück, J. Gilman, W. Kuster, J. de Gouw, P. Zotter, A. Prévôt, S. Szidat, T. Kleindienst, J. Offenberg, J. Jimenez
Modeling the formation and aging of secondary organic aerosols in Los Angeles during CalNex 2010
97th Canadian Chemistry Conference, Vancouver, Canada, 1-5 June, 2014.

R.-J. Huang, C. Bozzetti, M. Elser, R. Wolf, Q. Wang, Y. Wang, Y. Chen, K. Dällenbach, K.-F. Ho, J. Cao, Y. Han, F. Canonaco, P. Zotter, J. Slowik, Y.L. Zhang, S. Szidat, U. Baltensperger, I. El Haddad, A.S.H. Prévôt
Chemical characterization and source apportionment of PM2.5 in Chinese megacities
International Aerosol Conference, Busan, Korea, 31 August - 5 September, 2014.

J. Pey, J.C. Cerro, S. Hellebust, H.L. DeWitt, B. Temime-Roussel, M. Elser, N. Pérez, A. Sylvestre, D. Salameh, G. Močnik, A.S.H. Prévôt, Y.L. Zhang, S. Szidat, N. Marchand
Ground-based atmospheric monitoring in Mallorca and Corsica in summer 2013 in the context of ChArMEx: results on number-size distributions, on-line and off-line aerosol chemistry, and volatile organic compounds
2nd Iberian Meeting on Aerosol Science and Technology (RICTA-2014), Tarragona, Spain, 7-9 July, 2014.

J. Pey, J.C. Cerro, S. Hellebust, H.L. DeWitt, B. Temime-Roussel, M. Elser, N. Pérez, A. Sylvestre, D. Salameh, G. Močnik, A.S.H. Prévôt, Y.L. Zhang, S. Szidat, N. Marchand
Atmospheric monitoring in the western Mediterranean in summer 2013: overview of physic-chemical properties and variability
33rd Annual Conference of the American Association for Aerosol Research (AAAR), Orlando (FL), USA, 20-24 October, 2014.

G. Salazar, S. Szidat
Flow dynamics technique for sampling and separation of neutrals from analytes based on their axial momentum density differences
Annual Meeting of the American Society for Mass Spectrometry, Baltimore, USA, 15-19 June, 2014.

G. Salazar, S. Szidat
Flow separation of gas components with different axial momentum for online coupling of CO_2-producing analytical instruments with Accelerator Mass Spectrometry
13th International Conference on Accelerator Mass Spectrometry, Aix en Provence, France, 24-29 August, 2014.

G. Salazar, Y. Zhang, S. Szidat
Coupling of an elemental analyser with AMS for fast radiocarbon analysis of aerosol samples
13th International Conference on Accelerator Mass Spectrometry, Aix en Provence, France, 24-29 August, 2014.

S. Szidat, P. Zotter, Y.L. Zhang, V.G. Ciobanu, L. Wacker, A. Piazzalunga, P. Fermo, U. Baltensperger, A.S.H. Prévôt
Sources of carbonaceous aerosols in Switzerland for winter-smog episodes: Comparison of different apportionment techniques
NOSA (Nordic Society for Aerosol Research) Symposium 2014, Stockholm, Sweden, 30-31 January, 2014.
S. Szidat, G. Salazar
Radiocarbon dating of small samples (<1 mg carbon mass)
International Conference on Culture and Climate, Bern, 11-14 June, 2014.

S. Szidat, P. Zotter, Y.L. Zhang, V.G. Ciobanu, M. Macchia, L. Wacker, U. Baltensperger, A.S.H. Prévôt
Fossil and non-fossil sources of carbonaceous aerosols at urban and rural sites in Switzerland during winter-smog episodes
International Radiocarbon in the Environment Conference, Belfast, United Kingdom, 18-22 August, 2014.

E. Wieland, J. Rothardt, B. Cvetković, S. Szidat, G. Schlotterbeck
Speciation of carbon-14 in the cementitious near field of a repository for radioactive waste: First insights from corrosion experiments with iron powder
Implementing Geological Disposal Technology Platform (IGDTP) Geodisposal Conference 2014, Manchester, United Kingdom, 24-26 June, 2014.

Y.L. Zhang, R.J. Huang, I. El-Haddad, K.F. Ho, J.J. Cao, Y.M. Han, P. Zotter, G. Salazar, M. Schwikowski, J. Schnelle-Kreis, G. Abbaszade, R. Zimmermann, U. Baltensperger, A.S.H. Prévôt, S. Szidat
Fossil vs. non-fossil sources of fine carbonaceous aerosols in four Chinese cities during the extreme winter Haze episode in 2013
AOGS (Asia Oceania Geosciences Society) 11th Annual Meeting, Sapporo, Japan, 28 July - 1 August, 2014.

Y.L. Zhang, G. Salazar, P. Zotter, C. Zellweger, C. Hueglin, A.S.H. Prevot, S. Szidat
Radiocarbon determination of carbonaceous particles (organic carbon and elemental carbon) in rainwater samples
13th International Conference on Accelerator Mass Spectrometry, Aix en Provence, France, 24-29 August, 2014.

Y.L. Zhang, J.W. Liu, G. Salazar, J. Li, G. Zhang, P. Zotter, A.S.H. Prévôt, S. Szidat
Micro-scale (µg) radiocarbon analysis of water-soluble organic carbon in aerosol samples: results from China and Europe
International Aerosol Conference, Busan, Korea, 31 August - 05 September, 2014.

Y.L. Zhang, P. Zotter, D. Smith, R.A Cary, S. Szidat, A.S.H. Prévôt
Dual-wavelength thermal-optical transmittance analysis of organic carbon and elemental carbon: insights into charring
International Aerosol Conference, Busan, Korea, 31 August - 05 September, 2014.

P. Zotter, S. Szidat, Y. Zhang, I. El-Haddad, L. Wacker, A. Piazzalunga, P. Fermo, U. Baltensperger, A.S.H. Prévôt
[14]C-based source apportionment of carbonaceous aerosols in Switzerland for 2008 – 2012
18th ETH Conference on Combustion Generated Nanoparticles, Zurich, Switzerland, 22-25 June, 2014.

PUBLIC RELATIONS AND OUTREACH ACTIVITIES

Radiochemistry

Der Bund
Ein gewisses Gefährdungspotential für die Bevölkerung
3 June 2014

TeleBärn, TV News-Beitrag,
Unia trifft Bauarbeiter in Biel: Sie könnten von Radioaktivität betroffen sein
3 June 2014

Blick am Abend
Neuen Elementen auf der Spur
29 October 2014

Analytical Chemistry

PSI Medienmitteilung
Wenn auftauende Gletscher Schadstoffe wieder freisetzen
31 October 2014

Agence Télégraphique Suisse
En fondant, les glaciers relâchent les polluants qu'ils stockaient
31 October 2014

RTS.ch
En fondant, les glaciers menacent de relâcher les polluants qu'ils stockaient
31 October 2014

LE MATIN.ch
Les glaciers risquent de relâcher des polluants
31 October 2014

24 Heures
Les glaciers risquent de relâcher des polluants
31 October 2014

Tribune de Genève
Les glaciers risquent de relâcher des polluants
31 October 2014

SDA-Schweizerische Depeschenagentur
Forscher messen erstmals Schadstoffe im Eis eines Alpengletschers
31 October 2014

Tagesanzeiger, Der Bund, Basler Zeitung, Berner Zeitung
Die Altlast im Gletschereis
1 November 2014

Le Temps
Des polluants relâchés par les glaciers
1 November 2014

Die Botschaft
Wenn auftauende Gletscher Schadstoffe wieder freisetzen
3 November 2014

http://phys.org/news/2014-11-glaciers-pollutants.html
When thawing glaciers release pollutants
3 November 2014

24 Heures
En fondant, las glaciers relâchent des polluants
14 November 2014

Tribune de Genève
En fondant, las glaciers relâchent des polluants d'origine industrielle
14 November 2014

Öffentliche Führung Paul Scherrer Institut
Eisbohrkerne - dem Klimawandel auf der Spur
1 December 2014

Umwelttechnik Schweiz
Wenn auftauende Gletscher Schadstoffe wieder freisetzen
30 December 2014

Hydrologie und Wasserbewirtschaftung
Schadstoffe im Eis eines Alpengletschers
December 2014

Radwaste Analytics

The University of Edinburgh
Radioactive waste used to explore exploding stars
3 April 2014

New Scientist
Radioactive waste used to peek inside a star explosion
3 April 2014

CERN
ISOLDE sheds light on dying stars
4 April 2014

Phys.org™ Science X network
ISOLDE sheds light on dying stars
4 April 2014

Paul Scherrer Institute
Astral matter from the Paul Scherrer Institute
8 April 2014

Surface Chemistry

IUPAC Task Group on Atmospheric Chemical Data Evaluation (M. Ammann et al.), SPARC newsletter no 42, January 2014, pages 22-22.

Science Feature, IUPAC Task Group on Atmospheric Chemical Data Evaluation (M. Ammann et al.), IGACnews, issue 51, February 2014, pages 11-13.

Nachrichten aus der Chemie
Im Schnee und durch den Schnee
26 March 2014

Environmental Radionuclides Universität Bern

TV SRF 1, Schweiz Aktuell
Berner Zytglogge: Hans von Thann muss wieder zur Arbeit (TV report)
http://www.srf.ch/player/tv/videoembed?id=92a2a3b0-1472-406d-9a0b-919fcf008187
http://www.srf.ch/news/regional/bern-freiburg-wallis/der-alte-gloeckner-von-bern
15 April 2014

Radio SRF 1, Regionaljournal Bern Fribourg Wallis
Berner Zytglogge: Hans von Thann muss wieder zur Arbeit (Radio interview)
http://www.srf.ch/news/regional/bern-freiburg-wallis/berner-zytglogge-hans-von-thann-muss-wieder-zur-arbeit
15 April 2014

Berner Zeitung BZ
Hans von Thann muss wieder zur Arbeit
http://www.bernerzeitung.ch/region/bern/Hans-von-Thann-muss-wieder-zur-Arbeit/story/28183174
16/17 April 2014

Jahresbericht 2013 der Universität Bern
Ein Analysegerät für alle - die neue Radiokarbon-Messanlage
https://media.unibe.ch/public/Jahresberichte/2013/index.html
May 2014

Brunne Zytig 2/2014
Seltene Einblicke ins vielschichtige Innere des Stundenschlägers
http://altstadtleiste.ch/wp-content/uploads/2014/05/BrunneZytig_2014_2.pdf
20 June 2014

Blick
Forscher klären Quellen des chinesischen Rekord-Smogs
http://www.blick.ch/life/wissen/umwelt-forscher-klaeren-quellen-des-chinesischen-rekord-smogs-id3135723.html
17 September 2014

Tages Anzeiger
Russ allein macht noch keinen Smog
http://www.tagesanzeiger.ch/wissen/natur/Russ-allein-macht-noch-keinen-Smog/story/12535241
18 September 2014

CCTV News
Haze causes in China: Secondary aerosol is the main cause of haze (translation from Chinese)
http://news.cntv.cn/2014/09/18/VIDE1411004711222840.shtml
18 September 2014

Chemical Laboratory Technician Apprenticeship

Muba (Messe Basel)
14-19 February 2014

Lehrberufe a la carte (Berufsschau am PSI)
29 June 2014

Sommercamp (Experimente für Primarschüler)
7-11 July 2014

Lela Calancatal
15-22 Oktober 2014

Zukunftstag am PSI
13 November 2014

LECTURES AND COURSES

Prof. Dr. A. Türler
Universität Bern, FS2014
Bachelor
- Instrumentalanalytik II (with Dr. K. Krämer and Prof. M. Schwikowski) (3 ECTS)
- Allgemeine Chemie (Einführung Radioaktivität) (with Prof. R. Hähner and Prof. J. Hulliger) (4 ECTS)

Universität Bern, HS2014
Bachelor
- Physikalische Chemie IV (with PD P. Broekmann) (3,75 ECTS)
- Praktikum Phys. Chemie II (with others) (4 ECTS)
- Biochemische Methoden I (with others) (3 ECTS)

Master
- Nuclear and Radiochemistry (with Dr. R. Eichler) (3 ECTS)
- Lab course: Nuclear and Radiochemistry at Bern, Basel, ETHZ and PSI (with others) (4 ECTS)
- Seminar Radio- und Umweltchemie in collaboration with Paul Scherrer Institut
  (organized by Dr. N. van der Meulen FS2014 / HS2014)

Prof. Dr. M. Schwikowski
Universität Bern, FS2014
Bachelor
- Instrumentalanalytik II (with Prof. A. Türler and Dr. K. Krämer) (3 ECTS)

Master
- Summer Course at Paul Scherrer Institut. 2months International Summer Student Programme
  (with Prof. A. Türler) (4 ECTS)

Prof. Dr. M. Ammann
ETH Zürich, FS2014
Bachelor
- Systempraktikum Atmosphäre und Klima (7 ECTS)

Master
- Atmospheric Interface Chemistry (3ECTS)

ETH Zürich, HS2014
Bachelor
- Atmosphärenchemie (with Dr. D. Brunner) (3 ECTS)

Dr. T. Bartels-Rausch
Universität Bern, HS2014
Master
- Lab course: Nuclear and Radiochemistry at the PSI (with Prof. A. Türler and PD Dr. S. Szidat) (4 ECTS)

Dr. R. Eichler
Universität Bern, HS2014
Master
- Nuclear and Radiochemistry (with Prof. A. Türler) (3 ECTS)

Universität Bern, HS2014
Bachelor
- Praktikum Phys. Chemie II (with Prof. A. Türler) (4 ECTS)
Master
- Lab course: Nuclear and Radiochemistry (with Prof. A. Türler and PD Dr. S. Szidat) (4 ECTS)

PD Dr. S. Szidat
Universität Bern, FS2014
Bachelor
- Ergänzungen zur analytischen Chemie für Pharmaziestudierende (2 ECTS)

Universität Bern, HS2014
Bachelor
- Chemie für Studierende der Veterinärmedizin (with C. Leumann) (4.5 ECTS)
- Praktikum Physikalische Chemie II (with others) (4 ECTS)

Master
- Lab Course Nuclear and Radiochemistry (with A. Türler and R. Eichler) (4 ECTS)

N. Chiera
- Practice Course "Physical Chemistry I", DCB University of Bern 2014

G. Grzinic
- Lab Course Nuclear and Radiochemistry, PSI & DCB University of Bern 2014

Dr. S. Heinitz
- Practice Course "Physical Chemistry II" Liquid Scintillation Counting", DCB University of Bern 2014

M.-T. Lee
- Practice Course "Physical Chemistry I", DCB University of Bern 2014

J. Schindler
- Practice Course "Physical Chemistry I", DCB University of Bern 2014

P. Steinegger
- Practice Course Physical Chemistry II "γ-Spectroscopy", DCB University of Bern 2014

I. Usoltsev
- Practice Course "Physical Chemistry I", DCB University of Bern 2014

A. Waldner
- Tutor in "Atmosphärenchemie" D-USYS, ETH Zürich 2014

EDUCATION OF APPRENTICIES AS CHEMISTRY LABORATORY TECHNICIANS

R. Bentz

The vocational training is very important at the Paul Scherrer Institute. 95 apprentices and 3 trainees are employed here. This corresponds to a proportion of about 5 percent of all employees (~ 2000). Already this percentage perfectly demonstrates the status belonging to the vocational training at our research centre.

Among the vocational trainings available at PSI also the apprenticeship as chemical laboratory technician is offered. Three apprentices are employed by PSI per year in this professional direction. Since the training lasts for three years, nine chemical laboratory technician trainees are permanently at PSI. The education and training follows a rotational principle. Thus the trainees are working at 10 different research laboratories within PSI:

Atmospheric chemistry
Stable isotope analysis in conjunction with elemental analysis (EAII & Pyro-Cube, HPLC-IRMS, GC-IMRS);

Diffusion processes
Ion chromatography (anions, cations); Carbon analysis (TOC, TIC); Radiochemical analysis (Beta and gamma measurements);

Molecular biology
Various tasks connected to gene expression; gene manipulation at plasmids; DNA preparation and DNA analyses;

Protein biochemistry
Purification of proteins applying various chromatographic methods (FPLC); Biophysical characterization of purified proteins; Help with cultivation of animal and human cells in appropriate nutrient medium;

Radiation protection / Radioanalytics
Various measurement methods including gamma spectrometry and Alpha spectrometry using Ge- and Si- surface barrier detectors; Alpha/beta liquid scintillation counting and proportional counting;

Bioenergy and catalysis
Exhaust analysis using FTIR, ion selective electrodes; Production of catalyst modules with V_2O_5 or Pt/Pd as active components

Laboratory for Micro- and Nanotechnology
Binding of proteins to surfaces; Characterization of surfaces by contact angle measurements, light microscopy and scanning force microscopy;

Laboratory for Radiopharmacy
Radionuclide labeling of bio molecules including quality control using HPLC; In vitro and ex vivo autoradiography including cryo-thin sectioning;

Synthesis Laboratory
Synthesis of organic and inorganic chemicals; Analysis of chemicals with UPLC, GC, GC-MS, NMR;

Synthesis Laboratory
Sulfonation reactions with chlorosulfonic acid HSO_3Cl; *ex-situ* analysis (e.g.: titrations, FT-IR, SEM-EDX [with supervision], permeation measurements, conduction measurements as function of relative humidity, temperature etc..

http://www.psi.ch/bab/
http://www.psi.ch/bab/laborantin-efz-fachrichtung-chemie

MEMBERS OF SCIENTIFIC COMMITTEES
EXTERNAL ACTIVITIES

Prof. Dr. Markus Ammann
- Atmospheric Chemistry and Physics, member of editorial board
- IUPAC Task Group on Atmospheric Chemical Kinetic Data Evaluation, member
- PSI internal research commission (FoKo), member

Dr. Thorsten Bartels-Rausch
- Air-Ice Chemical Interactions (OASIS-AICI), Co-Chair
- Physics and Chemistry of Ice (PCI), member of the scientific committee
- General Assembly of the International Union of Geodesy and Geophysics, Session: Air-Ice Chemical Interactions, Co-Convener
- Fourth workshop of the Air Ice Chemical Interactions (AICI) task, Cambridge, UK; 2014, scientific committee
- European Geosciences Union General Assembly, Session: Boundary Layers in High Latitudes and Over Snow and Ice: Physics and Chemistry. Co-Convener
- Schweizerische Gesellschaft für Schnee, Eis und Permafrost (SEP), Financial Controller
- Atmospheric Chemistry and Physics, member of editorial board

Dr. Robert Eichler
- PSI internal research commission (FoKo), member
- Associate Editor of the International Journal of Modern Physics E (IJMPE)World Scientific Publishing

Dr. Jörg Neuhausen
- Member of the Expert group on Heavy Liquid Metal Technologies of the OECD/NEA Working Party on Scientific Issues of the Fuel Cycle (WPFC)

Dr. Dorothea Schumann
- PSI internal Neutron Source Development Group, member
- SEARCH, governing board member
- LIEBE, steering committee member

Prof. Dr. Margit Schwikowski
- Schweizerische Gesellschaft für Schnee, Eis und Permafrost (SEP), president
- Council of the International Glaciological Society, elective member
- Oeschger Centre for Climate Change Research (OCCR), member
- ERC starting and consolidator grant, remote reviewer
- International Partnerships in Ice Core Sciences (IPICS), Steering Committee member
- Member of PhD thesis committee of Helle Astrid Kjær, Continuous chemistry in ice cores, -Phosphorus, pH and the photolysis of humic like substances, University of Copenhagen, 25 August 2014.

PD Dr. Sönke Szidat
- Bernese Chemical Society (Berner Chemische Gesellschaft, BCG), president
- Oeschger Centre for Climate Change Research (OCCR), member
- Swiss Accreditation Service (SAS), technical expert

Prof. Dr. Andreas Türler
- Eidgenössische Kommission für Strahlenschutz und Überwachung der Radioaktivität (KSR), Vizepräsident
- Gesellschaft Deutscher Chemiker (GDCh), Fachgruppe Nuklearchemie, Vorstands-Beirat
- Radiochimica Acta, member of the advisory board
- Oeschger Centre for Climate Change Research (OCCR), Mitglied des Wissenschaftlichen Ausschusses
- Nuklearforum Schweiz, Mitglied des Vorstandes
- Member of the Albert Einstein Center for Fundamental Physics (AEC) Bern

Dr. Nicholas van der Meulen
- DOE Isotope R&D FOA, Panel Reviewer

BACHELOR THESIS

Prisca Lehmann

Optimized ^{14}C dating of fossil snails

PD Dr. S. Szidat / Uni Bern
May 2014

Marc Luginbühl

Online source apportionment of carbonaceous aerosols with radiocarbon

PD Dr. S. Szidat / Uni Bern
May 2014

MASTER THESIS

Dejan Husrefovic

Determination of fossil CO_2 in air with ^{14}C analysis

PD Dr. S. Szidat / Uni Bern
February 2014

Jacqueline Fenwick

Determination of accumulation rates from a shallow firn core of the West Antarctic Ice Sheet

Prof. Dr. M. Schwikowski / PSI & Uni Bern
December 2014

DOCTORAL THESIS

Maruta Bunka

The radionuclides ^{44}Ti and ^{44}Sc: Their production, isolation, and application in astrophysics and radio pharmacy

PD Dr. Christina Müller / PSI
Prof. Dr. A. Türler / PSI & Uni Bern
February 2014

Stefan Söllradl

Developments in prompt gamma-ray neutron activation analysis and cold neutron tomography and their application in non-destructive testing

Dr. Zsolt Revay / TU München
Prof. Dr. A. Türler / PSI & Uni Bern
March 2014

Isabel Wendl

High resolution records of black carbon and other aerosol constituents from the Lomonosovfonna 2009 ice core

Prof. Dr. M. Schwikowski / PSI & Uni Bern
September 2014

Pavlina Pavlova

Accelerated release of persistent organic pollutants from alpine glaciers

Prof. Dr. M. Schwikowski / PSI & Uni Bern
September 2014

Sarah Steimer

Interplay of diffusivity and reactivity in organic aerosol aging

Prof. Dr. M. Ammann / PSI & ETHZ
Prof. Dr. T. Peter/ ETHZ
November 2014

Ilya Usoltsev

Methodical developments for future chemical investigations of superheavy elements

Dr. Robert Eichler / PSI
Prof. Dr. A. Türler / PSI & Uni Bern
December 2014

Goran Grzinic

The multiphase chemical kinetics of dinitrogen pentoxide with aerosol particles

Prof. Dr. Markus Ammann / PSI & ETHZ
Prof. Dr. A. Türler / PSI & Uni Bern
December 2014

ADJUNCT PROFESSOR

Markus Ammann

was awarded adjunct professor of ETHZ

For his achievements in research and teaching in the field of atmospheric chemistry, June 2014

AWARDS

Nadine Chiera

Towards the selenides of the superheavy elements copernicium and flerovium
Best presentation Award

First Year Graduate Student Symposium of the Department of Chemistry and Biochemistry 2014, University of Bern
September 2014

Desirée Burkhart

Best degree of the apprentices as chemistry laboratory technician in the canton Aargau
June 2014

SUMMER STUDENTS

Philipp Meier
Gymnasium Bäumlihof, Basel
Maturarbeit
Einfluss von kosmischer Strahlung auf das globale Klima und die Klimarekonstruktion mit Gletschereis

Loic Schmidely
Analysis of black carbon in snow and ice samples with the Single Particle Soot Photometer (SP2)
1 July - 14 September 2014

Simon Rohrbach
Preparation of intermetallic lanthanide and actinide targets with rhodium metal backing
1 July - 29 August 2014

David Roesel
Investigation of the uptake of H_2O_2 to ice by means of a coated wall flow tube
11-29 August 2014

VISITING GUESTS AT PSI 2014

1-31 January
Kim Rijpstra, University of Ghent, Belgium
Computationally capturing polonium on noble metals

3-5 February
Marin Ayranov, European Commission, DG-Energy, Luxembourg
Participation in ^7Be separation

3-6 March
Fadil Inceoglu, The Department of Physics and Astronomy, Aarhus University, Denmark
Sampling of Tsambagarav ice core for ^{10}Be analysis

12-14 March
Roy Pöllänen, Radation and Nuclear Safety Authority, Helsinki, Finland
Sample characterization using alpha spectrometry

11 April
Gesine Mollenhauer, Alfred-Wegener-Institut, Bremerhaven, Germany
How compound-specific radiocarbon analysis elucidates carbon cycling in high latitudes

9 May
Stefaan Cottenier, Ghent University, Belgium
Polonium in Accelerator Driven Systems: computer experiments met lab experiments

28 May
Fabrice Lambert, Center for Climate and Resilience Research, University of Chile, Santiago, Chile
The potential of Central Andean glaciers to preserve a record of air pollution from the city of Santiago

1-11 June / 29 June- 5 July
Carmen Vega, Uppsala University, Sweden
Tonu Martma, Tallinn University of Technology, Estonia
Sampling of ice cores from Fimbulisen ice shelf, western Dronning Maud Land, Antarctica, for ion chromatography and stable isotope analyses

10 August - 31 December (several times)
Thomas Berkemeier, Max-Planck- Institut für Chemie, Mainz, Germany
N-13 experiments at PROTRAC Facility related to formation of nitrates in secondary organic aerosol

18-20 August
Tong Haijie, Max-Planck- Institut für Chemie, Mainz, Germany
Visiting guest in the context of aerosol flow tube experiments

1 September - 10 October
Dariusz Aksamit, Warsaw University of Technology, Warsaw, Poland
Performed dosimetric calculations on the cellular level using Medical Internal Radiation Dose (MIRD) formalism

1-6 September
Andrius Garbaras, SRI Center for Physical Sciences and Technology, Vilnius, Lithuania
Radiocarbon analysis of carbonaceous aerosols

23 September
Crispin Halsall, University of Lancaster, United Kingdom
Persistent organic pollutants in snow and ice

9 October
Mathias Vuille, Department of Atmospheric and Environmental Sciences, University at Albany, USA
Reconstruction of South American monsoon variability based on stable isotopic proxies and model simulations

15-18 October

Elisabeth Issakson, Norwegian Polar Institute, Tromso, Norway
Ice core records from Lomonosovfonna, Svalbard and Fimbulsen Ice Shelf, Antartica

18 October

Robert Mulvaney, British Antarctic Survey, Cambridge, United Kingdom
Ice core records from Lomonosovfonna, Svalbard

11 November 2014

Boon Lee, Australian National University, Australia
Auger electron yields for nuclear physics and medical applications

2-9 December

Jan-David Förster, Max-Planck- Institut für Chemie, Mainz, Germany
Participation in STXM beamtime at POLLUX/SLS and discussion of new environmental cell design
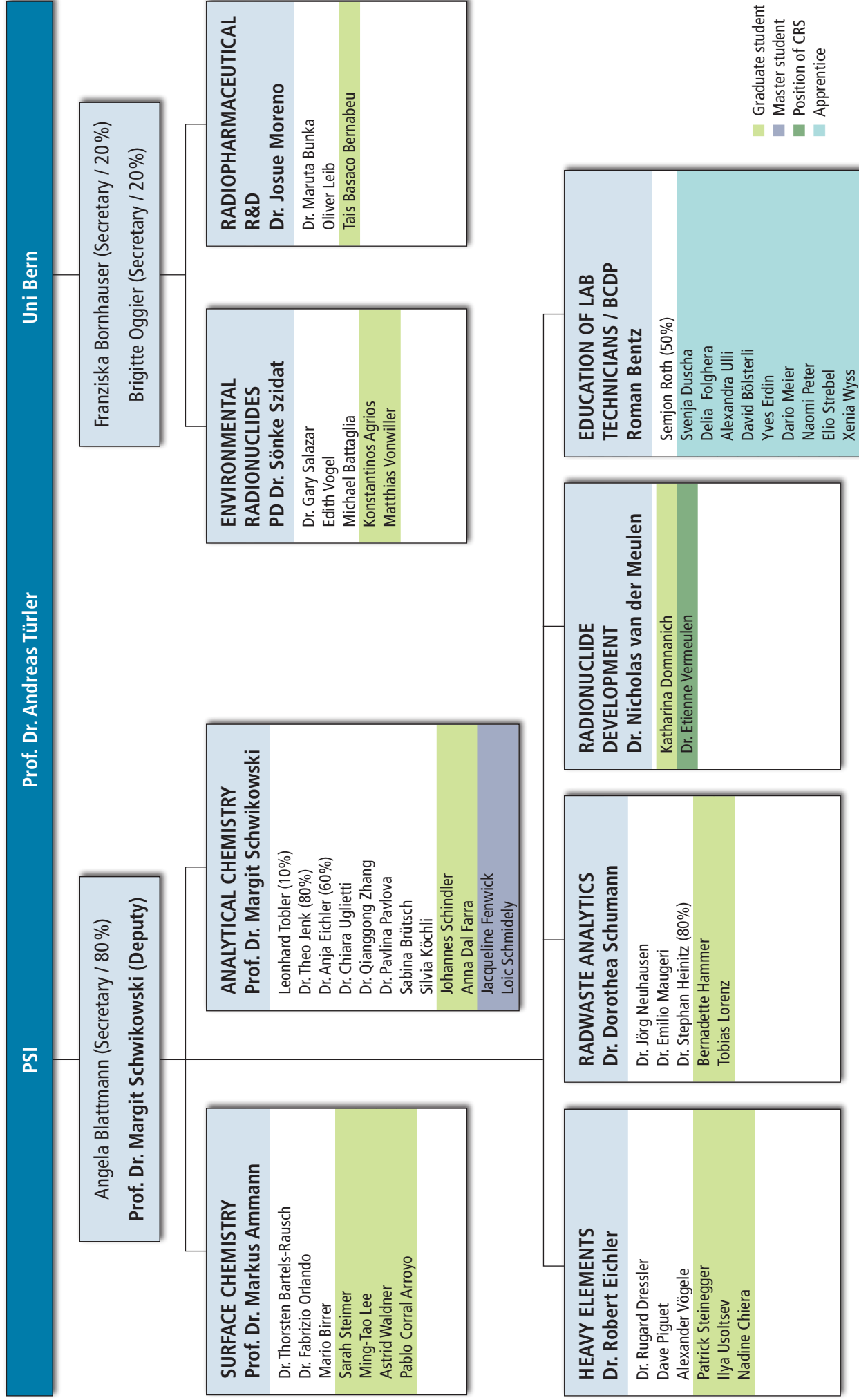
2-9 December

Peter Alpert. IRCELYON, CNRS; University of Lyon, France
Participation in STXM beamtime at POLLUX/SLS in the context of ocean surface microlayer samples

12 December

Davide Vione, University of Torina, Italy
Photochemical formation of substances with humic-like fluorescence in aqueous solution

LABOR FÜR RADIO- UND UMWELTCHEMIE
DES PAUL SCHERRER INSTITUTS UND DER UNIVERSITÄT BERN
31.12.2014

PAUL SCHERRER INSTITUT

u^b
UNIVERSITÄT BERN

Prof. Dr. Andreas Türler

PSI

Uni Bern

Angela Blattmann (Secretary / 80%)
Prof. Dr. Margit Schwikowski (Deputy)

Franziska Bornhauser (Secretary / 20%)
Brigitte Oggier (Secretary / 20%)

SURFACE CHEMISTRY
Prof. Dr. Markus Ammann

Dr. Thorsten Bartels-Rausch
Dr. Fabrizio Orlando
Mario Birrer
Sarah Steimer
Ming-Tao Lee
Astrid Waldner
Pablo Corral Arroyo

ANALYTICAL CHEMISTRY
Prof. Dr. Margit Schwikowski

Leonhard Tobler (10%)
Dr. Theo Jenk (80%)
Dr. Anja Eichler (60%)
Dr. Chiara Uglietti
Dr. Qianggong Zhang
Dr. Pavlina Pavlova
Sabina Brütsch
Silvia Köchli
Johannes Schindler
Anna Dal Farra
Jacqueline Fenwick
Loïc Schmidely

ENVIRONMENTAL RADIONUCLIDES
PD Dr. Sönke Szidat

Dr. Gary Salazar
Edith Vogel
Michael Battaglia
Konstantinos Agrios
Matthias Vonwiller

RADIOPHARMACEUTICAL R&D
Dr. Josue Moreno

Dr. Maruta Bunka
Oliver Leib
Tais Basaco Bernabeu

HEAVY ELEMENTS
Dr. Robert Eichler

Dr. Rugard Dressler
Dave Piguet
Alexander Vögele
Patrick Steinegger
Ilya Usoltsev
Nadine Chiera

RADWASTE ANALYTICS
Dr. Dorothea Schumann

Dr. Jörg Neuhausen
Dr. Emilio Maugeri
Dr. Stephan Heinitz (80%)
Bernadette Hammer
Tobias Lorenz

RADIONUCLIDE DEVELOPMENT
Dr. Nicholas van der Meulen

Katharina Domnanich
Dr. Etienne Vermeulen

EDUCATION OF LAB TECHNICIANS / BCDP
Roman Bentz

Semjon Roth (50%)
Svenja Duscha
Delia Folghera
Alexandra Ulli
David Bölsterli
Yves Erdin
Dario Meier
Naomi Peter
Elio Strebel
Xenia Wyss

Legend:
Graduate student
Master student
Position of CRS
Apprentice

AUTHOR INDEX

AFFILIATION INDEX

ABE	Abteilung Beschleuniger / Betrieb und Entwicklung (ABE), Paul Scherrer Institut, 5232 Villigen, Switzerland
AHL	Hot Laboratory Division of the Nuclear Energy and Safety Department (NES), Paul Scherrer Institut, 5232 Villigen, Switzerland
ASI	Abteilung Strahlenschutz und Sicherheit, Paul Scherrer Institut, 5232 Villigen, Switzerland
ASRC, JAEA	Advanced Science research Center, Japan Atomic Energy Agency, Tokai, Ibaraki 319-1195, Japan
ASQ	Spallation Neutron Source Division (NUM), Paul Scherrer Institut, 5232 Villigen, Switzerland
BAS	British Antarctic Survey, Cambridge Cambridgeshire CB3 0ET, United Kingdom
CAS-GIG	State Key Laboratory of Organic Geochemistry, Guangzhou, Institute of Geochemistry, Chinese, Academy of Sciences, Guangzhou, China
CAS-IEE	State Key Laboratory of Loess and Quaternary Geology (SKLLQG), Institute of Earth Environment, Chinese Academy of Sciences, Xi'an, China
CEA	CEA/Saclay: Commissariat à l'énergie atomique et aux énergies alternatives/Saclay, 91191 Gif-sur-Yvette, Cedex, France
CECS	Centro de Estudios Científicos, Valdivia, Chile
CERN	European Organization for Nuclear Research, CERN CH-1211, Genève 23, Switzerland
CRS	Center for Radiopharmaceutical Sciences, Paul Scherrer Institut, 5232 Villigen, Switzerland
CU	University of Colorado, Boulder, CO 80309, USA
Empa	Swiss Federal Laboratories for Materials Science and Technology, Überlandstrasse 129, 8600 Dübendorf, Switzerland
ENSI	Eidgenössisches Nuklearsicherheitsinspektorat, Industriestrasse 19, 5200 Brugg, Switzerland
ESS AB	ESS AB: European Spallation Source ESS AB, P.O. Box 176, SE-221 00 Lund, Sweden
ETHZ	Eidgen. Technische Hochschule Zürich, 8092 Zürich, Switzerland
EU	European Union
FLNR Dubna	Flerov Laboratory of Nuclear Reactions, Joliot Curie 6, 141980 Dubna, Russia
Geoestudios	Los Aromos 3408, Las Vertientes, San Jose de Maipo Santiago, Chile
GIG CAS	Guangzhou Institute of Geochemistry, Chinese Academy of Sciences, Guangzhou, China
GNS	Institute of Geological and Nuclear Sciences, National Isotope Centre, Lower Hutt 5040, New Zealand
GSI	Helmholtzzentrum für Schwerionenforschung GmbH, 64291 Darmstadt, Germany
HIM	Helmholtz-Institut Mainz, 55099 Mainz, Germany
HNINP	Henryk Niewodniczański Institute of Nuclear Physics, Radzikowskiego 152, 31-342 Kraków, Poland
HZ München	Helmholtz Zentrum München, German Research Center for Environmental (GmbH), Neuherberg, Germany
ILL	Institut Laue-Langevin, 71 avenue des Martyrs 38000 Grenoble, France
JAEA	Japan Atomic Energy Agency, Tokai-mura, Naka-gun Ibaraki-ken, 319-1195, Japan
KTH	Kungl Tekniska Högskolan, SE-100 44 STOCKHOLM, Sweden

KUP	Climate and Environmental Physics, Physics Institute, University of Bern, Sidlerstrasse 5, 3012 Bern, Switzerland
LAC	Laboratory of Atmospheric Chemistry, Paul Scherrer Institut, 5232 Villigen, Switzerland
LBK	Bioenergy and Catalysis Laboratory, Paul Scherrer Institut, 5232 Villigen, Switzerland
LNM	Laboratory for Nuclear Materials, Bereich Nuclear Energy and Safety (NES), Paul Scherrer Institut, 5232 Villigen, Switzerland
LSK PSI	Laboratory for Synchrotron Radiation – Catalysis and Sustainable Chemistry, Paul Scherrer Institut, 5232 Villigen, Switzerland
MPIC	Max-Planck-Institut für Chemie (Otto-Hahn-Institut), Joh.-Joachim-Becher-Weg 27, 55128 Mainz, Germany
NPI	Norwegian Polar Institute, N-9296 Tromsø, Norway
PSI	Paul Scherrer Institut, 5232 Villigen, Switzerland
SCK CEN	SCK-CEN: Belgian Nuclear Research Centre, Boeretang 200, B-2400 Mol, Belgium
SLS	Swiss Light Source, Paul Scherrer Institut, 5232 Villigen+, Switzerland
SNF	Schweizerischer Nationalfonds SNF, Wildhainweg 3, 3001 Bern, Switzerland
SUBATECH	SUBATECH Laboratory, CNRS/IN2P3-EMN-Universite, 44307 Nantes, France
Tallin Univ. Technology	Tallinn University of Technology, Institute of Geology, Tallinn, Estonia
Univ. Albany	University at Albany, Department of Atmospheric and Environmental Sciences, Albany, NY, 12222, USA
Univ. Bern	Departement für Chemie und Biochemie, Universität Bern, Freiestr. 3, 3012 Bern, Switzerland
Univ. Fribourg	University of Fribourg, Avenue de l'Europe 20, 1700 Fribourg, Switzerland
Univ. Innsbruck	University of Innsbruck, Institute of Meteorology and Geophysics, A-6020 Innsbruck, Austria
Univ. Magallanes	University of Magallanes, Punta Arenas 6210427, Chile
Univ. Mainz	Johannes Gutenberg-Universität Mainz, Saarstr. 21, 55122 Mainz, Germany
Univ. Massachusetts	University of Massachusetts Amherst, MA 01003, USA
Univ. Nanjing	Nanjing University, 22 Hankou Road, Gulou, Nanjing, Jiangsu, China
Univ. Zürich	University of Zurich, Department of Geography, 8057 Zurich, Switzerland
Uppsala Univ.	Uppsala University, 751 05 Uppsala, Sweden
Vicencio Expeditions	Pasaje las Azucenas, Huaraz-Ancash, Peru
WSL	Swiss Federal Research Institute WSL, 8903 Birmensdorf, Switzerland
Yale-NUIST	Center on Atmospheric Environment, Nanjing University of Information Science and Technology, Nanjing, Jiangsu, China